Deciphering earthquake triggering mechanisms for induced seismicity using a fully coupled poroelastic model and machine learning analysis

Ryley Graham Hill[1], Daniel T. Trugman[2], and Matthew Weingarten[3]

[1]University of California, San Diego
[2]University of Nevada, Reno
[3]San Diego State University

April 23, 2024

Abstract

In areas of induced seismicity, earthquakes can be triggered by stress changes from fluid injection and from static deformation caused by fault slip. Here we present a method to distinguish between injection-driven and earthquake-driven triggering of induced seismicity by combining a calibrated, fully-coupled, poroelastic stress model of wastewater injection with a random forest machine learning algorithm trained on both earthquake catalog and modeled stress features. We investigate the classic Paradox Valley, Colorado induced seismicity dataset as an ideal test case: a single, high-pressure injector that has induced >7000 earthquakes between 1991 and 2012. We find that injection-driven earthquakes are approximately 22±-5% of the total catalog and have distinct spatiotemporal clustering with a larger b-value, closer proximity to the well and earlier occurrence in the injection history. Our model may be applicable to other regions to help determine site's susceptibility to triggered earthquakes due to fluid injection.

Deciphering earthquake triggering mechanisms for induced seismicity using a fully coupled poroelastic model and machine learning analysis

R. G. Hill[1,2], D. Trugman[3], and M. Weingarten[1]

[1]Department of Geological Sciences, San Diego State University, San Diego, California
[2]Scripps Institution of Oceanography, University of California San Diego, La Jolla, California
[3]Nevada Seismological Laboratory, University of Nevada, Reno, Nevada

Key Points:

- Combining physics-based and machine learning models can decipher earthquake triggering mechanisms for induced seismicity.
- Injection-driven earthquakes account for just 22±5% of all earthquakes in the Paradox Valley catalog.
- Injection-driven earthquakes have a larger b-value, are closer to the well, and occur earlier in the injection history.

Corresponding author: Ryley G. Hill, `ryleyghill@gmail.com`

Abstract

In areas of induced seismicity, earthquakes can be triggered by stress changes from fluid injection and from static deformation caused by fault slip. Here we present a method to distinguish between injection-driven and earthquake-driven triggering of induced seismicity by combining a calibrated, fully-coupled, poroelastic stress model of wastewater injection with a random forest machine learning algorithm trained on both earthquake catalog and modeled stress features. We investigate the classic Paradox Valley, Colorado induced seismicity dataset as an ideal test case: a single, high-pressure injector that has induced >7000 earthquakes between 1991 and 2012. We find that injection-driven earthquakes are approximately 22±5% of the total catalog and have distinct spatiotemporal clustering with a larger b-value, closer proximity to the well and earlier occurrence in the injection history. Our model may be applicable to other regions to help determine site's susceptibility to triggered earthquakes due to fluid injection.

Plain Language Summary

The Paradox Valley Unit, Colorado in the central United States has had a remarkable increase in seismicity coincident with over 8 million cubic meters of brine fluid injection since 1991, inducing >7000 earthquakes within an aquifer 4.5 km below the surface. We use a physics-based model of the Earth combined with statistical and machine learning techniques to help discern which earthquakes are triggered by other earthquakes and which earthquakes are directly triggered by the stress changes from the well as well as their comparative characteristics. Discerning which earthquakes are directly caused from pressure changes due to the fluid injected by the well can inform our understanding of earthquake physics and provide useful information to operators of energy production sites.

1 Introduction

A variety of anthropogenic industrial activities, including wastewater disposal, can induce seismicity (Ellsworth, 2013; Keranen et al., 2014; Shirzaei et al., 2016). Similar to naturally occurring earthquakes, induced seismicity typically occurs on pre-existing, critically stressed faults (Townend & Zoback, 2000). Generating induced seismicity from the reactivation of faults is attributed to several physical mechanisms: pore pressure diffusion (Keranen & Weingarten, 2018; Weingarten et al., 2015; Langenbruch et al., 2018), poroelastic coupling (Segall & Lu, 2015), and stress changes caused by seismic or aseismic fault slip (Ge & Saar, 2022; Brown & Ge, 2018).

These physical mechanisms for induced seismicity jointly contribute to the triggering potential of each earthquake. Since induced earthquakes can be triggered by small stress changes of order 1-10 kPa (Bachmann et al., 2012; Cacace et al., 2021; Stokes et al., 2023), a large difficulty arises in deciphering which mechanism was responsible for triggering each earthquake. We are particularly interested in discerning which earthquakes were more likely driven by injection-related stress changes and which earthquakes were more likely driven by stress changes from prior earthquakes. Furthermore, site-to-site differences in physical rock properties, reservoir structure, fault geometry, and remnant tectonic stress could contribute to differences in the ratio of injection-driven and earthquake-driven events despite similar injection-related stresses.

Relative stress changes from fluid injection require analytical or numerical models to resolve the spatio-temporal evolution of pore pressure and poroelastic stress. To capture the fully coupled poroelastic stress changes (Biot, 1941; Rice & Cleary, 1976; Wang, 2000) induced from the fluid sources requires detailed knowledge of the hydrogeologic properties of the region. The fault geometry is also critical for resolving fault plane stress tractions that characterize fault stability and the potential for induced seismicity (G. C. P. King et al., 1994; Cocco, 2002; Levandowski et al., 2018). Hence, any attempt at discerning induced earthquakes requires an accurate and comprehensive hydrogeological model, detailed injection well data, precise fault geometries, and high-resolution earthquake catalog.

Here, we investigate which earthquakes are more likely triggered by stress changes from injection and which earthquakes are more likely triggered by earthquake-earthquake interaction. We built a three-dimensional (3D) fully-coupled poroelastic model of Paradox Valley Unit, CO (PVU) to resolve time-dependent pore pressure and stress changes due to brine injection. To inform the contribution of our earthquake triggering mechanisms, we use a random forest regression machine learning analysis trained on more than 20 years of induced earthquakes at Paradox Valley Unit and SHapley Additive exPlanations (SHAP), a game theoretic approach to explain the output of any machine learning model (Lundberg & Lee, 2017). We corroborate our results with an independent, induced seismicity cluster analysis, which demonstrates that the physics-based machine learning method provides novel insight into discerning triggering mechanism not previously captured. This model explores the induced earthquake triggering process for wastewater disposal and could help discern what regions are more or less susceptible to stress changes from anthropogenic sources with applicability to other types of subsurface injection including CO_2 sequestration, enhanced geothermal systems, and hydraulic fracturing.

2 Paradox Valley Unit (PVU) Data

The PVU is a program run by the U.S. Bureau of Reclamation, which has been disposing deep brine into a confined aquifer between 4.3 and 4.6 km depth in Paradox Valley, Colorado since 1995 (Ake et al., 2005; Denlinger & RH O'Connell, 2020) (Figure 1). The high-pressure fluid injection has been associated with >7000 earthquakes between 1991 and 2012, which have all been documented as induced seismicity (Ake et al., 2005; Block et al., 2015; V. M. King et al., 2016; Denlinger & RH O'Connell, 2020). Most seismic events within 5 km of the injection well were induced within the first 10 years of injection and nearly all within the high permeability injection reservoir known as the Leadville formation. This zone is highly pressurized from decades of continuous pumping and dictates the lateral migration of seismicity away from the wellbore. These carefully studied events support the notion of a $\sqrt{t}$ diffusion model for pressurization from the well (Block et al., 2015; V. M. King et al., 2016) (Figure 2). Additional ancillary data also make this an ideal study region: numerous wells that extend into deeper formations than just the Leadville aquifer, 3D seismic tomography, logs of P-wave velocity, density and porosity from the near surface to basement in the injection well, and logging of geologic units in other wells in the area (Denlinger & RH O'Connell, 2020).

Most importantly for our purposes, previous work has already compiled a detailed, fully coupled poroelastic model (Denlinger & RH O'Connell, 2020). This model is given by a grid description of nodes with corresponding parameter values which we validate in our finite element numerical model (Dassault Systemes, 2020) with improved meshing near the well where pressure and stress gradients are highest (see SM 8.1). Figure 2 includes a plot of the earthquake distribution overlaid on a cross-section of the numerical model mesh.

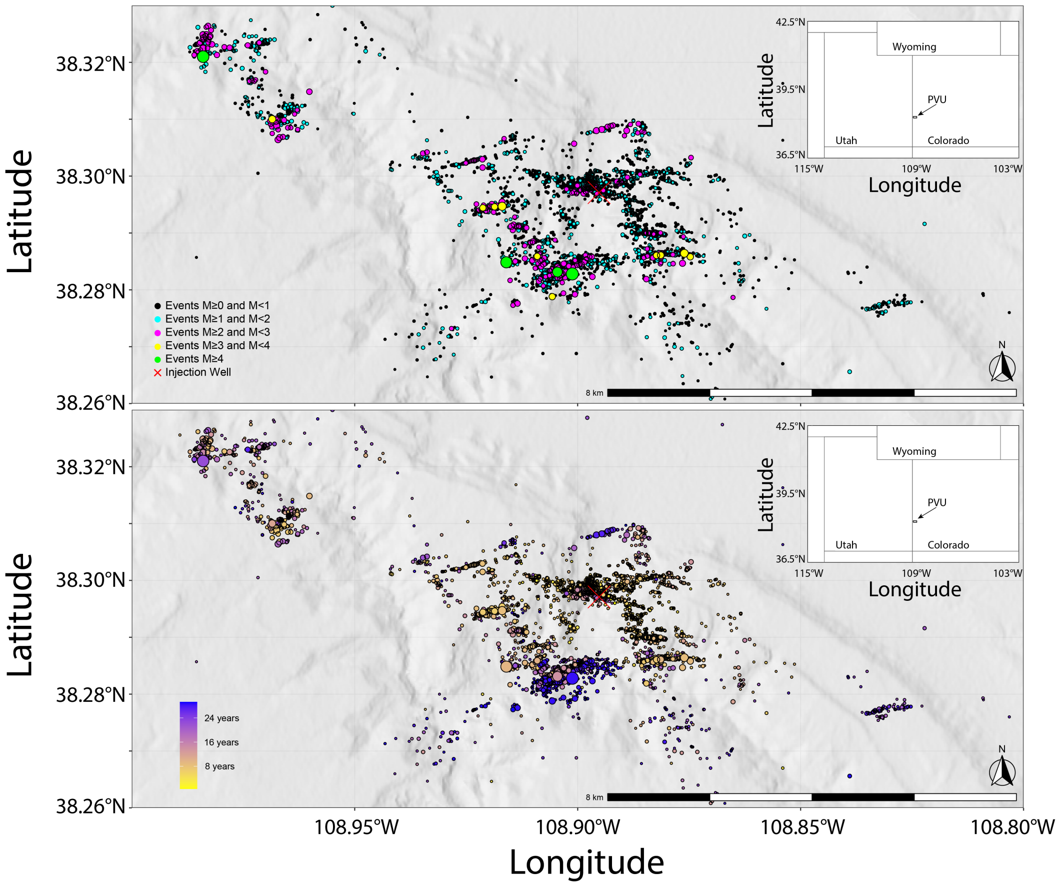

Figure 1. Regional setting of the Paradox Valley Unit, CO (PVU). a) Earthquakes binned by different magnitude ranges. The well is denoted by the red 'X'. The deep brine injection began in 1991 at a depth of 4.3 km. Most seismicity is clustered near the well, where stress perturbations are largest and fluctuate the most. b) Temporal evolution of events. There are more than 7000 earthquakes in the catalog, but within the 8 km radius around the well which we use for analysis includes only 3000.

3 Methods

The core of our methodology relies on the careful development of machine learning features which will represent the contribution of injection-driven stress changes and earthquake-driven stress change for each event in the PVU catalog. Our injection-driven stress feature is resolved using time-dependent pore pressure and stress changes throughout the PVU. Pore pressure and stress perturbations are used to produce von Mises stress features that are physical inputs for the ML/SHAP analysis. To quantify our earthquake-driven stress changes, we create a second feature in the ML/SHAP analysis, which we

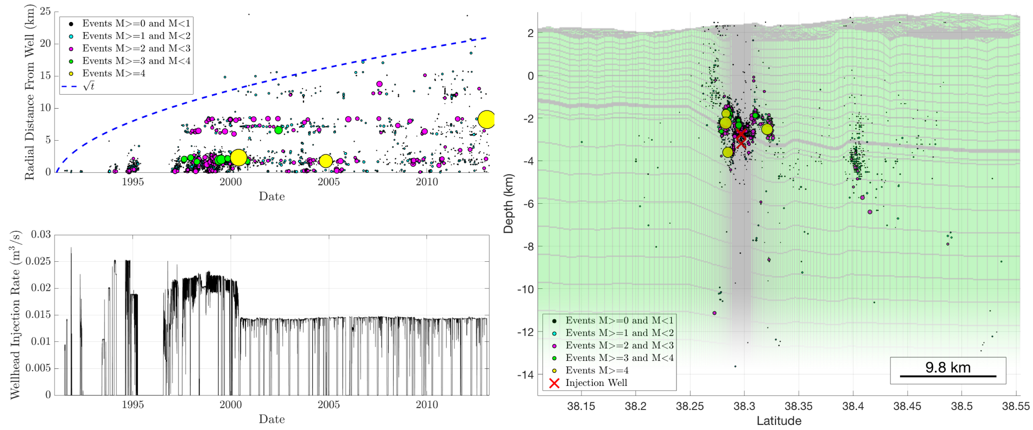

Figure 2. Earthquakes plotted as their radial distance from the well and time. Most earthquakes behave in a typical $\sqrt{t}$ diffusion rate away from the well consistent with progressive lateral migration of seismicity through the permeable Leadville (Ake et al., 2005; Block et al., 2015; Denlinger & RH O'Connell, 2020). Flow tests were performed prior to 1995. Notice injection is highest during peak injection rates ∼1997. Our model records pore pressure and stress perturbations from 10-July-1991 to 16-April-2013. Numerical model cross section with earthquake and well depth superimposed. The model is a fully-coupled poroelastic model based on prior work (Denlinger & RH O'Connell, 2020). We increase the grid discretization near the well to capture large changes in pressure gradients (see SM 8.1).

call the "earthquake feature". The earthquake feature is calculated from the stresses produced by prior earthquakes that may have generated perturbations large enough to produce the current earthquake. These two feature weights are then trained on the entire PVU catalog to find the optimal weight of each feature for each earthquake in the PVU catalog. SHAP analysis of the ML model's feature weights allow for interpretation of the relative contribution of each feature to each event. We support our interpretations of triggering mechanisms from the ML/SHAP with results from a nearest neighbor distance cluster analysis.

3.1 Numerical Model

We model the relative increase in pore pressure ΔP (scalar) and poroelastic stress ΔS (2nd order tensor) for the PVU using a model with one injection well in the center of the model domain (SM Figure 1). The hydrogeologic structure is based on a nodal distribution of parameters that we reduced down to 1000 unique unit formations and use Abaqus to resolve the linear poroelastic equations (R. G. Hill et al., 2024) (see SM 8.1). The model dimensions are 50 km by 50 km laterally with a 18 km depth. Figure 2 shows a cross-section through the well injection zone. The injection is divided across three perforated zones consistent with prior modeling and uses the entire injection history as 7952 unique daily rates in our model from 10-July-1991 to 16-April-2013 (Denlinger & RH O'Connell, 2020) (Figure 2). We output ΔP and ΔS from these daily steps across the entire domain at 284 $\sim$monthly time steps. We do not include earthquakes in our study that occur outside of the modelled time domain which is restricted by the injection history, although the earthquake catalog does extend until 31-December-2019 (Figure 2).

3.2 Stress Features

The Abaqus outputs of ΔP and ΔS were post-processed in Matlab using abaqus2matlab (Papazafeiropoulos et al., 2017). The stress features of ΔP and ΔS represent the relative change induced from the fluid injection and are resolved at the closest value in the domain to each $\sim$3000 earthquakes during our study time. We assessed a variety of different stress features during the preliminary stages of this work, consistent with prior forecasting studies (DeVries et al., 2018; Sharma et al., 2020; Qin et al., 2022). We found that von Mises stress and von Mises stressing rate were the best stress-based features for forecasting the seismicity rate and are the only two stress features we consider hereinafter. We make the assumption that the von Mises stress is resolved uniformly using a strike azimuth of 260^0 and vertical dip consistent with the most common faulting structure present from the earthquakes locations (Denlinger & RH O'Connell, 2020).

3.3 Earthquake Feature

Static stress transfer modeling can be used to assess earthquake-earthquake triggering on faults embedded in an elastic half space with homogeneous isotropic elastic properties (Lin & Stein, 2004; Toda et al., 2005). Stress transfer can promote or reduce the potential of earthquake triggering, depending on the coefficient of friction, fault geometry, and sense of slip (G. C. P. King et al., 1994; Stein, 1999). Since the exact geometries of every earthquake in our model are unknown, we choose to develop an earthquake feature that is based on the occurrence of prior earthquakes that could have plausibly influenced each earthquake.

We use 'cutde' (Thompson, 2021) to resolve elastic stress transfer produced from triangular dislocation element representations of fault slip (Nikkhoo & Walter, 2015). Several assumptions are required for the static stress transfer modeling: (1) We assume a uniform stress drop for every event of 3 MPa, (2) a shear modulus of 30 GPa, and (3) a Poisson ratio of 0.25. Under this framework we show that the von Mises stress is self-similar for both parallel and perpendicular receiver receiver planes at a given distance from the event (SM Figure 2). By varying event magnitude, we calculate a radius from the center of the dislocation that can increase the potential of failure up to a distance that intersects the 10 kPa triggering threshold (Reasenberg & Simpson, 1992; Stein, 1999). As a sensitivity test we varied the stress drop from 1-10 MPa and observe marginal change to the perturbable radius for varying magnitudes (SM Figure 2). Then, for every earthquake, we create an earthquake-to-earthquake feature, which counts the number of earthquakes that could have perturbed it. The earthquake count is represented by $\ln(N+1)$, where N is the number of perturbing earthquakes to have occurred prior to each event. Higher values of this feature indicate a higher likelihood of earthquake-earthquake interaction.

3.4 ML/SHAP Analysis

We use the machine learning technique of random forest regression (RFR) to fit our observed seismicity (Ho et al., 1995; Ho, 1998). The RFR model makes a prediction on the target variable, which are one-hot encoded occurrences of the observed earthquakes across 284 ∼monthly time steps each. We avoid overfitting and optimize model hyperparameters using an exhaustive grid search applied to a 5-fold cross-validation score. The observed seismicity is therefore repeatedly divided into training and test folds with the mean squared error evaluating fit on the test folds which the trained model does not see. The RFR models chosen for our analysis were trained using the hyperparameters derived from the best-performing model during the cross-validation process.

The input features are composed from the stress and earthquake features as well as their time lags. The time lags are introduced both to capture any potential anisotropy or hydromechanical heterogeneity that are not explicit in the numerical model as well as time delayed effects that former earthquakes or stress history may have when perturbing the current earthquake. We find that including more lags improves the overall fit of our model, up to ∼50 lags, but is likely over-fitting and unrealistic. We assume that the physical meaning of the lags are unreasonable beyond ∼1 year before the actual earthquake timing and reserve our total lags to the local minimum of 5 lags (SM Figure 3). In other words, a model can contain the current stress/earthquake feature (+0 lag), the time period prior (+1 lag), and the time periods before that (+2-+5 lag etc..) or any combination of that set (SM Figure 3).

To assess feature importance, we use SHAP, which provides a robust and self-consistent means to explain the predictions of our target variable (earthquake or no-earthquake) by computing the contribution of each feature to the prediction (Shapley et al., 1953; Lundberg & Lee, 2017). A key advantage of SHAP lies in its ability to consistently untangle the impacts of multiple correlated input variables (Trugman & Ben-Zion, 2023). Since the SHAP value is represented as an additive feature, it is a linear model and the contributions of each feature can be added to describe the contribution that the stress features have compared to the earthquake features. This is often preferable compared to permutation feature importance which chooses importance based on the decrease in model performance. Larger SHAP values for a given feature, averaged across the dataset, signify a higher importance for the model's prediction.

3.5 Cluster Analysis

As an independent test of earthquake behavior, we investigate how the PVU seismicity is distributed in magnitude, space, and time using a traditional cluster analysis. We use the nearest neighbor distance (NND) in the space-time-magnitude domain (Baiesi & Paczuski, 2004) for each pair of events i and j using the following equation:

$$\eta_{ij} = \begin{cases} t_{ij}(r_{ij})^d 10^{-bm_i}, & t_{ij} > 0; \\ \infty, & t_{ij} \leq 0 \end{cases} \tag{1}$$

Where, t_{ij} is the interevent time (year), r_{ij} is the inter event distance (km), d is the dimension of the earthquake hypocenter distribution ($d = 1.32$) determined using a box-counting procedure (Corral, 2003) (SM Figure 4), b is the b-value ($b = 0.75$) determined by maximum likelihood estimation (Aki, 1965), and m_i is the ith event magnitude (Zaliapin & Ben-Zion, 2013; Schoenball et al., 2015). The NND is separable into rescaled distance (R_{ij}) and rescaled time (T_{ij}) where (Zaliapin et al., 2008; Zaliapin & Ben-Zion, 2013):

$$\eta_{ij} = R_{ij}T_{ij} \tag{2}$$

$$R_{ij} = (r_{ij})^d 10^{-bm_i/2} \tag{3}$$

$$T_{ij} = (r_{ij})^d 10^{-bm_i/2}, \tag{4}$$

An advantage of this form of NND is that the clustering style of seismicity can be displayed by a joint 2D distribution of rescaled time $\log_{10} T_{ij}$ and rescaled distance $\log_{10} R_{ij}$ (Zaliapin et al., 2008; Zaliapin & Ben-Zion, 2013, 2016). The distribution helps to describe the type of earthquake clustering style, since observed seismicity often shows a bimodal joint distribution divided by a constant line and chosen nearest-neighbor threshold n_0. Events below this threshold are classified as clustered (i.e., earthquake-driven triggering) and the events that are above this threshold are classified as background (i.e., injection-driven or independent) (Zaliapin & Ben-Zion, 2016). We use the NND distributions for the PVU as an independent test of the physical mechanism driving each earthquake in the sequence. We hypothesize that our ML/SHAP model will preferentially separate injection-driven vs earthquake-driven events as identified by Zaliapin and Ben-Zion (2016).

4 Results

4.1 Numerical Model Results

The fully-coupled poroelastic model shows that areas with seismicity experience pore pressure increases from 0.005 MPa to 9 MPa. Most pore pressure increases occur within an 8 km radius around the injection well (SM Figures 5-10). Most seismicity occurs in close vicinity of the injection well and the ΔP is highest in early 1999 ($\sim$9 MPa). The pressure changes near the well mimic injection rate changes as the temporal delay of diffusion is negligible. Elsewhere, the diffusion process dominates the pressure changes and therefore the increase in pore pressure is more gradual through time (SM Figure 8-9). Across the domain, seismicity occurs during the highest rates of pressure increase. This observation is consistent with other instances of wastewater induced seismicity (Langenbruch et al., 2018; Qin et al., 2022). The increasing pore pressure diffuses laterally through the highly permeable Leadville formation. Low permeability confining units above and below the reservoir restrict vertical pressure migration (SM Video 1).

4.2 Cluster Analysis Results

Results of the NND cluster analysis show that a larger portion of the earthquakes are classified as the background mode (Zaliapin & Ben-Zion, 2016; Goebel et al., 2019)(Figure 3a). The constant threshold value $\eta_0 = -4.9$ is chosen based on a 1D Gaussian mixture model analysis (Zaliapin et al., 2008; Zaliapin & Ben-Zion, 2016). The clustering behavior is similar to other cases of wastewater induced seismicity (Zaliapin & Ben-Zion, 2016; Glasgow et al., 2021). There is a larger population of background events and clustered events occur at short space-time distances. These results are also dissimilar from other cases of induced seismicity that have a more clear bimodal distribution, albeit different mechanical processes are occurring (Zaliapin & Ben-Zion, 2016, e.g., Coso and Salton Sea geothermal areas). A small portion of the background domain is characterized by low R_{ij} and large T_{ij}, which often characterizes these events as repeaters (Zaliapin & Ben-Zion, 2016; Hsu et al., 2024). These events make sense in the context of single well injection. The start-stop nature of the injection means repetitive changes in stress occur at the same locations. This is observed in the pore pressure results at different clusters near the well where the pore pressure closely follows the flux of the injection (SM Figures 5-8).

4.3 ML/SHAP Model Results

Our preferred model uses the following: 1000 total trees, a maximum depth of 10, a minimum sample split of 10, and a minimum of 4 samples for a leaf node. Figure 4a shows the fit of our random forest model for two different model types. One model uses only the von Mises stress rate and earthquake feature while the other model uses both the von Mises stress and the von Mises stress rate as well as the earthquake feature (including lags). We find that the mean squared error (MSE) is slightly lower for the model that includes both stress features. However, we choose to present the parsimonious solution of one stress feature and refer the reader to the supplementary for the results including both stress features, which contains small differences to the main results (SM Figures 11-14).

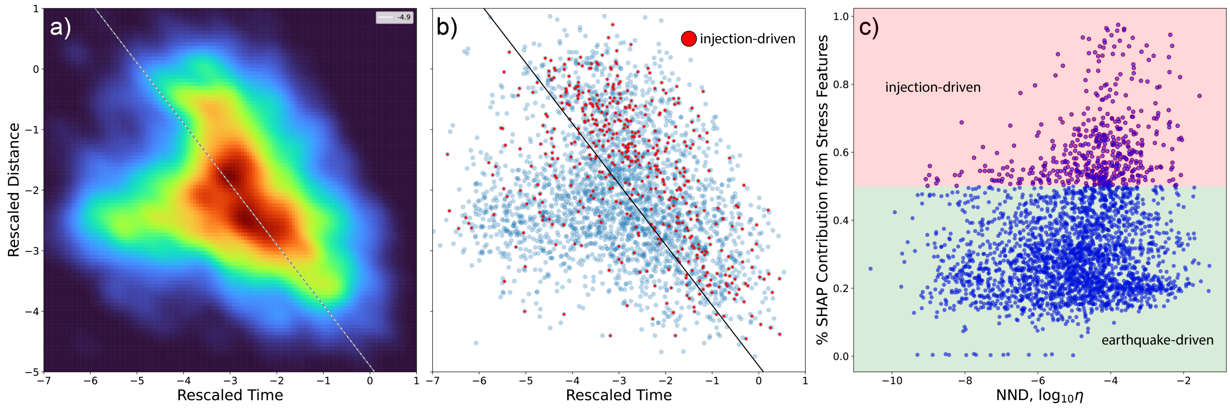

Figure 3. a) Nearest neighbor time-distance distributions for seismicity in the PVU. The color bar represents the number of event pairs. The total number of earthquakes used in this analysis is 2927. The diagonal dashed line is the η_0 background (above) and clustered (below) mode threshold. The value is a constant distance threshold determined by the 1D Gaussian mixture model and is -4.9. b) Comparing the earthquakes that have at least 50% stress feature contribution on the rescaled distance rescaled time plot. Many of the earthquakes cluster in the independent background mode with a second distribution towards the repeater mode and a few earthquakes spread out in the cluster mode. c) The SHAP stress feature contribution vs. the nearest neighbor distance value. Many of the earthquakes cluster below the 50% stress feature contribution indicating and to the left of the -4.9 cluster threshold. However, earthquakes that have >50% stress feature contribution, denoted as red circles, tends to populate the 'background' mode of the NND (to the right of -4.9). These results are consistent for earthquakes driven by stress from the injection since they act as initial parent earthquakes that trigger subsequent seismicity in a region that has experienced stress changes high enough to begin seismicity.

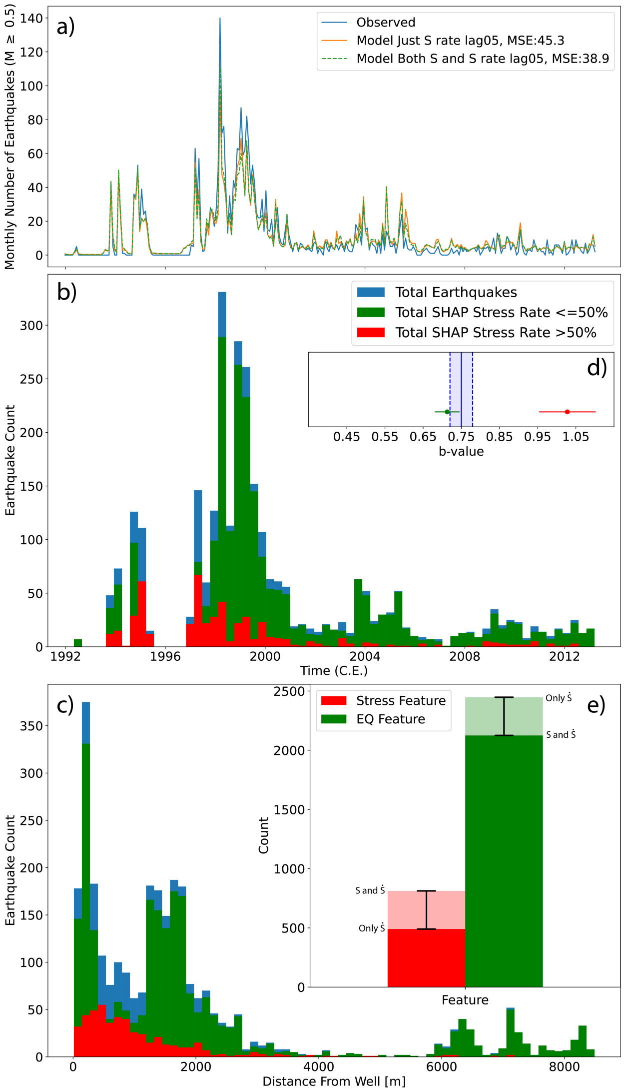

Figure 4. a) Forecasted seismicity rate across for all time steps. Orange line represents the best fit model that includes only the von-Mises stress rate. The dashed green line includes von-Mises stress and has slightly better fit. b) Earthquake count binned through time for earthquakes with SHAP stress rate <=50% (ie. earthquake-driven green) and >50% (ie. injection-driven red). c) same as panel b, but for distance away from well. d) b-value analysis of all earthquakes (blue), earthquake-driven (green), and injection-driven (red). e) Ratio of all earthquakes with a larger sum of SHAP value for stress features (red) and the earthquake features (green). We reflect the uncertainty of triggering mechanism based on our two models described in panel a.

The SHAP analysis results are summarized in SM Figure 15. We output the results exclusively at the time when the earthquakes occur since we are only interested in discerning the contribution of the stress features at that time. A summary of the SHAP contributions for all time, not just when the earthquakes occur, is presented in the supplementary material (SM Figure 16). The feature with the higher overall impact on the model is the perturbable earthquake feature that represents the number of earthquakes that occurred during the chosen time step that could have potentially perturbed the earthquake in question. The next most important features, with nearly equal importance, are the lagged von Mises stress rates. These stress features are considerably less important on average compared with the earthquake feature.

To assess the total contribution of the stress features vs the earthquake features, we compare the cumulative feature results. Separating which earthquakes are dominated by cumulative feature importance, Figure 4e shows that the ratio of earthquakes that have a higher stress feature contribution compared to earthquakes that have a higher total earthquake feature contribution is about 1:5. We examined the sensitivity of this since it would be expected that increasing lags may contribute to higher contribution to stress. While the stress contribution does increase for models that include 0,+1,+2 lags, after the model reaches +3 lags, earthquakes that are considered to have a higher total stress contribution increase marginally. For example, from +3 lags to +5 lags the ratio has a percent increase of only $\sim$0.5% (SM Figure 17). We do not pursue sensitivity past +5 lags as the SHAP analysis is computationally expensive with increasing features. It is important to note that when testing increasing lag sensitivity, the overall ratio of the total number of stress features to earthquake features remains the same.

5 Discussion

The ML/SHAP model identifies injection-driven earthquakes (ie. >50% stress feature contribution) predominantly as background events in the NND model (Figure 3b-c). In the NND model, background events are mostly the independent Poisson mode (Zaliapin et al., 2008; Zaliapin & Ben-Zion, 2016). This suggests injection-driven earthquakes often act as parent earthquakes, likely induced by pore pressure and stress changes, triggering further seismicity. These results are further supported by the relative timing of these earthquakes, which often occur at the beginning of injection stages (Figure 4b). We statistically compare injection-driven event distribution to the larger catalog using a two-sample Kolmogorov–Smirnov test, which rejects the null hypothesis of identical distributions with 99% confidence (SM Figure 18).

We explored two interevent time measures to analyze event timing between injection-driven and earthquake-driven classes (Davidsen et al., 2021). The first measure, interevent time ratio R, indicates deviations from a Poisson process (Van Der Elst & Brodsky, 2010; Davidsen et al., 2017). Rejecting the Poisson process hypothesis with >95% confidence, we observe a significant peak at $R = 0$ suggesting triggering, and another at $R = 1$ indicating longer intervals likely due to stress changes stimulated by a non-random process (SM Figure 19). Injection-driven earthquakes show less bi-modal distribution, implying less temporal clustering than earthquake-driven ones. The second measure, the Bi-test, also indicates temporal clustering and rejects the Poisson process hypothesis with >95% confidence (Bi et al., 1989; Baró et al., 2014). Injection-driven earthquakes exhibit lower temporal clustering (lower fluctuation in H values) compared to clearly clustered earthquake-driven ones (higher fluctuation in H values around 0 and 1) (SM Figure 20).

We also analyze the spatiotemporal distribution of injection-driven earthquakes (Figure 4b-c). They tend to occur earlier in injection history and cluster near the injection well, contrasting with earthquake-driven earthquakes. These events coincide with sharp stress field changes near the well, often preceding clustered seismicity. The b-value of injection-driven earthquakes (Figure 4d) is notably higher (1.03) compared to overall seismicity (0.75) and earthquake-driven events (0.71). This suggests that injection-driven events tend to have lower magnitudes, on average, than the earthquake-driven events and a b-value closer to 1 indicates that these events may appear to mimic independent background events. The finding that earthquake-driven events produce lower b-values and characterize more of the large events in induced catalogs may have implications for maximum magnitude estimates of induced earthquakes, since initial injection-driven earthquakes at the onset of induced sequences might underestimate the overall maximum magnitude of triggered seismicity

Clusters of seismic activity away from the well are noticeable, yet they have fewer stress-dominated earthquakes (SM Figure 21). Often, clusters away from the well are initiated by a few injection-driven earthquakes. This observation is consistent with the machine learning process since earthquakes that had no prior earthquakes would not be expected to have a strong prior earthquake feature contribution. However, not all injection-driven earthquakes precede nearby seismic events. Additionally, areas lacking clear clustering seem to host multiple injection-driven earthquakes, suggesting varied driving mechanisms in those regions (SM Figure 21).

It is important to recognize that uncertainty is introduced in the model at various stages: physical model material parameters, static stress transfer parameters, RFR input features, and the number of included lags. We affirm the numerical model (see SM 8.1 and SM Figures 5-10) and show that the static stress transfer at a triggering threshold of 10 kPa is only marginally sensitive to varied stress drop assumptions (SM Figure 2). We find that increasing lags beyond +3 does not greatly change the ratio of injection-driven and earthquake-driven earthquakes (SM Figure 17). The main model sensitivity lies in input features: incorporating von Mises stress and rate increases injection-driven earthquakes from 17% to 27% (Figure 4e and SM Figure 14). It is unclear whether including both the stress and stress rate features provides a better model since more injection-driven earthquakes also begin to populate the cluster mode, which we assume is a product of over-fitting the seismicity rate (Figure 4a and SM Figure 13). We therefore suggest that these two models may provide estimates on the lower and upper bound with the true portion of injection-driven earthquakes at approximately 22$\pm$5% of the total.

Results of this study indicate that the physics-based model, with RFR and SHAP analysis, accounts for a significant portion of independent background mode events found in NND cluster analysis. However, not all background mode events are classified as injection-driven. The absence of a clear bi-modal distribution in NND analysis suggests that events populating the independent background mode may have less direct fluid injection influence (Zaliapin & Ben-Zion, 2016; Glasgow et al., 2021). We expect this ratio of injection-driven vs earthquake-driven seismicity to vary by geologic region, stress state, distribution of preexisting faults, and injection style. Understanding this ratio is crucial for wastewater management, as it impacts induced seismic hazard. Sites where seismicity is mainly earthquake-driven would be harder to control via well operations best practices (R. G. Hill et al., 2024), while sites with mostly injection-driven events may be more manageable. Identifying the triggering process in candidate sites can guide energy production decisions, avoiding areas prone to severe triggered seismicity.

6 Conclusion

We decipher induced earthquake triggering mechanisms using a 3D fully-coupled poroelastic model of brine injection and a random forest machine learning model trained on more than 20 years of induced earthquakes at Paradox Valley Unit, Colorado. Our simple ML/SHAP feature training approach, using one injection-driven feature and one earthquake-driven feature, allows for the separation of events that are more likely injection-driven from events that are more likely earthquake-driven in the sequence. Comparing the ML/SHAP results with a nearest-neighbor cluster analysis reveals good agreement in stress contribution and cluster style. Our methodology finds that injection-driven earthquakes make up only 22±5% of the catalog and have distinct spatiotemporal clustering with a larger b-value, closer proximity to the well and earlier occurrence in the injection history. Our method may be applicable to other regions to help determine the site susceptibility to earthquake triggering or aid in declustering induced catalogs.

7 Open Research

Data of Abaqus files, post-processing scripts, ML model scripts, and figure generation scripts are available online at Hill, R. (2024) (`https://doi.org/10.5281/zenodo.10967359`).

The wastewater injection data and earthquake data is available from the Bureau of Reclamation Upper Colorado Basin website (`https://https://www.usbr.gov/uc/progact/paradox/index.html`).

The numerical models were built and solved using the software Abaqus (Dassault Systemes, 2020).

Acknowledgments

The authors appreciate discussion with Robert Guyer at early stages of the work. We acknowledge use of the CSRC high-performance computing cluster and other support from San Diego State University. D.T.T acknowledges support from NSF Award EAR-2121666.

References

Ake, J., Mahrer, K., O'Connell, D., & Block, L. (2005). Deep-injection and closely monitored induced seismicity at paradox valley, colorado. *Bulletin of the Seismological Society of America*, *95*(2), 664–683.

Aki, K. (1965). Maximum likelihood estimate of b in the formula log n= a-bm and its confidence limits. *Bull. Earthquake Res. Inst., Tokyo Univ.*, *43*, 237–239.

Bachmann, C. E., Wiemer, S., Goertz-Allmann, B., & Woessner, J. (2012). Influence of pore-pressure on the event-size distribution of induced earthquakes. *Geophysical Research Letters*, *39*(9).

Baiesi, M., & Paczuski, M. (2004). Scale-free networks of earthquakes and aftershocks. *Physical review E*, *69*(6), 066106.

Baró, J., Martín-Olalla, J.-M., Romero, F. J., Gallardo, M. C., Salje, E. K., Vives, E., & Planes, A. (2014). Avalanche correlations in the martensitic transition of a cu–zn–al shape memory alloy: Analysis of acoustic emission and calorimetry. *Journal of Physics: Condensed Matter*, *26*(12), 125401.

Bear, J. (1988). *Dynamics of fluids in porous media.* Courier Corporation.

Bi, H., Börner, G., & Chu, Y. (1989). Correlations in the absorption lines of the quasar q0420-388. *Astronomy and Astrophysics (ISSN 0004-6361), vol. 218, no. 1-2, July 1989, p. 19-23.*, *218*, 19–23.

Biot, M. A. (1941). General theory of three-dimensional consolidation. *J. Appl. Phys.*, *12*(2), 155–164. Retrieved 2021-04-13, from `https://urldefense.com/v3/__http://aip.scitation.org/doi/10.1063/1.1712886__;!!Mih3wA!E0xCUAx3ctL8wKS_tp-pNn95UaeXh_lRKy7b2Mcg4-S1_-Ss2NOb2nM5ld42UzHIa8rqXMpIajp0q38i$` doi: 10.1063/1.1712886

Block, L. V., Wood, C. K., Yeck, W. L., & King, V. M. (2015). Induced seismicity constraints on subsurface geological structure, paradox valley, colorado. *Geophysical Journal International*, *200*(2), 1172–1195.

Brown, M. R., & Ge, S. (2018). Small earthquakes matter in injection-induced seismicity. *Geophysical Research Letters*, *45*(11), 5445–5453.

Cacace, M., Hofmann, H., & Shapiro, S. A. (2021). Projecting seismicity induced by complex alterations of underground stresses with applications to geothermal systems. *Scientific Reports*, *11*(1), 23560.

Cocco, M. (2002). Pore pressure and poroelasticity effects in coulomb stress analysis of earthquake interactions. *J. Geophys. Res.*, *107*, 2030.

Corral, A. (2003). Local distributions and rate fluctuations in a unified scaling law for earthquakes. *Physical Review E*, *68*(3), 035102.

Dassault Systemes, . (2020). *Abaqus (version 2019).* Retrieved from `https://urldefense.com/v3/__https://www.3ds.com/products-services/simulia/products/abaqus/__;!!Mih3wA!EOxCUAx3ctL8wKS_tp-pNn95UaeXh_lRKy7b2Mcg4-S1_-Ss2N0b2nM5ld42UzHIa8rqXMpIag2Io7P8$`

Davidsen, J., Goebel, T., Kwiatek, G., Stanchits, S., Baró, J., & Dresen, G. (2021). What controls the presence and characteristics of aftershocks in rock fracture in the lab? *Journal of Geophysical Research: Solid Earth*, *126*(10), e2021JB022539.

Davidsen, J., Kwiatek, G., Charalampidou, E.-M., Goebel, T., Stanchits, S., Rück, M., & Dresen, G. (2017). Triggering processes in rock fracture. *Physical review letters*, *119*(6), 068501.

Denlinger, R. P., & RH O'Connell, D. (2020). Evolution of faulting induced by deep fluid injection, paradox valley, colorado. *Bulletin of the Seismological Society of America*, *110*(5), 2308–2327.

DeVries, P. M., Viégas, F., Wattenberg, M., & Meade, B. J. (2018). Deep learning of aftershock patterns following large earthquakes. *Nature*, *560*(7720), 632–634.

Ellsworth, W. L. (2013). Injection-induced earthquakes. *Science*, *341*(6142).

Ge, S., & Saar, M. O. (2022). Induced seismicity during geoenergy development—a hydromechanical perspective. *Journal of Geophysical Research: Solid Earth*, *127*(3), e2021JB023141.

Glasgow, M., Schmandt, B., Wang, R., Zhang, M., Bilek, S. L., & Kiser, E. (2021). Raton basin induced seismicity is hosted by networks of short basement faults and mimics tectonic earthquake statistics. *Journal of Geophysical Research: Solid Earth*, *126*(11), e2021JB022839.

Goebel, T., Rosson, Z., Brodsky, E., & Walter, J. (2019). Aftershock deficiency of induced earthquake sequences during rapid mitigation efforts in oklahoma. *Earth and Planetary Science Letters*, *522*, 135–143.

Harr, C. (1988). Final geological well report. *US Bureau of Reclamation Test Well*(1).

Hill, R. (2024). *Data and Code for Modeling Paradox Valley Unit [Data Set].* Zenodo. Retrieved from `pending`

Hill, R. G., Weingarten, M., Langenbruch, C., & Fialko, Y. (2024). Mitigation and optimization of induced seismicity using physics-based forecasting. *JGR: Solid Earth (in review)*. (in review)

Ho, T. K. (1998). The random subspace method for constructing decision forests. *IEEE transactions on pattern analysis and machine intelligence*, *20*(8), 832–844.

Ho, T. K., et al. (1995). Proceedings of 3rd international conference on document analysis and recognition. In *Proceedings of 3rd international conference on document analysis and recognition.*

Hsu, Y.-F., Zaliapin, I., & Ben-Zion, Y. (2024). Informative modes of seismicity in nearest-neighbor earthquake proximities. *Journal of Geophysical Research: Solid Earth*, *129*(3), e2023JB027826.

Keranen, K. M., & Weingarten, M. (2018). Induced seismicity. *Annual Review of Earth and Planetary Sciences*, *46*, 149–174.

Keranen, K. M., Weingarten, M., Abers, G. A., Bekins, B. A., & Ge, S. (2014). Sharp increase in central oklahoma seismicity since 2008 induced by massive wastewater injection. *Science*, *345*(6195), 448–451.

King, G. C. P., Stein, R. C., & Lin, J. (1994). Static stress change and the triggering of earthquakes. *Bull. Seism. Soc. Am.*, *84*, 935–953.

King, V., & Block, L. (2019, Aug). *Paradox valley seismic and injection data - amerigeoss community platform datahub. (beta).* Retrieved from `https://urldefense.com/v3/__https://data.amerigeoss.org/dataset/paradox-valley-seismic-and-injection-data__;!!Mih3wA!E0xCUAx3ctL8wKS_tp-pNn95UaeXh_lRKy7b2Mcg4-S1_-Ss2N0b2nM5ld42UzHIa8rqXMpIaj50ioAx$`

King, V. M., Block, L. V., & Wood, C. K. (2016). Pressure/flow modeling and induced seismicity resulting from two decades of high-pressure deep-well brine injection, paradox valley, colorado. *Geophysics*, *81*(5), B119–B134.

Langenbruch, C., Weingarten, M., & Zoback, M. D. (2018). Physics-based forecasting of man-made earthquake hazards in oklahoma and kansas. *Nature communications*, *9*(1), 1–10.

Levandowski, W., Weingarten, M., & Walsh III, R. (2018). Geomechanical sensitivities of injection-induced earthquakes. *Geophysical Research Letters*, *45*(17), 8958–8965.

Lin, J., & Stein, R. S. (2004). Stress triggering in thrust and subduction earthquakes and stress interaction between the southern san andreas and nearby thrust and strike-slip faults. *Journal of Geophysical Research: Solid Earth*, *109*(B2).

Lundberg, S. M., & Lee, S.-I. (2017). A unified approach to interpreting model predictions. *Advances in neural information processing systems*, *30*.

Nikkhoo, M., & Walter, T. R. (2015). Triangular dislocation: an analytical, artefact-free solution. *Geophysical Journal International*, *201*(2), 1119–1141.

Papazafeiropoulos, G., Muñiz-Calvente, M., & Martínez-Pañeda, E. (2017). Abaqus2matlab: A suitable tool for finite element post-processing. *Adv. Eng. Softw.*, *105*, 9–16.

Qin, Y., Chen, T., Ma, X., & Chen, X. (2022). Forecasting induced seismicity in oklahoma using machine learning methods. *Scientific Reports*, *12*(1), 9319.

Reasenberg, P. A., & Simpson, R. W. (1992). Response of regional seismicity to the static stress change produced by the loma prieta earthquake. *Science*, *255*(5052), 1687–1690.

Rice, J. R., & Cleary, M. P. (1976). Some basic stress diffusion solutions for fluid-saturated elastic porous media with compressible constituents. *Rev. Geophys.*, *14*(2), 227. Retrieved 2021-04-13, from `https://urldefense.com/v3/__http://doi.wiley.com/10.1029/RG014i002p00227__;!!Mih3wA!E0xCUAx3ctL8wKS_tp-pNn95UaeXh_lRKy7b2Mcg4-S1_-Ss2N0b2nM5ld42UzHIa8rqXMpIai1FHNoQ$` doi: 10.1029/RG014i002p00227

Roeloffs, E., & Denlinger, R. (2009). An axisymmetric coupled flow and deformation model for pore pressure caused by brine injection in paradox valley, colorado: Implications for the mechanisms of induced seismicity. *Preliminary Report to the Bureau of Reclamation*.

Rudnicki, J. W. (1986). Fluid mass sources and point forces in linear elastic diffusive solids. *Mechanics of Materials*, *5*(4), 383-393. Retrieved from `https://urldefense.com/v3/__https://www.sciencedirect.com/science/article/pii/0167663686900426__;!!Mih3wA!E0xCUAx3ctL8wKS_tp-pNn95UaeXh_lRKy7b2Mcg4-S1_-Ss2N0b2nM5ld42UzHIa8rqXMpIahGXh2Vz$` doi: https://urldefense.com/v3/__https://doi.org/10.1016/0167-6636(86)90042-6__;!!Mih3wA!E0xCUAx3ctL8wKS_tp-pNn95UaeXh_lRKy7b2Mcg4-S1_-Ss2N0b2nM5ld42UzHIa8rqXMpIarQvXa1P$

Schoenball, M., Davatzes, N. C., & Glen, J. M. (2015). Differentiating induced and natural seismicity using space-time-magnitude statistics applied to the coso geothermal field. *Geophysical Research Letters*, *42*(15), 6221–6228.

Segall, P., & Lu, S. (2015). Injection-induced seismicity: Poroelastic and earthquake nucleation effects. *Journal of Geophysical Research: Solid Earth*, *120*(7), 5082–5103.

Shapley, L. S., et al. (1953). A value for n-person games.

Sharma, S., Hainzl, S., Zöeller, G., & Holschneider, M. (2020). Is coulomb stress the best choice for aftershock forecasting? *Journal of Geophysical Research: Solid Earth*, *125*(9), e2020JB019553.

Shirzaei, M., Ellsworth, W. L., Tiampo, K. F., González, P. J., & Manga, M. (2016). Surface uplift and time-dependent seismic hazard due to fluid injection in eastern texas. *Science*, *353*(6306), 1416–1419.

Stein, R. S. (1999). The role of stress transfer in earthquake occurrence. *Nature*, *402*(6762), 605–609.

Stokes, S. M., Ge, S., Brown, M. R., Menezes, E. A., Sheehan, A. F., & Tiampo, K. F. (2023). Pore pressure diffusion and onset of induced seismicity. *Journal of Geophysical Research: Solid Earth*, *128*(3), e2022JB026012.

Thompson, B. (2021). *cutde.* Retrieved from `https://github.com/tbenthompson/cutde`

Toda, S., Stein, R. S., Richards-Dinger, K., & Bozkurt, S. B. (2005). Forecasting the evolution of seismicity in southern california: Animations built on earthquake stress transfer. *Journal of Geophysical Research: Solid Earth*, *110*(B5).

Townend, J., & Zoback, M. D. (2000). How faulting keeps the crust strong. *Geology*, *28*(5), 399–402.

Trugman, D. T., & Ben-Zion, Y. (2023). Coherent spatial variations in the productivity of earthquake sequences in california and nevada. *The Seismic Record*, *3*(4), 322–331.

Van Der Elst, N. J., & Brodsky, E. E. (2010). Connecting near-field and far-field earthquake triggering to dynamic strain. *Journal of Geophysical Research: Solid Earth*, *115*(B7).

Wang, H. (2000). *Theory of linear poroelasticity: With applications to geomechanics and hydrogeology.* Princeton, New Jersey: 287 pp., Princeton Univ. Press.

Weingarten, M., Ge, S., Godt, J. W., Bekins, B. A., & Rubinstein, J. L. (2015).

High-rate injection is associated with the increase in us mid-continent seismicity. *Science*, *348*(6241), 1336–1340.

Zaliapin, I., & Ben-Zion, Y. (2013). Earthquake clusters in southern california i: Identification and stability. *Journal of Geophysical Research: Solid Earth*, *118*(6), 2847–2864.

Zaliapin, I., & Ben-Zion, Y. (2016). Discriminating characteristics of tectonic and human-induced seismicity. *Bulletin of the Seismological Society of America*, *106*(3), 846–859.

Zaliapin, I., Gabrielov, A., Keilis-Borok, V., & Wong, H. (2008). Clustering analysis of seismicity and aftershock identification. *Physical review letters*, *101*(1), 018501.

8 Supplementary

8.1 Model Pre-processing

A variety of issues and subsequent solutions arose in the model preprocessing that is important to elaborate on. As mentioned, previous work already compiled resources into a comprehensive, fully coupled poroelastic model of the PVU (Denlinger & RH O'Connell, 2020). However, this model was not easily portable to Abaqus and lacked sufficient discretization to capture large pressure gradients near the well. The methodology used to transfigure the initial model are presented here. We compare the model to a well known analytical solution and observed wellhead pressures to confirm its robustness.

8.1.1 Material Parameters and Meshing

The first difficulty with the Denlinger and O'Connel (D&O) model (Denlinger & RH O'Connell, 2020) is that the poroelastic material parameters are all defined at the nodes of the mesh. In Abaqus, there are a few material parameters defined at the nodes (pore pressure, void ratio, and saturation), but the elements (hexahedrons defined spatially by 8 nodes) are assigned other material parameters (ie. Young's modulus and bulk modulus of solid grains). After simple conversions of the given material parameters in the D&O model to the values used in Abaqus, we thought the best way to solve the issue of defining the *node only* values to elements would be to average the 8 nodal coordinates that make up a hexahedron element to the value at that element.

However, the averaging proved ineffective for a variety of reasons. First, the D&O model near the region of the well head experiences strong changes in material values. The Leadville formation, the high permeable injection formation, is embedded in low permeable material. The nodal change between these materials was actually only 1 node thick in some instances so by taking the average of 8 nodes resulted in significantly reducing the order of magnitude of material permeability for areas near fluid injection. Second, the strong changes in material values coupled with the large spatial discretization of the D&O model near the wellhead resulted in unrealistic gradients and convergence issues.

Therefore, in order to solve the issues present with the conversion of the D&O model to Abaqus, we decided to make several adjustments to our model that we believe make it a stronger model overall. First, we decided to reduce the spatial discretization near the well head. The well head is actually composed of 3 separate perforated injection zones and creates strong pressure gradients that require smaller spatial sampling in order to capture the large and rapid changes there. This is difficult to do based on the previous mesh since preserving spatial features such as dipping beds and down scaling material features is not straight forward. Thankfully, the vertical discretization was already well defined by the D&O model so the only change to the discretization was the horizontal directions. We solved this problem by preserving the number of elements whilst changing the horizontal spacing to grow exponentially from the location of the well head. Then, the vertical spacing and material parameters of the D&O model are preserved in the smaller spacing by using a nearest point search measured in Euclidean distance. The spatial meshing changes between the D&O model and ours are shown in Figure 1.

The second adjustment we made was in the determination of material parameters throughout the model. As previously mentioned the D&O model allows for entirely unique material parameters at every node, which caused difficulties in convergence for Abaqus. Using the newly discretized mesh of nodes/elements, and their associated material parameters, we applied a k-medoids clustering algorithm to cluster the nodes/elements based on similar material metrics across the combined set of materials. K-medoids is similar to k-means clustering, but instead of choosing the average from the kth cluster it chooses an actual data point as the center of the cluster. We worked with several different material cluster values, but ultimately decided on 1000. At this number, the model preserves many of the naturally occurring geological features such as the layered beds and salt domes whilst also maintaining a high level of material contrast near the wellhead without generating drastic gradients.

8.1.2 FEM Results Compared to Analytical Solution/Observation

A well known analytical solution exists to describe the spatial and temporal evolution of pore pressure due to continuous fluid injection into a poroelastic full space (Rudnicki, 1986). In order to gauge the success of the model, we first compare this solution to the 3D model using homogeneous material parameters. Additionally, we reduce the 3 injection nodes to a single node to better reflect the analytical solution. The radial analytical solution of pore pressure is compared with the closest radial axis given by the nodes shown in Figure 22. The solution for pore pressure matches well to the analytical solution after 10 days of constant injection using a typical bulk value of the crust as shown in Figure 23.

One thing to note is that the solution of pore pressure increases rapidly closer to the point of injection. The strong pressure gradients at this location require smaller elements then the horizontal discretization in the D&O model (200 m).

With the model now confirmed in the simplest case it was time to test a variety of k-medoid models, as previously described, and compare them to the observed wellhead pressures to confirm that the model was capable of capturing the observations. It is important to note that any complex model will result in overfitting of the wellhead data, and thus poor predictive ability for future data.

There has been a plethora of previous work from observational drilling to pressure-flow modeling designed to capture the reservoir permeability structure (V. King & Block, 2019). These different observations and modeling have provided a sizeable range of permeability values. For example, the permeability of intact limestone and dolomite varies from 0.01 to 0.1 mD (Bear, 1988). Fracturing is expected to increase permeability outside of this laboratory setting. Drill stem tests gave an original permeability of 7.97 mD, yet at the same time additional analysis indicated permeability between 1.3 and 1.5 mD. Samples from a well 4.6 km to the northeast yielded permeability ranges of 0.03 to 1.3 mD (Harr, 1988). An earlier model by Denlinger and Roeloffs (Roeloffs & Denlinger, 2009) arrived at a permeability in the injection zone of 28 mD, with significantly lower values for the other formations. Additional pressure-flow models also arrive at ranges of 9.06 to 29.2 mD for certain injection phases (V. King & Block, 2019). The current *best* model (the D&O model) throughout the entire model domain, only has a maximum permeability of 1.97 mD. The final 1000 k-medoids model, modeled at constant injection rate (typical daily average from PVU injection data), is compared with several hypothetical analytical solutions for constant injection rate for a range of bulk permeabilities in Figure 24.

The final 3D heterogeneous model compares well with a range of typical observational values and observed wellhead pressures. In the near-field, the permeability matches the higher permeability analytical solutions as expected since there is likely fractured media in this location (V. King & Block, 2019). In the far-field, where the permeability structure is expected to decrease, the model approaches the lower permeability analytical solution. For the future, it will likely be important to test a variety of physics based models to understand the sensitivity introduced in the machine learning. However, we are confident in the evidence presented that our current model, adopted from the D&O model, is robust enough to continue with the primary goal of this work.

671 ## 8.2 Supplementary Figures

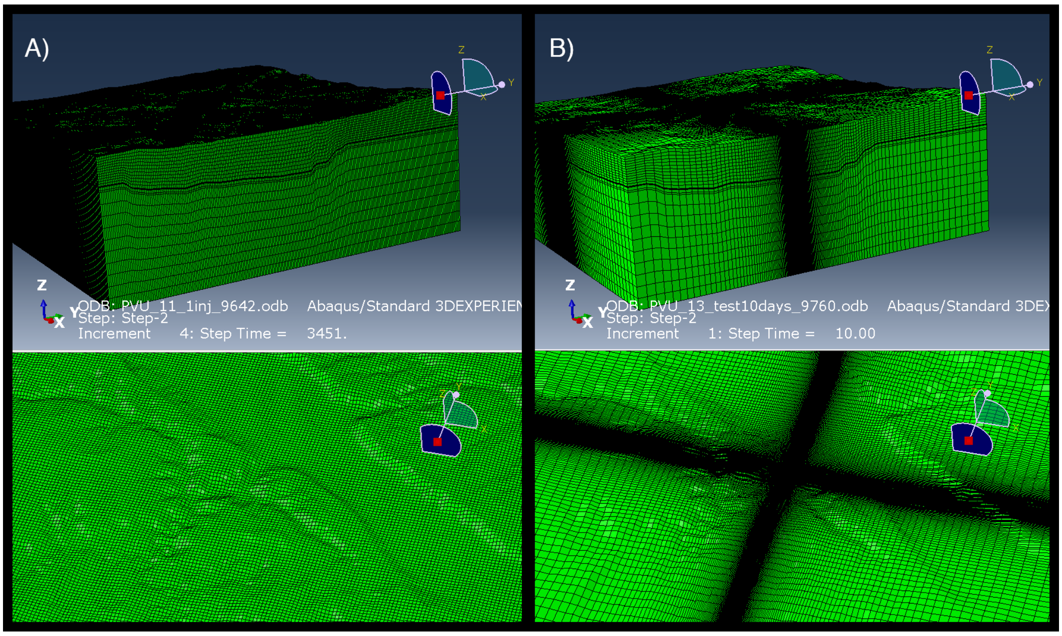

Figure 1. Previous model mesh from D&O model (Panel A) with surface view of well location compared to (Panel B) our smaller discretized model with similar surface view.

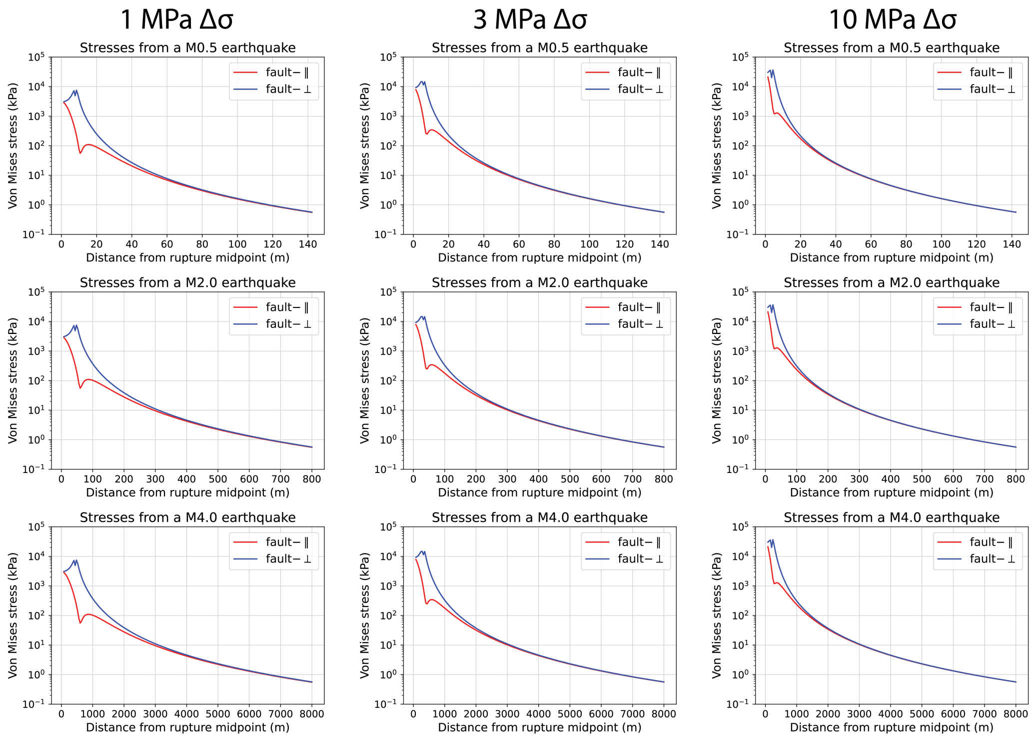

Figure 2. The von Mises stress in kPa for the three varying earthquake magnitudes (0.5, 2.0, and 4.0) for three varying stress drops (1, 3, and 10 MPa). We use cutde (Thompson, 2021) to resolve stress transfer produced from fullspace triangle dislocation elements assuming a uniform stress drop, a shear modulus of 30 GPa, and a Poisson ratio of 0.25. We show that the von Mises stress is self similar for opposite receiver planes at certain distances, dependent on the magnitude, produced by the dislocation. We use thetriggering threshold of 10 kPa (Reasenberg & Simpson, 1992; Stein, 1999) which increases depending on the magnitude size. This distance is our perturbable radius used for the earthquake feature.

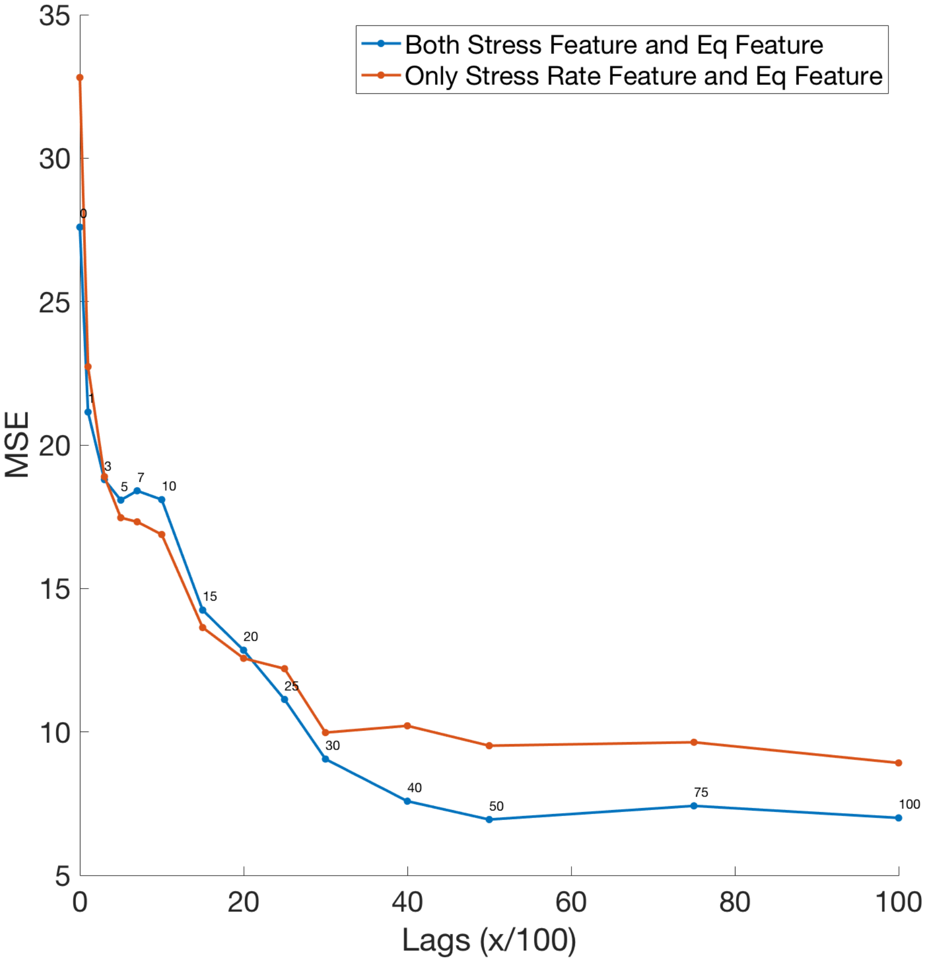

Figure 3. A sensitivity test to increasing and the overall MSE fit to the seismicity rate. We find that there is a local minimum near 5 lags. The fit does not improve after approximately 50 lags.

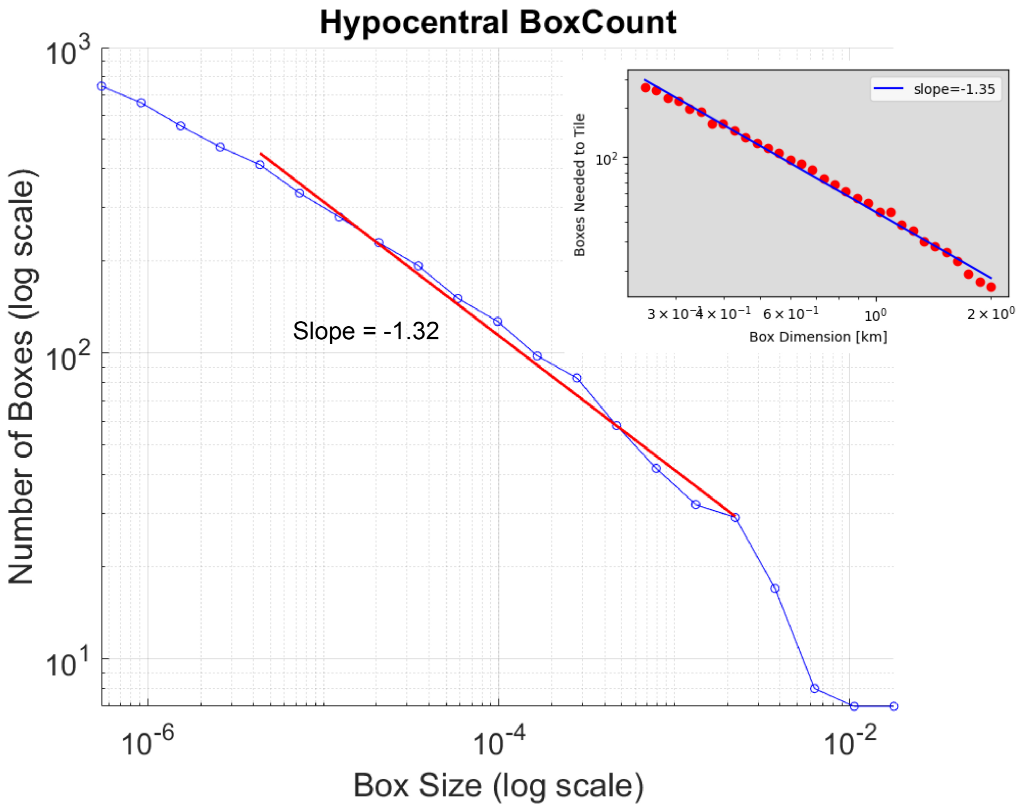

Figure 4. Hypocentral and epicentral (inlet) box-counting procedures with good agreement on the fractal dimension d_f=1.32 of the earthquakes at Paradox Valley.

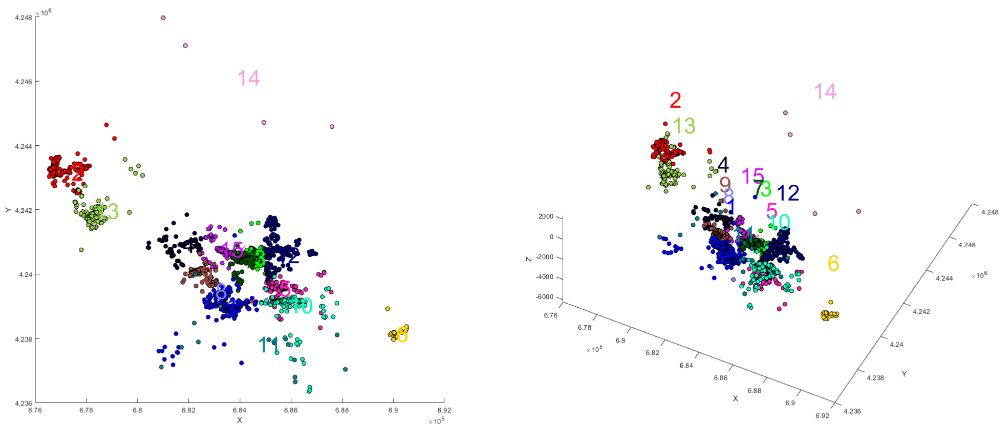

Figure 5. Different k-means cluster locations (1-15) of seismicity for the PVU. We extract the pore pressure at the center of each seismicity cluster from the numerical model in the subsequent figures. We include results for the near well cluster (7), two further regions with more diffuse responses (4) and (10) as well as farther distance (2) and (6).

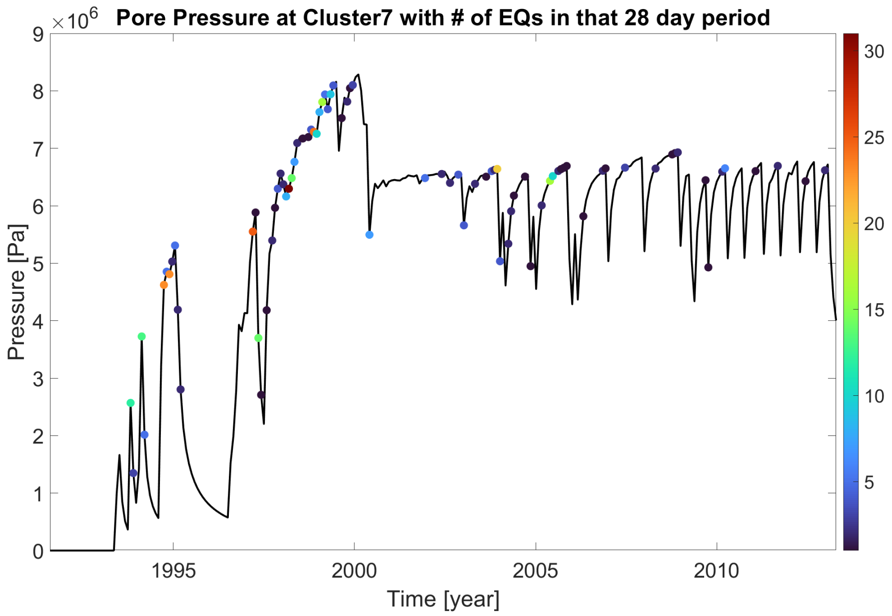

Figure 6. Cluster 7 near the well and pore pressure profile at the center of cluster. The pore pressure mimics the injection well rates due its close vicinity to the well.

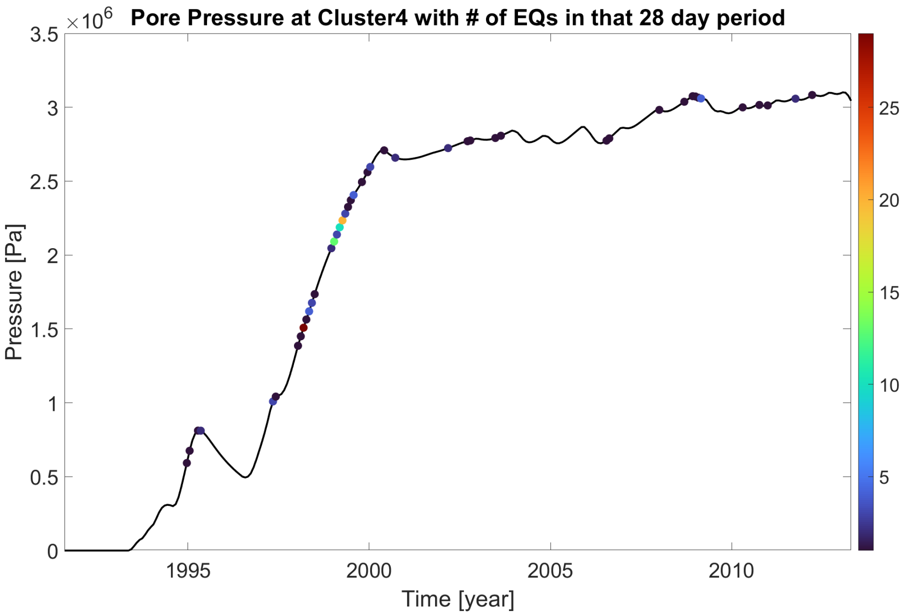

Figure 7. Cluster 4.

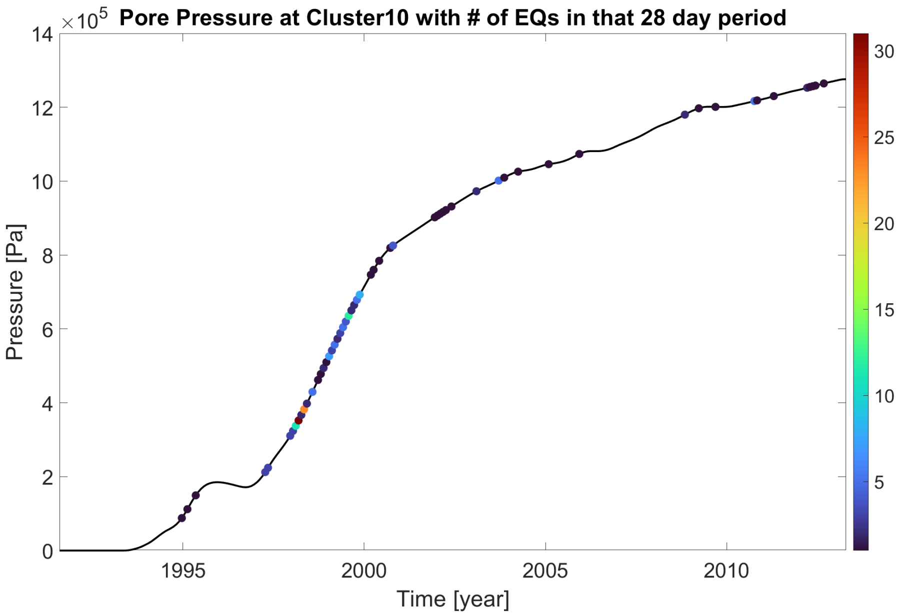

Figure 8. Cluster 10.

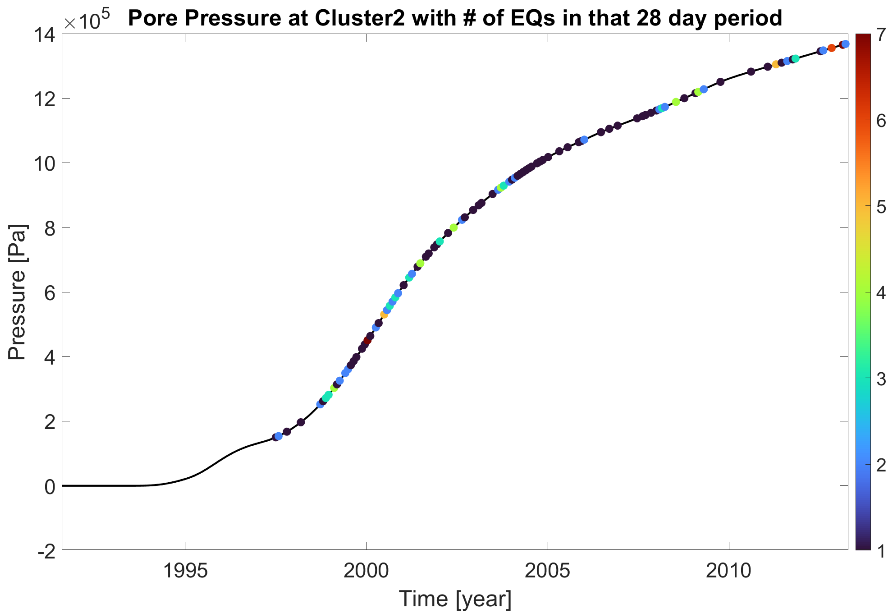

Figure 9. Cluster 2.

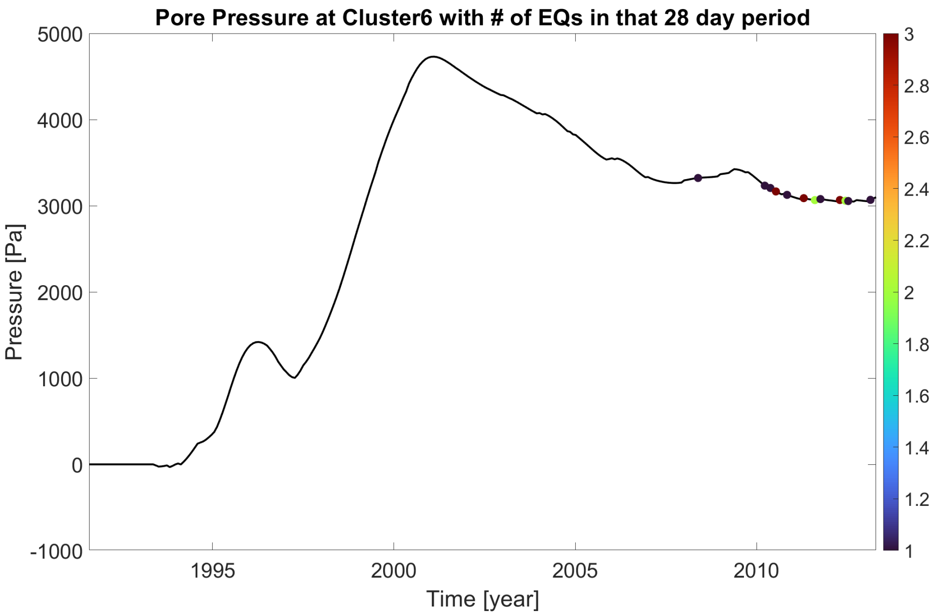

Figure 10. Cluster 6.

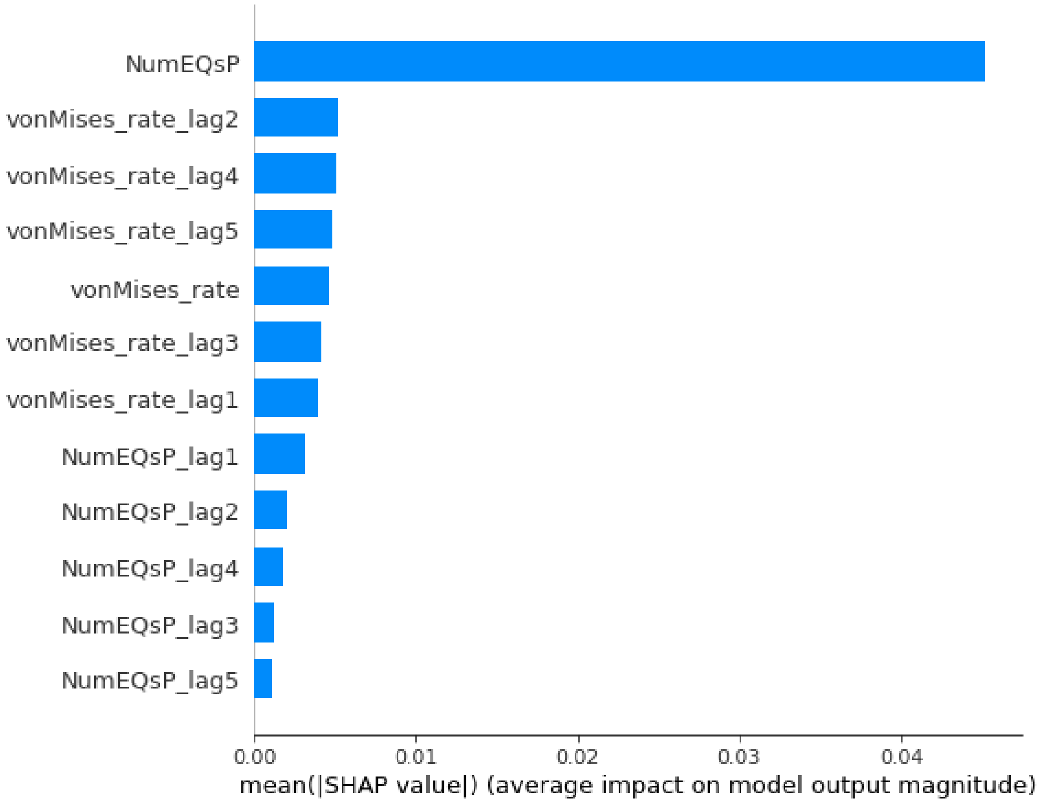

Figure 11. Similar to SM Figure 15 but for the model that includes both the von Mises stress and the von Mises stress rate. This represents 2927 total events. The most important feature is the number of perturbable earthquakes (NumEQsP) that occurred during that same time step as the earthquake in question. The next 65 variables are a mix of the von Mises and von Mises rate.

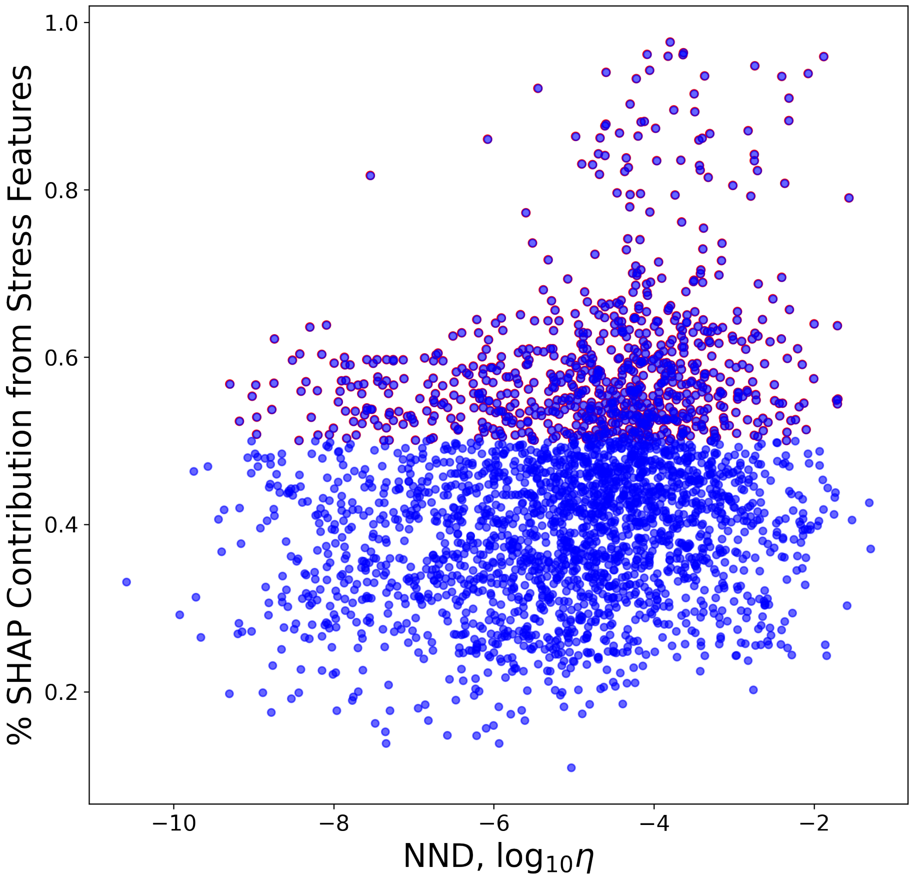

Figure 12. Similar to Figure 3c but for the model that includes both the von Mises stress and the von Mises stress rate. There is more earthquakes associated with the clustered mode, but still a large amount of background mode earthquakes.

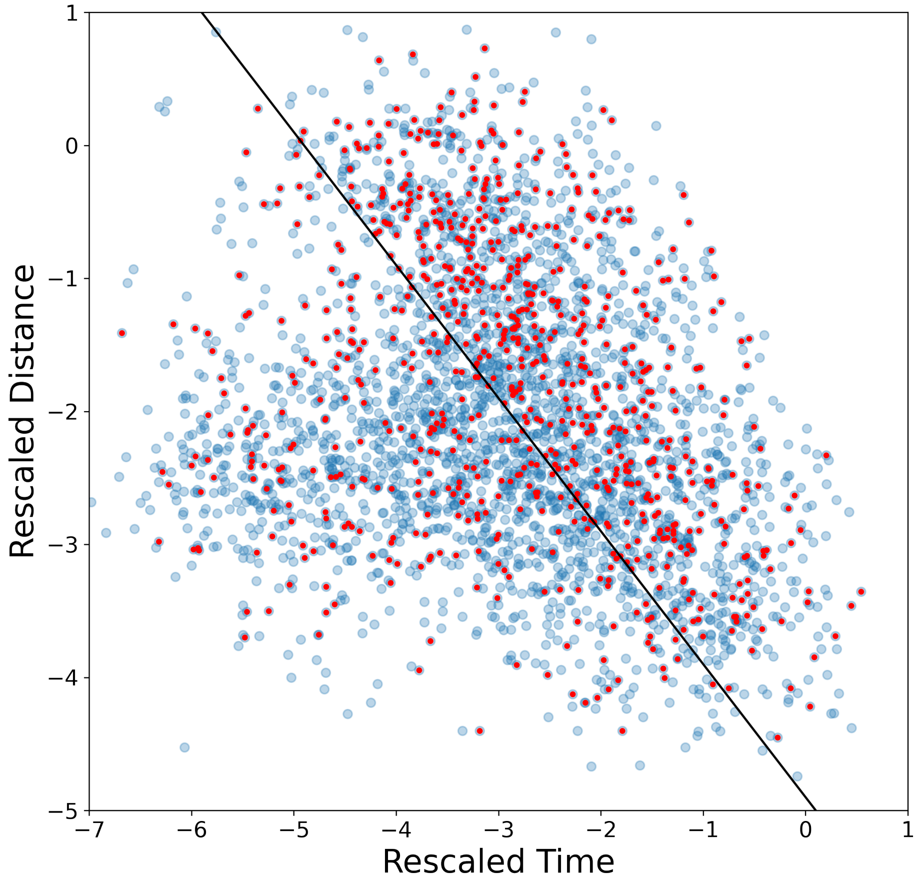

Figure 13. Similar to Figure 3b but for the model that includes both the von Mises stress and the von Mises stress rate. There is more earthquakes associated with the clustered mode, but still a large amount of background mode earthquakes.

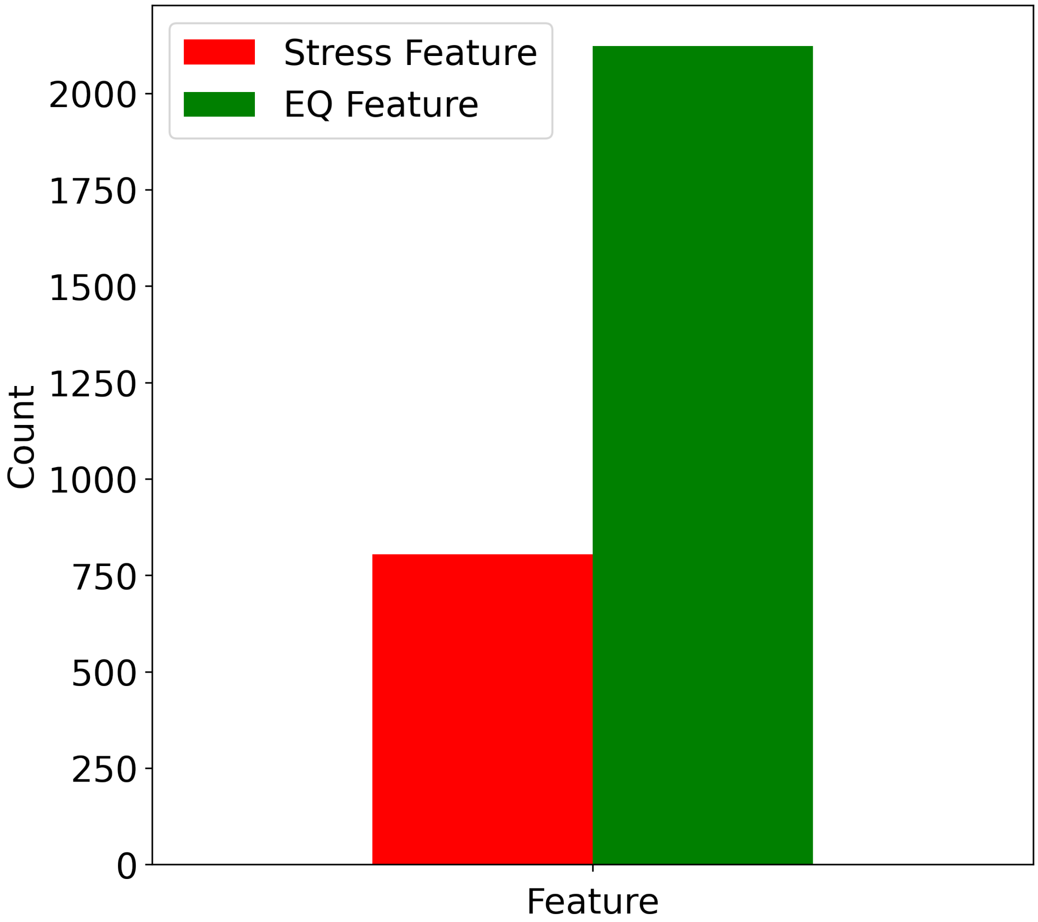

Figure 14. Similar to Figure 4e but for the model that includes both the von Mises stress and the von Mises stress rate. Ratio of the earthquake stress contribution totals for both the stress features and the earthquake features. For our model of including +5lags the stress feature to earthquake feature ratio approximately 1:3 which is must higher than the (1:5) ratio seen in the model that only has one stress feature.

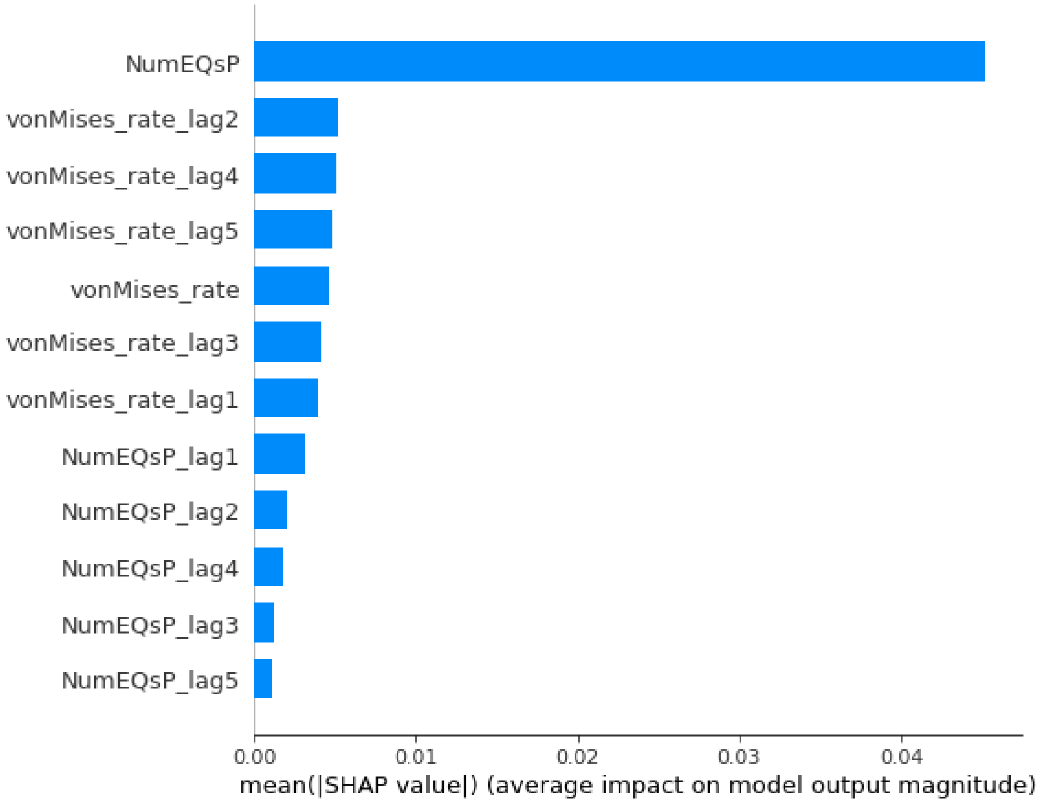

Figure 15. Mean absolute SHAP value for times in the model that an earthquake actually occured. This represents 2927 total events. The most important feature is the number of perturbable earthquakes (NumEQsP) that occurred during that same time step as the earthquake in question. The next 6 variables are all the stress rate from the stress change from the injection.

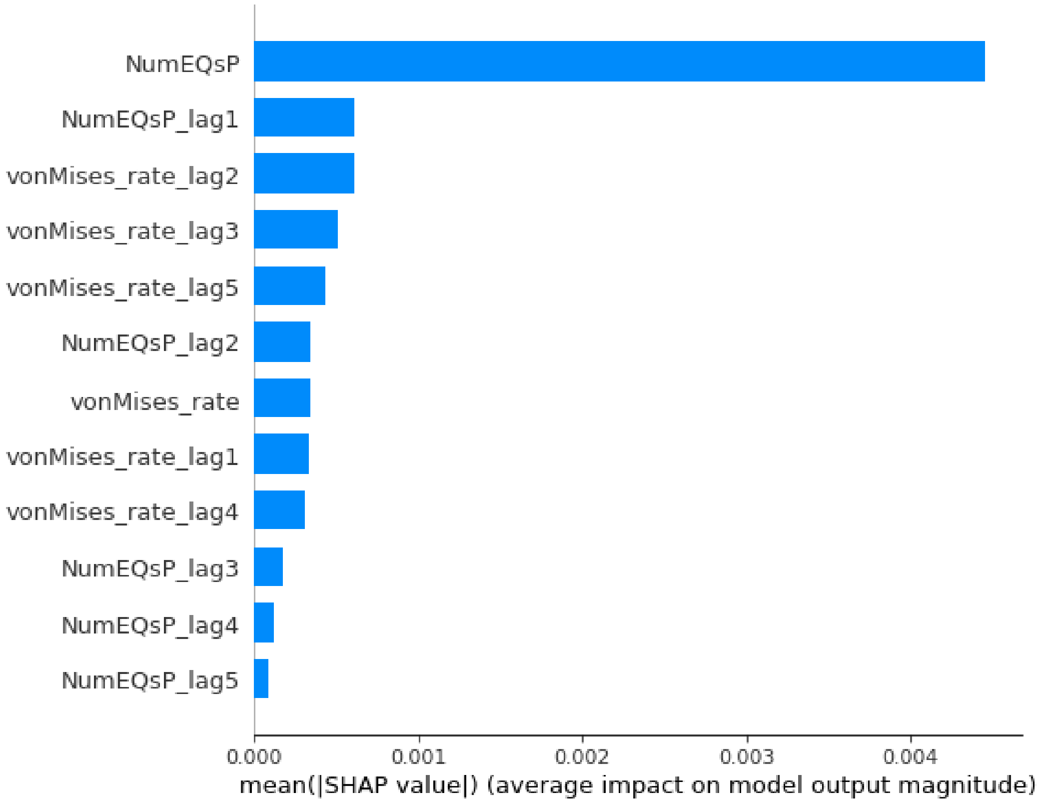

Figure 16. Simlar to SM Figure 15 except for all time steps in the model which includes the time steps when an earthquake is not occurring ($2927 * 284 = 831,268$ total samples).

Figure 17. Similar to SM Figure 14 but for the model that includes both the von Mises stress and the von Mises stress rate and only +3 lags. The ratio is (0.3762) compared with the ratio at +5 lags (0.3789). Implying, that the ratio is not sensitive to increasing lags after +3.

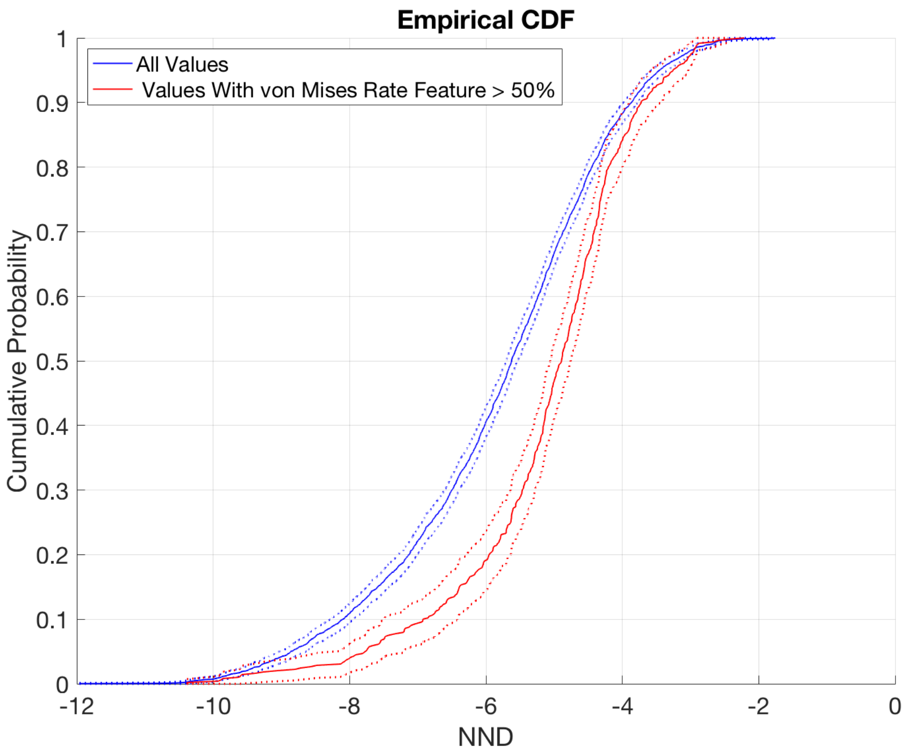

Figure 18. Empirical cumulative density functions of the two sample Kolmogorov–Smirnov test. We show that the distribution for the earthquakes with stress contribution >50% are not drawn from the same distribution as the total earthquakes with 99% confidence. Dashed line represents lower and upper confidence bounds for each distribution.

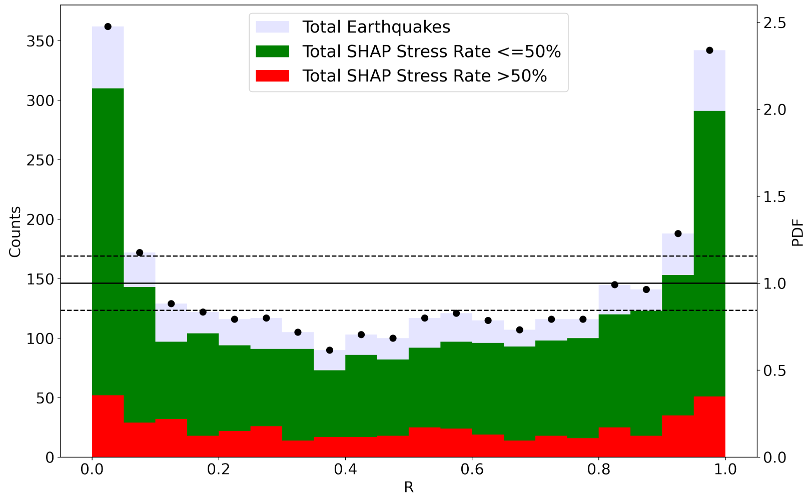

Figure 19. Results of interevent time measure R-test (Van Der Elst & Brodsky, 2010; Davidsen et al., 2017). The histograms represent count of earthquakes for the total earthquakes (blue) and the portion of this set for the the earthquake-driven earthquakes (green) and injection-driven earthquakes (red). The overall events reject the null-hypothesis due to the PDF of the interevent time ratio R exisiting outside the the dotted lines corresponding to the 95% confidence intervals of a Poisson process. Notice that the bimodal tails near $R = 0$ and $R = 1$ are indicative of clustering. The majority of the these tails are composed of earthquake-driven events. The injection-driven earthquakes are considerably flatter and represent a lower portion of the clustered seismicty in the overall catalog.

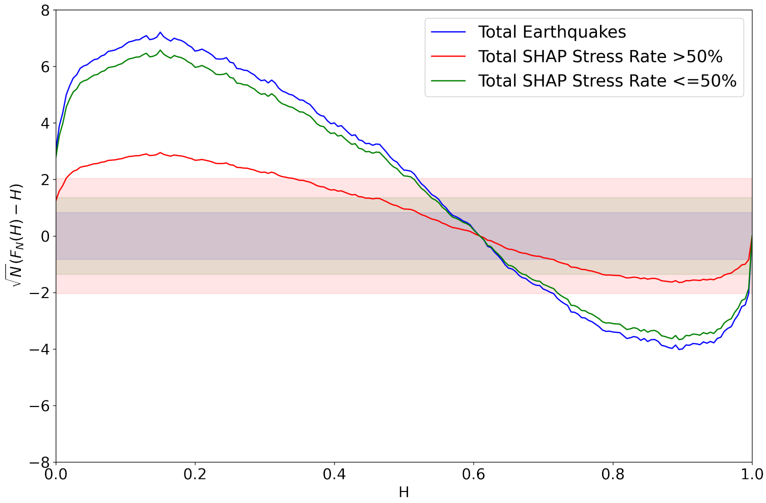

Figure 20. Results of the two sample Kolmogorov-Smirnov test for the distribution of the H statistics obtained by the Bi-test (Bi et al., 1989; Baró et al., 2014; Davidsen et al., 2021). The overall sesimicity (blue) and the portion of cumulative components of the earthquake-driven earthquakes (green) and injection-driven earthquakes (red). The three color bars represent the 50%, 95%, and 99.95% confidence bounds for the null hypothesis of a Poisson process ($F_n(H) = H$). Notice that the portion H attributed to injection-driven earthquakes are significantly flatter compared to the clustered earthquake-driven earthquakes which implies a smaller component of the clustered seismicity albeit we can not reject that it is clustered.

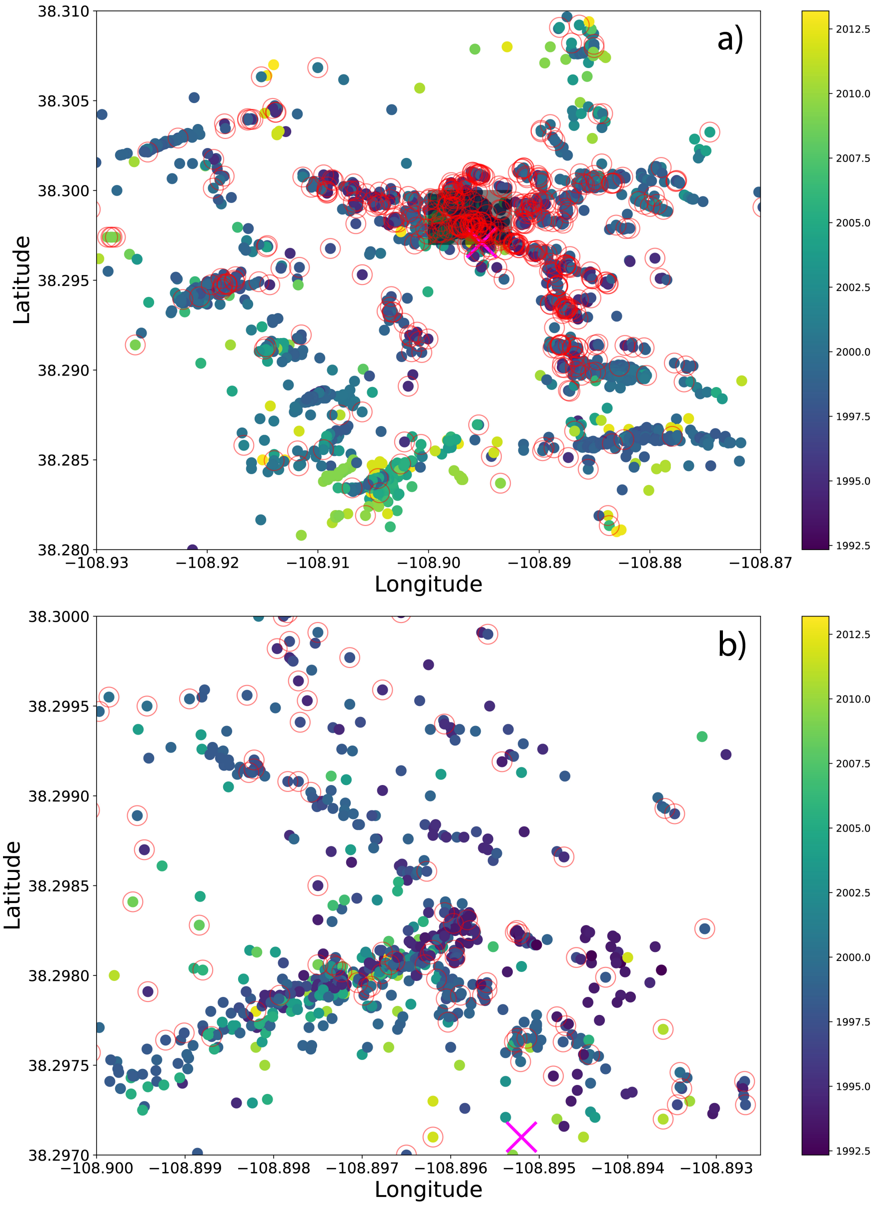

Figure 21. a) Map view of most earthquakes used in our study and denoted in color by the time they occurred. The red circled events represent those circled in red in Figure 3 (i.e. earthquakes that had >50% stress feature contribution). b) same as above panel, but zoomed in near well. The earthquakes strongly stress driven near the injection well, but also appear at different clusters throughout the domain. Often those away from the well have early times compared to the other earthquakes in their cluster suggesting they may be starting the seismicity in those areas. There are some examples of earthquakes that are close but nearly stress driven as opposed to earthquake driven as well.

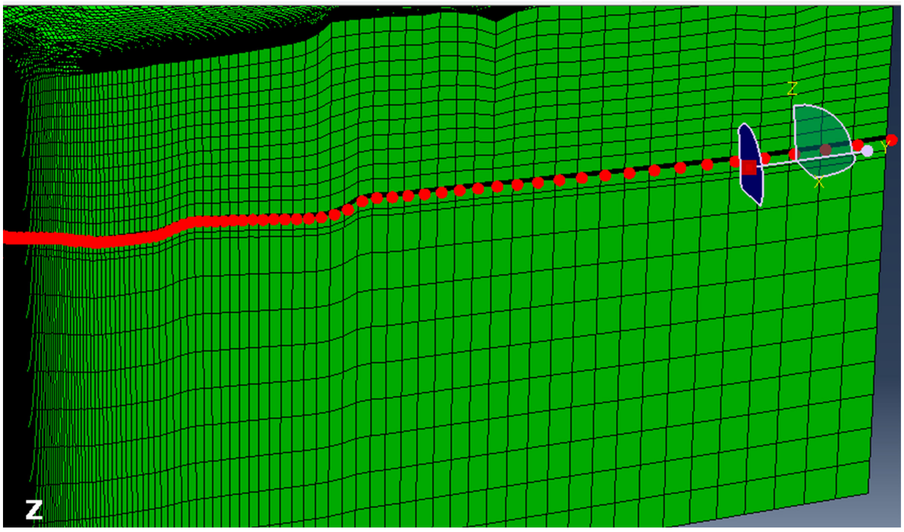

Figure 22. Nodes used in comparison with analytical solution. Well is located on the left and extends to the far field on the right.

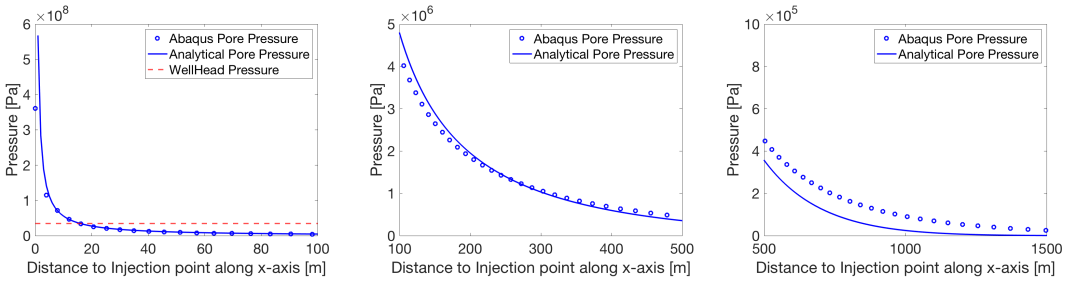

Figure 23. Analytical solution compared to the homogeneous 3D model. Dashed red line represents the average well head pressure of the observed PVU.

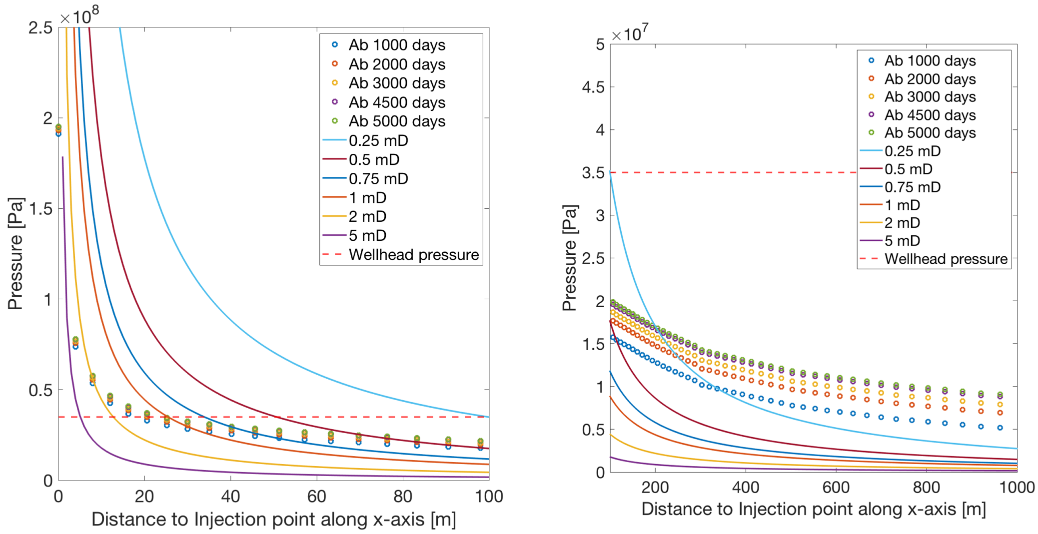

Figure 24. Final 1000 k-medoids model compared to several analytical solutions for a variety of constant rate injection times.

Deciphering earthquake triggering mechanisms for induced seismicity using a fully coupled poroelastic model and machine learning analysis

R. G. Hill[1,2], D. Trugman[3], and M. Weingarten[1]

[1]Department of Geological Sciences, San Diego State University, San Diego, California
[2]Scripps Institution of Oceanography, University of California San Diego, La Jolla, California
[3]Nevada Seismological Laboratory, University of Nevada, Reno, Nevada

Key Points:

- Combining physics-based and machine learning models can decipher earthquake triggering mechanisms for induced seismicity.
- Injection-driven earthquakes account for just 22±5% of all earthquakes in the Paradox Valley catalog.
- Injection-driven earthquakes have a larger b-value, are closer to the well, and occur earlier in the injection history.

Corresponding author: Ryley G. Hill, `ryleyghill@gmail.com`

Abstract

In areas of induced seismicity, earthquakes can be triggered by stress changes from fluid injection and from static deformation caused by fault slip. Here we present a method to distinguish between injection-driven and earthquake-driven triggering of induced seismicity by combining a calibrated, fully-coupled, poroelastic stress model of wastewater injection with a random forest machine learning algorithm trained on both earthquake catalog and modeled stress features. We investigate the classic Paradox Valley, Colorado induced seismicity dataset as an ideal test case: a single, high-pressure injector that has induced >7000 earthquakes between 1991 and 2012. We find that injection-driven earthquakes are approximately 22±5% of the total catalog and have distinct spatiotemporal clustering with a larger b-value, closer proximity to the well and earlier occurrence in the injection history. Our model may be applicable to other regions to help determine site's susceptibility to triggered earthquakes due to fluid injection.

Plain Language Summary

The Paradox Valley Unit, Colorado in the central United States has had a remarkable increase in seismicity coincident with over 8 million cubic meters of brine fluid injection since 1991, inducing >7000 earthquakes within an aquifer 4.5 km below the surface. We use a physics-based model of the Earth combined with statistical and machine learning techniques to help discern which earthquakes are triggered by other earthquakes and which earthquakes are directly triggered by the stress changes from the well as well as their comparative characteristics. Discerning which earthquakes are directly caused from pressure changes due to the fluid injected by the well can inform our understanding of earthquake physics and provide useful information to operators of energy production sites.

1 Introduction

A variety of anthropogenic industrial activities, including wastewater disposal, can induce seismicity (Ellsworth, 2013; Keranen et al., 2014; Shirzaei et al., 2016). Similar to naturally occurring earthquakes, induced seismicity typically occurs on pre-existing, critically stressed faults (Townend & Zoback, 2000). Generating induced seismicity from the reactivation of faults is attributed to several physical mechanisms: pore pressure diffusion (Keranen & Weingarten, 2018; Weingarten et al., 2015; Langenbruch et al., 2018), poroelastic coupling (Segall & Lu, 2015), and stress changes caused by seismic or aseismic fault slip (Ge & Saar, 2022; Brown & Ge, 2018).

These physical mechanisms for induced seismicity jointly contribute to the triggering potential of each earthquake. Since induced earthquakes can be triggered by small stress changes of order 1-10 kPa (Bachmann et al., 2012; Cacace et al., 2021; Stokes et al., 2023), a large difficulty arises in deciphering which mechanism was responsible for triggering each earthquake. We are particularly interested in discerning which earthquakes were more likely driven by injection-related stress changes and which earthquakes were more likely driven by stress changes from prior earthquakes. Furthermore, site-to-site differences in physical rock properties, reservoir structure, fault geometry, and remnant tectonic stress could contribute to differences in the ratio of injection-driven and earthquake-driven events despite similar injection-related stresses.

Relative stress changes from fluid injection require analytical or numerical models to resolve the spatio-temporal evolution of pore pressure and poroelastic stress. To capture the fully coupled poroelastic stress changes (Biot, 1941; Rice & Cleary, 1976; Wang, 2000) induced from the fluid sources requires detailed knowledge of the hydrogeologic properties of the region. The fault geometry is also critical for resolving fault plane stress tractions that characterize fault stability and the potential for induced seismicity (G. C. P. King et al., 1994; Cocco, 2002; Levandowski et al., 2018). Hence, any attempt at discerning induced earthquakes requires an accurate and comprehensive hydrogeological model, detailed injection well data, precise fault geometries, and high-resolution earthquake catalog.

Here, we investigate which earthquakes are more likely triggered by stress changes from injection and which earthquakes are more likely triggered by earthquake-earthquake interaction. We built a three-dimensional (3D) fully-coupled poroelastic model of Paradox Valley Unit, CO (PVU) to resolve time-dependent pore pressure and stress changes due to brine injection. To inform the contribution of our earthquake triggering mechanisms, we use a random forest regression machine learning analysis trained on more than 20 years of induced earthquakes at Paradox Valley Unit and SHapley Additive exPlanations (SHAP), a game theoretic approach to explain the output of any machine learning model (Lundberg & Lee, 2017). We corroborate our results with an independent, induced seismicity cluster analysis, which demonstrates that the physics-based machine learning method provides novel insight into discerning triggering mechanism not previously captured. This model explores the induced earthquake triggering process for wastewater disposal and could help discern what regions are more or less susceptible to stress changes from anthropogenic sources with applicability to other types of subsurface injection including CO_2 sequestration, enhanced geothermal systems, and hydraulic fracturing.

2 Paradox Valley Unit (PVU) Data

The PVU is a program run by the U.S. Bureau of Reclamation, which has been disposing deep brine into a confined aquifer between 4.3 and 4.6 km depth in Paradox Valley, Colorado since 1995 (Ake et al., 2005; Denlinger & RH O'Connell, 2020) (Figure 1). The high-pressure fluid injection has been associated with >7000 earthquakes between 1991 and 2012, which have all been documented as induced seismicity (Ake et al., 2005; Block et al., 2015; V. M. King et al., 2016; Denlinger & RH O'Connell, 2020). Most seismic events within 5 km of the injection well were induced within the first 10 years of injection and nearly all within the high permeability injection reservoir known as the Leadville formation. This zone is highly pressurized from decades of continuous pumping and dictates the lateral migration of seismicity away from the wellbore. These carefully studied events support the notion of a $\sqrt{t}$ diffusion model for pressurization from the well (Block et al., 2015; V. M. King et al., 2016) (Figure 2). Additional ancillary data also make this an ideal study region: numerous wells that extend into deeper formations than just the Leadville aquifer, 3D seismic tomography, logs of P-wave velocity, density and porosity from the near surface to basement in the injection well, and logging of geologic units in other wells in the area (Denlinger & RH O'Connell, 2020).

Most importantly for our purposes, previous work has already compiled a detailed, fully coupled poroelastic model (Denlinger & RH O'Connell, 2020). This model is given by a grid description of nodes with corresponding parameter values which we validate in our finite element numerical model (Dassault Systemes, 2020) with improved meshing near the well where pressure and stress gradients are highest (see SM 8.1). Figure 2 includes a plot of the earthquake distribution overlaid on a cross-section of the numerical model mesh.

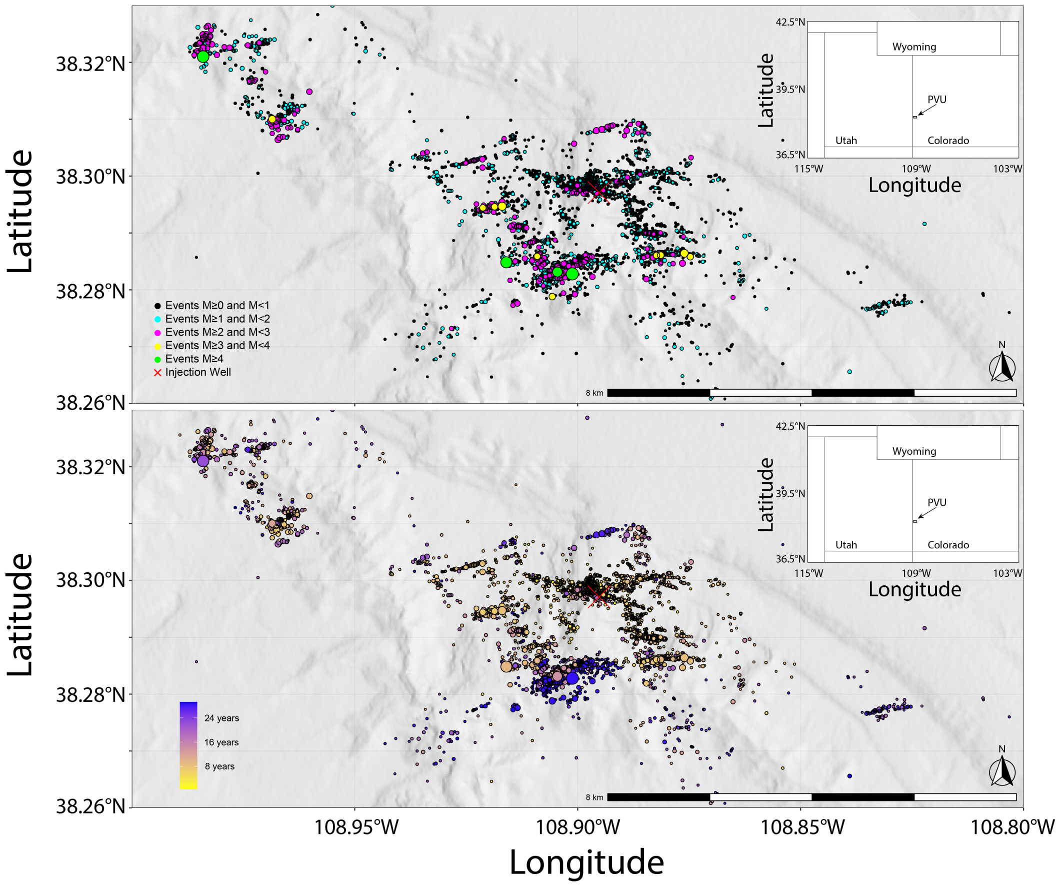

Figure 1. Regional setting of the Paradox Valley Unit, CO (PVU). a) Earthquakes binned by different magnitude ranges. The well is denoted by the red 'X'. The deep brine injection began in 1991 at a depth of 4.3 km. Most seismicity is clustered near the well, where stress perturbations are largest and fluctuate the most. b) Temporal evolution of events. There are more than 7000 earthquakes in the catalog, but within the 8 km radius around the well which we use for analysis includes only 3000.

3 Methods

The core of our methodology relies on the careful development of machine learning features which will represent the contribution of injection-driven stress changes and earthquake-driven stress change for each event in the PVU catalog. Our injection-driven stress feature is resolved using time-dependent pore pressure and stress changes throughout the PVU. Pore pressure and stress perturbations are used to produce von Mises stress features that are physical inputs for the ML/SHAP analysis. To quantify our earthquake-driven stress changes, we create a second feature in the ML/SHAP analysis, which we

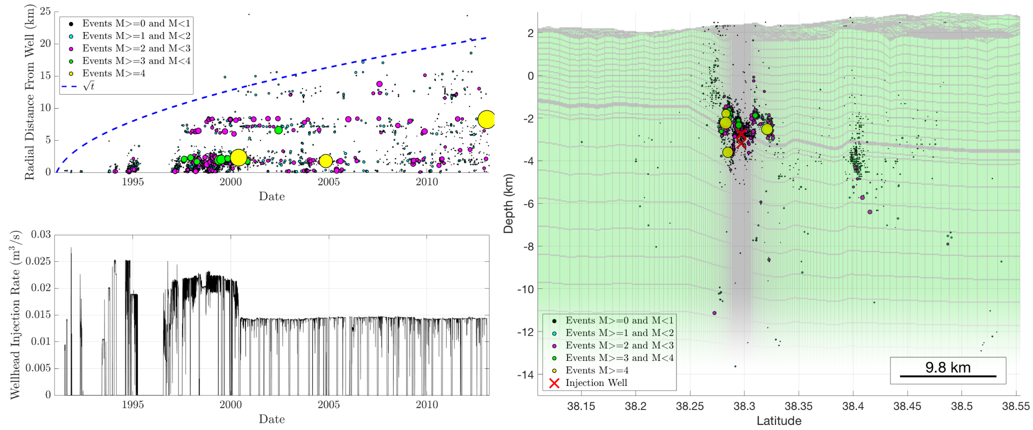

Figure 2. Earthquakes plotted as their radial distance from the well and time. Most earthquakes behave in a typical $\sqrt{t}$ diffusion rate away from the well consistent with progressive lateral migration of seismicity through the permeable Leadville (Ake et al., 2005; Block et al., 2015; Denlinger & RH O'Connell, 2020). Flow tests were performed prior to 1995. Notice injection is highest during peak injection rates ∼1997. Our model records pore pressure and stress perturbations from 10-July-1991 to 16-April-2013. Numerical model cross section with earthquake and well depth superimposed. The model is a fully-coupled poroelastic model based on prior work (Denlinger & RH O'Connell, 2020). We increase the grid discretization near the well to capture large changes in pressure gradients (see SM 8.1).

call the "earthquake feature". The earthquake feature is calculated from the stresses produced by prior earthquakes that may have generated perturbations large enough to produce the current earthquake. These two feature weights are then trained on the entire PVU catalog to find the optimal weight of each feature for each earthquake in the PVU catalog. SHAP analysis of the ML model's feature weights allow for interpretation of the relative contribution of each feature to each event. We support our interpretations of triggering mechanisms from the ML/SHAP with results from a nearest neighbor distance cluster analysis.

3.1 Numerical Model

We model the relative increase in pore pressure ΔP (scalar) and poroelastic stress ΔS (2nd order tensor) for the PVU using a model with one injection well in the center of the model domain (SM Figure 1). The hydrogeologic structure is based on a nodal distribution of parameters that we reduced down to 1000 unique unit formations and use Abaqus to resolve the linear poroelastic equations (R. G. Hill et al., 2024) (see SM 8.1). The model dimensions are 50 km by 50 km laterally with a 18 km depth. Figure 2 shows a cross-section through the well injection zone. The injection is divided across three perforated zones consistent with prior modeling and uses the entire injection history as 7952 unique daily rates in our model from 10-July-1991 to 16-April-2013 (Denlinger & RH O'Connell, 2020) (Figure 2). We output ΔP and ΔS from these daily steps across the entire domain at 284 ~monthly time steps. We do not include earthquakes in our study that occur outside of the modelled time domain which is restricted by the injection history, although the earthquake catalog does extend until 31-December-2019 (Figure 2).

3.2 Stress Features

The Abaqus outputs of ΔP and ΔS were post-processed in Matlab using abaqus2matlab (Papazafeiropoulos et al., 2017). The stress features of ΔP and ΔS represent the relative change induced from the fluid injection and are resolved at the closest value in the domain to each ~3000 earthquakes during our study time. We assessed a variety of different stress features during the preliminary stages of this work, consistent with prior forecasting studies (DeVries et al., 2018; Sharma et al., 2020; Qin et al., 2022). We found that von Mises stress and von Mises stressing rate were the best stress-based features for forecasting the seismicity rate and are the only two stress features we consider hereinafter. We make the assumption that the von Mises stress is resolved uniformly using a strike azimuth of 260^0 and vertical dip consistent with the most common faulting structure present from the earthquakes locations (Denlinger & RH O'Connell, 2020).

3.3 Earthquake Feature

Static stress transfer modeling can be used to assess earthquake-earthquake triggering on faults embedded in an elastic half space with homogeneous isotropic elastic properties (Lin & Stein, 2004; Toda et al., 2005). Stress transfer can promote or reduce the potential of earthquake triggering, depending on the coefficient of friction, fault geometry, and sense of slip (G. C. P. King et al., 1994; Stein, 1999). Since the exact geometries of every earthquake in our model are unknown, we choose to develop an earthquake feature that is based on the occurrence of prior earthquakes that could have plausibly influenced each earthquake.

We use 'cutde' (Thompson, 2021) to resolve elastic stress transfer produced from triangular dislocation element representations of fault slip (Nikkhoo & Walter, 2015). Several assumptions are required for the static stress transfer modeling: (1) We assume a uniform stress drop for every event of 3 MPa, (2) a shear modulus of 30 GPa, and (3) a Poisson ratio of 0.25. Under this framework we show that the von Mises stress is self-similar for both parallel and perpendicular receiver receiver planes at a given distance from the event (SM Figure 2). By varying event magnitude, we calculate a radius from the center of the dislocation that can increase the potential of failure up to a distance that intersects the 10 kPa triggering threshold (Reasenberg & Simpson, 1992; Stein, 1999). As a sensitivity test we varied the stress drop from 1-10 MPa and observe marginal change to the perturbable radius for varying magnitudes (SM Figure 2). Then, for every earthquake, we create an earthquake-to-earthquake feature, which counts the number of earthquakes that could have perturbed it. The earthquake count is represented by $\ln(N + 1)$, where N is the number of perturbing earthquakes to have occurred prior to each event. Higher values of this feature indicate a higher likelihood of earthquake-earthquake interaction.

3.4 ML/SHAP Analysis

We use the machine learning technique of random forest regression (RFR) to fit our observed seismicity (Ho et al., 1995; Ho, 1998). The RFR model makes a prediction on the target variable, which are one-hot encoded occurrences of the observed earthquakes across 284 ∼monthly time steps each. We avoid overfitting and optimize model hyperparameters using an exhaustive grid search applied to a 5-fold cross-validation score. The observed seismicity is therefore repeatedly divided into training and test folds with the mean squared error evaluating fit on the test folds which the trained model does not see. The RFR models chosen for our analysis were trained using the hyperparameters derived from the best-performing model during the cross-validation process.

The input features are composed from the stress and earthquake features as well as their time lags. The time lags are introduced both to capture any potential anisotropy or hydromechanical heterogeneity that are not explicit in the numerical model as well as time delayed effects that former earthquakes or stress history may have when perturbing the current earthquake. We find that including more lags improves the overall fit of our model, up to ∼50 lags, but is likely over-fitting and unrealistic. We assume that the physical meaning of the lags are unreasonable beyond ∼1 year before the actual earthquake timing and reserve our total lags to the local minimum of 5 lags (SM Figure 3). In other words, a model can contain the current stress/earthquake feature (+0 lag), the time period prior (+1 lag), and the time periods before that (+2-+5 lag etc..) or any combination of that set (SM Figure 3).

To assess feature importance, we use SHAP, which provides a robust and self-consistent means to explain the predictions of our target variable (earthquake or no-earthquake) by computing the contribution of each feature to the prediction (Shapley et al., 1953; Lundberg & Lee, 2017). A key advantage of SHAP lies in its ability to consistently untangle the impacts of multiple correlated input variables (Trugman & Ben-Zion, 2023). Since the SHAP value is represented as an additive feature, it is a linear model and the contributions of each feature can be added to describe the contribution that the stress features have compared to the earthquake features. This is often preferable compared to permutation feature importance which chooses importance based on the decrease in model performance. Larger SHAP values for a given feature, averaged across the dataset, signify a higher importance for the model's prediction.

3.5 Cluster Analysis

As an independent test of earthquake behavior, we investigate how the PVU seismicity is distributed in magnitude, space, and time using a traditional cluster analysis. We use the nearest neighbor distance (NND) in the space-time-magnitude domain (Baiesi & Paczuski, 2004) for each pair of events i and j using the following equation:

$$\eta_{ij} = \begin{cases} t_{ij}(r_{ij})^d 10^{-bm_i}, & t_{ij} > 0; \\ \infty, & t_{ij} \leq 0 \end{cases} \tag{1}$$

Where, t_{ij} is the interevent time (year), r_{ij} is the inter event distance (km), d is the dimension of the earthquake hypocenter distribution ($d = 1.32$) determined using a box-counting procedure (Corral, 2003) (SM Figure 4), b is the b-value ($b = 0.75$) determined by maximum likelihood estimation (Aki, 1965), and m_i is the ith event magnitude (Zaliapin & Ben-Zion, 2013; Schoenball et al., 2015). The NND is separable into rescaled distance (R_{ij}) and rescaled time (T_{ij}) where (Zaliapin et al., 2008; Zaliapin & Ben-Zion, 2013):

$$\eta_{ij} = R_{ij} T_{ij} \tag{2}$$

$$R_{ij} = (r_{ij})^d 10^{-bm_i/2} \tag{3}$$

$$T_{ij} = (r_{ij})^d 10^{-bm_i/2}, \tag{4}$$

An advantage of this form of NND is that the clustering style of seismicity can be displayed by a joint 2D distribution of rescaled time $\log_{10} T_{ij}$ and rescaled distance $\log_{10} R_{ij}$ (Zaliapin et al., 2008; Zaliapin & Ben-Zion, 2013, 2016). The distribution helps to describe the type of earthquake clustering style, since observed seismicity often shows a bimodal joint distribution divided by a constant line and chosen nearest-neighbor threshold n_0. Events below this threshold are classified as clustered (i.e., earthquake-driven triggering) and the events that are above this threshold are classified as background (i.e., injection-driven or independent) (Zaliapin & Ben-Zion, 2016). We use the NND distributions for the PVU as an independent test of the physical mechanism driving each earthquake in the sequence. We hypothesize that our ML/SHAP model will preferentially separate injection-driven vs earthquake-driven events as identified by Zaliapin and Ben-Zion (2016).

4 Results

4.1 Numerical Model Results

The fully-coupled poroelastic model shows that areas with seismicity experience pore pressure increases from 0.005 MPa to 9 MPa. Most pore pressure increases occur within an 8 km radius around the injection well (SM Figures 5-10). Most seismicity occurs in close vicinity of the injection well and the ΔP is highest in early 1999 ($\sim$9 MPa). The pressure changes near the well mimic injection rate changes as the temporal delay of diffusion is negligible. Elsewhere, the diffusion process dominates the pressure changes and therefore the increase in pore pressure is more gradual through time (SM Figure 8-9). Across the domain, seismicity occurs during the highest rates of pressure increase. This observation is consistent with other instances of wastewater induced seismicity (Langenbruch et al., 2018; Qin et al., 2022). The increasing pore pressure diffuses laterally through the highly permeable Leadville formation. Low permeability confining units above and below the reservoir restrict vertical pressure migration (SM Video 1).

4.2 Cluster Analysis Results

Results of the NND cluster analysis show that a larger portion of the earthquakes are classified as the background mode (Zaliapin & Ben-Zion, 2016; Goebel et al., 2019)(Figure 3a). The constant threshold value $\eta_0 = -4.9$ is chosen based on a 1D Gaussian mixture model analysis (Zaliapin et al., 2008; Zaliapin & Ben-Zion, 2016). The clustering behavior is similar to other cases of wastewater induced seismicity (Zaliapin & Ben-Zion, 2016; Glasgow et al., 2021). There is a larger population of background events and clustered events occur at short space-time distances. These results are also dissimilar from other cases of induced seismicity that have a more clear bimodal distribution, albeit different mechanical processes are occurring (Zaliapin & Ben-Zion, 2016, e.g., Coso and Salton Sea geothermal areas). A small portion of the background domain is characterized by low R_{ij} and large T_{ij}, which often characterizes these events as repeaters (Zaliapin & Ben-Zion, 2016; Hsu et al., 2024). These events make sense in the context of single well injection. The start-stop nature of the injection means repetitive changes in stress occur at the same locations. This is observed in the pore pressure results at different clusters near the well where the pore pressure closely follows the flux of the injection (SM Figures 5-8).

4.3 ML/SHAP Model Results

Our preferred model uses the following: 1000 total trees, a maximum depth of 10, a minimum sample split of 10, and a minimum of 4 samples for a leaf node. Figure 4a shows the fit of our random forest model for two different model types. One model uses only the von Mises stress rate and earthquake feature while the other model uses both the von Mises stress and the von Mises stress rate as well as the earthquake feature (including lags). We find that the mean squared error (MSE) is slightly lower for the model that includes both stress features. However, we choose to present the parsimonious solution of one stress feature and refer the reader to the supplementary for the results including both stress features, which contains small differences to the main results (SM Figures 11-14).

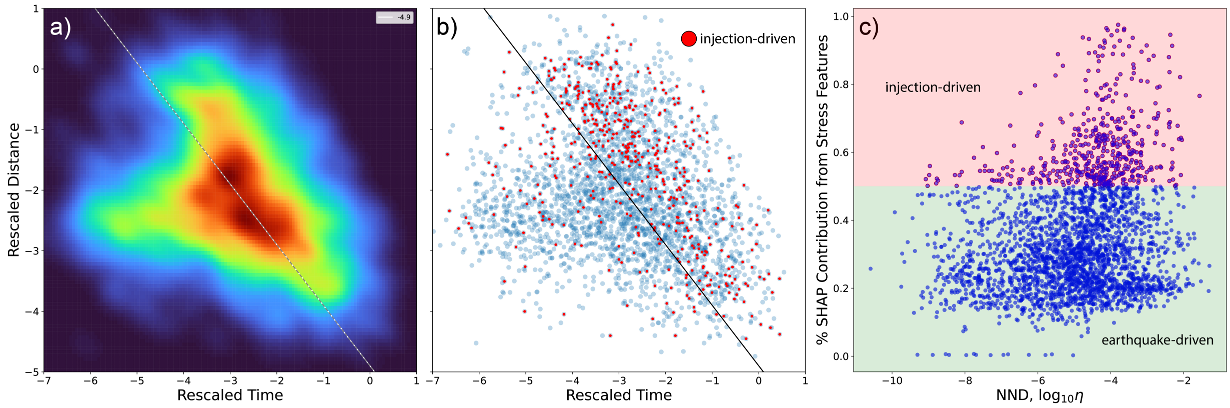

Figure 3. a) Nearest neighbor time-distance distributions for seismicity in the PVU. The color bar represents the number of event pairs. The total number of earthquakes used in this analysis is 2927. The diagonal dashed line is the η_0 background (above) and clustered (below) mode threshold. The value is a constant distance threshold determined by the 1D Gaussian mixture model and is -4.9. b) Comparing the earthquakes that have at least 50% stress feature contribution on the rescaled distance rescaled time plot. Many of the earthquakes cluster in the independent background mode with a second distribution towards the repeater mode and a few earthquakes spread out in the cluster mode. c) The SHAP stress feature contribution vs. the nearest neighbor distance value. Many of the earthquakes cluster below the 50% stress feature contribution indicating and to the left of the -4.9 cluster threshold. However, earthquakes that have >50% stress feature contribution, denoted as red circles, tends to populate the 'background' mode of the NND (to the right of -4.9). These results are consistent for earthquakes driven by stress from the injection since they act as initial parent earthquakes that trigger subsequent seismicity in a region that has experienced stress changes high enough to begin seismicity.

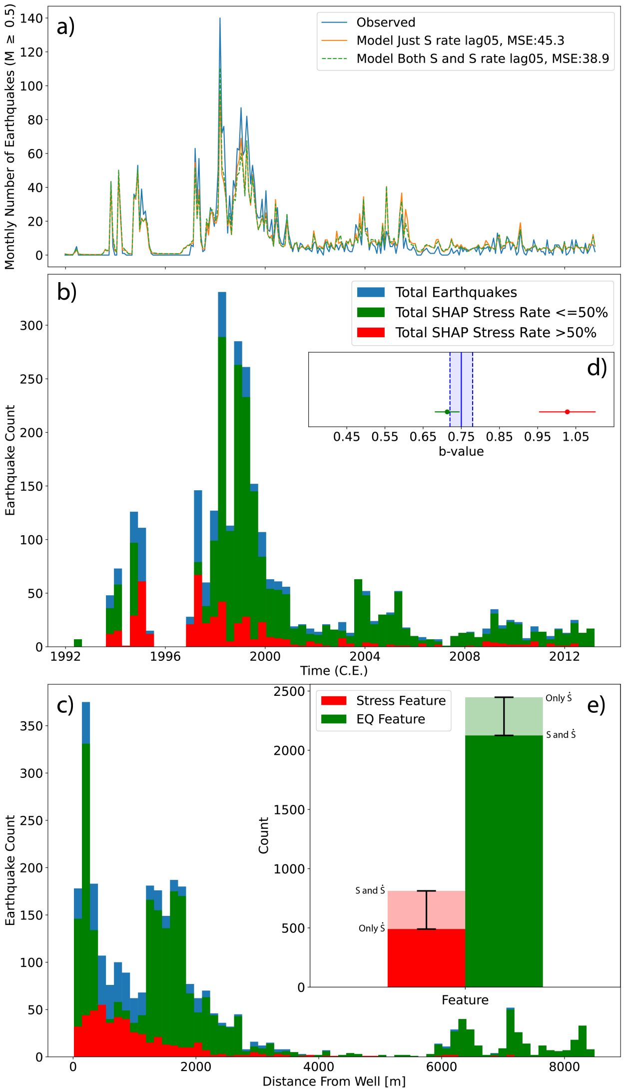

Figure 4. a) Forecasted seismicity rate across for all time steps. Orange line represents the best fit model that includes only the von-Mises stress rate. The dashed green line includes von-Mises stress and has slightly better fit. b) Earthquake count binned through time for earthquakes with SHAP stress rate <=50% (ie. earthquake-driven green) and >50% (ie. injection-driven red). c) same as panel b, but for distance away from well. d) b-value analysis of all earthquakes (blue), earthquake-driven (green), and injection-driven (red). e) Ratio of all earthquakes with a larger sum of SHAP value for stress features (red) and the earthquake features (green). We reflect the uncertainty of triggering mechanism based on our two models described in panel a.

The SHAP analysis results are summarized in SM Figure 15. We output the results exclusively at the time when the earthquakes occur since we are only interested in discerning the contribution of the stress features at that time. A summary of the SHAP contributions for all time, not just when the earthquakes occur, is presented in the supplementary material (SM Figure 16). The feature with the higher overall impact on the model is the perturbable earthquake feature that represents the number of earthquakes that occurred during the chosen time step that could have potentially perturbed the earthquake in question. The next most important features, with nearly equal importance, are the lagged von Mises stress rates. These stress features are considerably less important on average compared with the earthquake feature.

To assess the total contribution of the stress features vs the earthquake features, we compare the cumulative feature results. Separating which earthquakes are dominated by cumulative feature importance, Figure 4e shows that the ratio of earthquakes that have a higher stress feature contribution compared to earthquakes that have a higher total earthquake feature contribution is about 1:5. We examined the sensitivity of this since it would be expected that increasing lags may contribute to higher contribution to stress. While the stress contribution does increase for models that include 0,+1,+2 lags, after the model reaches +3 lags, earthquakes that are considered to have a higher total stress contribution increase marginally. For example, from +3 lags to +5 lags the ratio has a percent increase of only $\sim$0.5% (SM Figure 17). We do not pursue sensitivity past +5 lags as the SHAP analysis is computationally expensive with increasing features. It is important to note that when testing increasing lag sensitivity, the overall ratio of the total number of stress features to earthquake features remains the same.

5 Discussion

The ML/SHAP model identifies injection-driven earthquakes (ie. >50% stress feature contribution) predominantly as background events in the NND model (Figure 3b-c). In the NND model, background events are mostly the independent Poisson mode (Zaliapin et al., 2008; Zaliapin & Ben-Zion, 2016). This suggests injection-driven earthquakes often act as parent earthquakes, likely induced by pore pressure and stress changes, triggering further seismicity. These results are further supported by the relative timing of these earthquakes, which often occur at the beginning of injection stages (Figure 4b). We statistically compare injection-driven event distribution to the larger catalog using a two-sample Kolmogorov–Smirnov test, which rejects the null hypothesis of identical distributions with 99% confidence (SM Figure 18).

We explored two interevent time measures to analyze event timing between injection-driven and earthquake-driven classes (Davidsen et al., 2021). The first measure, interevent time ratio R, indicates deviations from a Poisson process (Van Der Elst & Brodsky, 2010; Davidsen et al., 2017). Rejecting the Poisson process hypothesis with >95% confidence, we observe a significant peak at $R = 0$ suggesting triggering, and another at $R = 1$ indicating longer intervals likely due to stress changes stimulated by a non-random process (SM Figure 19). Injection-driven earthquakes show less bi-modal distribution, implying less temporal clustering than earthquake-driven ones. The second measure, the Bi-test, also indicates temporal clustering and rejects the Poisson process hypothesis with >95% confidence (Bi et al., 1989; Baró et al., 2014). Injection-driven earthquakes exhibit lower temporal clustering (lower fluctuation in H values) compared to clearly clustered earthquake-driven ones (higher fluctuation in H values around 0 and 1) (SM Figure 20).

We also analyze the spatiotemporal distribution of injection-driven earthquakes (Figure 4b-c). They tend to occur earlier in injection history and cluster near the injection well, contrasting with earthquake-driven earthquakes. These events coincide with sharp stress field changes near the well, often preceding clustered seismicity. The b-value of injection-driven earthquakes (Figure 4d) is notably higher (1.03) compared to overall seismicity (0.75) and earthquake-driven events (0.71). This suggests that injection-driven events tend to have lower magnitudes, on average, than the earthquake-driven events and a b-value closer to 1 indicates that these events may appear to mimic independent background events. The finding that earthquake-driven events produce lower b-values and characterize more of the large events in induced catalogs may have implications for maximum magnitude estimates of induced earthquakes, since initial injection-driven earthquakes at the onset of induced sequences might underestimate the overall maximum magnitude of triggered seismicity

Clusters of seismic activity away from the well are noticeable, yet they have fewer stress-dominated earthquakes (SM Figure 21). Often, clusters away from the well are initiated by a few injection-driven earthquakes. This observation is consistent with the machine learning process since earthquakes that had no prior earthquakes would not be expected to have a strong prior earthquake feature contribution. However, not all injection-driven earthquakes precede nearby seismic events. Additionally, areas lacking clear clustering seem to host multiple injection-driven earthquakes, suggesting varied driving mechanisms in those regions (SM Figure 21).

It is important to recognize that uncertainty is introduced in the model at various stages: physical model material parameters, static stress transfer parameters, RFR input features, and the number of included lags. We affirm the numerical model (see SM 8.1 and SM Figures 5-10) and show that the static stress transfer at a triggering threshold of 10 kPa is only marginally sensitive to varied stress drop assumptions (SM Figure 2). We find that increasing lags beyond +3 does not greatly change the ratio of injection-driven and earthquake-driven earthquakes (SM Figure 17). The main model sensitivity lies in input features: incorporating von Mises stress and rate increases injection-driven earthquakes from 17% to 27% (Figure 4e and SM Figure 14). It is unclear whether including both the stress and stress rate features provides a better model since more injection-driven earthquakes also begin to populate the cluster mode, which we assume is a product of over-fitting the seismicity rate (Figure 4a and SM Figure 13). We therefore suggest that these two models may provide estimates on the lower and upper bound with the true portion of injection-driven earthquakes at approximately 22±5% of the total.

Results of this study indicate that the physics-based model, with RFR and SHAP analysis, accounts for a significant portion of independent background mode events found in NND cluster analysis. However, not all background mode events are classified as injection-driven. The absence of a clear bi-modal distribution in NND analysis suggests that events populating the independent background mode may have less direct fluid injection influence (Zaliapin & Ben-Zion, 2016; Glasgow et al., 2021). We expect this ratio of injection-driven vs earthquake-driven seismicity to vary by geologic region, stress state, distribution of preexisting faults, and injection style. Understanding this ratio is crucial for wastewater management, as it impacts induced seismic hazard. Sites where seismicity is mainly earthquake-driven would be harder to control via well operations best practices (R. G. Hill et al., 2024), while sites with mostly injection-driven events may be more manageable. Identifying the triggering process in candidate sites can guide energy production decisions, avoiding areas prone to severe triggered seismicity.

6 Conclusion

We decipher induced earthquake triggering mechanisms using a 3D fully-coupled poroelastic model of brine injection and a random forest machine learning model trained on more than 20 years of induced earthquakes at Paradox Valley Unit, Colorado. Our simple ML/SHAP feature training approach, using one injection-driven feature and one earthquake-driven feature, allows for the separation of events that are more likely injection-driven from events that are more likely earthquake-driven in the sequence. Comparing the ML/SHAP results with a nearest-neighbor cluster analysis reveals good agreement in stress contribution and cluster style. Our methodology finds that injection-driven earthquakes make up only 22±5% of the catalog and have distinct spatiotemporal clustering with a larger b-value, closer proximity to the well and earlier occurrence in the injection history. Our method may be applicable to other regions to help determine the site susceptibility to earthquake triggering or aid in declustering induced catalogs.

7 Open Research

Data of Abaqus files, post-processing scripts, ML model scripts, and figure generation scripts are available online at Hill, R. (2024) (`https://doi.org/10.5281/zenodo.10967359`).

The wastewater injection data and earthquake data is available from the Bureau of Reclamation Upper Colorado Basin website (`https://https://www.usbr.gov/uc/progact/paradox/index.html`).

The numerical models were built and solved using the software Abaqus (Dassault Systemes, 2020).

Acknowledgments

The authors appreciate discussion with Robert Guyer at early stages of the work. We acknowledge use of the CSRC high-performance computing cluster and other support from San Diego State University. D.T.T acknowledges support from NSF Award EAR-2121666.

References

Ake, J., Mahrer, K., O'Connell, D., & Block, L. (2005). Deep-injection and closely monitored induced seismicity at paradox valley, colorado. *Bulletin of the Seismological Society of America*, *95*(2), 664–683.

Aki, K. (1965). Maximum likelihood estimate of b in the formula log n= a-bm and its confidence limits. *Bull. Earthquake Res. Inst., Tokyo Univ.*, *43*, 237–239.

Bachmann, C. E., Wiemer, S., Goertz-Allmann, B., & Woessner, J. (2012). Influence of pore-pressure on the event-size distribution of induced earthquakes. *Geophysical Research Letters*, *39*(9).

Baiesi, M., & Paczuski, M. (2004). Scale-free networks of earthquakes and aftershocks. *Physical review E*, *69*(6), 066106.

Baró, J., Martín-Olalla, J.-M., Romero, F. J., Gallardo, M. C., Salje, E. K., Vives, E., & Planes, A. (2014). Avalanche correlations in the martensitic transition of a cu–zn–al shape memory alloy: Analysis of acoustic emission and calorimetry. *Journal of Physics: Condensed Matter*, *26*(12), 125401.

Bear, J. (1988). *Dynamics of fluids in porous media.* Courier Corporation.

Bi, H., Börner, G., & Chu, Y. (1989). Correlations in the absorption lines of the quasar q0420-388. *Astronomy and Astrophysics (ISSN 0004-6361), vol. 218, no. 1-2, July 1989, p. 19-23.*, *218*, 19–23.

Biot, M. A. (1941). General theory of three-dimensional consolidation. *J. Appl. Phys.*, *12*(2), 155–164. Retrieved 2021-04-13, from `https://urldefense.com/v3/__http://aip.scitation.org/doi/10.1063/1.1712886__;!!Mih3wA!E0xCUAx3ctL8wKS_tp-pNn95UaeXh_lRKy7b2Mcg4-S1_-Ss2N0b2nM5ld42UzHIa8rqXMpIajp0q38i$` doi: 10.1063/1.1712886

Block, L. V., Wood, C. K., Yeck, W. L., & King, V. M. (2015). Induced seismicity constraints on subsurface geological structure, paradox valley, colorado. *Geophysical Journal International*, *200*(2), 1172–1195.

Brown, M. R., & Ge, S. (2018). Small earthquakes matter in injection-induced seismicity. *Geophysical Research Letters*, *45*(11), 5445–5453.

Cacace, M., Hofmann, H., & Shapiro, S. A. (2021). Projecting seismicity induced by complex alterations of underground stresses with applications to geothermal systems. *Scientific Reports*, *11*(1), 23560.

Cocco, M. (2002). Pore pressure and poroelasticity effects in coulomb stress analysis of earthquake interactions. *J. Geophys. Res.*, *107*, 2030.

Corral, A. (2003). Local distributions and rate fluctuations in a unified scaling law for earthquakes. *Physical Review E*, *68*(3), 035102.

Dassault Systemes, . (2020). *Abaqus (version 2019).* Retrieved from `https://urldefense.com/v3/__https://www.3ds.com/products-services/simulia/products/abaqus/__;!!Mih3wA!E0xCUAx3ctL8wKS_tp-pNn95UaeXh_lRKy7b2Mcg4-S1_-Ss2N0b2nM5ld42UzHIa8rqXMpIag2Io7P8$`

Davidsen, J., Goebel, T., Kwiatek, G., Stanchits, S., Baró, J., & Dresen, G. (2021). What controls the presence and characteristics of aftershocks in rock fracture in the lab? *Journal of Geophysical Research: Solid Earth*, *126*(10), e2021JB022539.

Davidsen, J., Kwiatek, G., Charalampidou, E.-M., Goebel, T., Stanchits, S., Rück, M., & Dresen, G. (2017). Triggering processes in rock fracture. *Physical review letters*, *119*(6), 068501.

Denlinger, R. P., & RH O'Connell, D. (2020). Evolution of faulting induced by deep fluid injection, paradox valley, colorado. *Bulletin of the Seismological Society of America*, *110*(5), 2308–2327.

DeVries, P. M., Viégas, F., Wattenberg, M., & Meade, B. J. (2018). Deep learning of aftershock patterns following large earthquakes. *Nature*, *560*(7720), 632–634.

Ellsworth, W. L. (2013). Injection-induced earthquakes. *Science*, *341*(6142).

Ge, S., & Saar, M. O. (2022). Induced seismicity during geoenergy development—a hydromechanical perspective. *Journal of Geophysical Research: Solid Earth*, *127*(3), e2021JB023141.

Glasgow, M., Schmandt, B., Wang, R., Zhang, M., Bilek, S. L., & Kiser, E. (2021). Raton basin induced seismicity is hosted by networks of short basement faults and mimics tectonic earthquake statistics. *Journal of Geophysical Research: Solid Earth*, *126*(11), e2021JB022839.

Goebel, T., Rosson, Z., Brodsky, E., & Walter, J. (2019). Aftershock deficiency of induced earthquake sequences during rapid mitigation efforts in oklahoma. *Earth and Planetary Science Letters*, *522*, 135–143.

Harr, C. (1988). Final geological well report. *US Bureau of Reclamation Test Well*(1).

Hill, R. (2024). *Data and Code for Modeling Paradox Valley Unit [Data Set].* Zenodo. Retrieved from `pending`

Hill, R. G., Weingarten, M., Langenbruch, C., & Fialko, Y. (2024). Mitigation and optimization of induced seismicity using physics-based forecasting. *JGR: Solid Earth (in review)*. (in review)

Ho, T. K. (1998). The random subspace method for constructing decision forests. *IEEE transactions on pattern analysis and machine intelligence*, *20*(8), 832–844.

Ho, T. K., et al. (1995). Proceedings of 3rd international conference on document analysis and recognition. In *Proceedings of 3rd international conference on document analysis and recognition.*

Hsu, Y.-F., Zaliapin, I., & Ben-Zion, Y. (2024). Informative modes of seismicity in nearest-neighbor earthquake proximities. *Journal of Geophysical Research: Solid Earth*, *129*(3), e2023JB027826.

Keranen, K. M., & Weingarten, M. (2018). Induced seismicity. *Annual Review of Earth and Planetary Sciences*, *46*, 149–174.

Keranen, K. M., Weingarten, M., Abers, G. A., Bekins, B. A., & Ge, S. (2014). Sharp increase in central oklahoma seismicity since 2008 induced by massive wastewater injection. *Science*, *345*(6195), 448–451.

King, G. C. P., Stein, R. C., & Lin, J. (1994). Static stress change and the triggering of earthquakes. *Bull. Seism. Soc. Am.*, *84*, 935–953.

King, V., & Block, L. (2019, Aug). *Paradox valley seismic and injection data - amerigeoss community platform datahub. (beta).* Retrieved from `https://urldefense.com/v3/__https://data.amerigeoss.org/dataset/paradox-valley-seismic-and-injection-data__;!!Mih3wA!E0xCUAx3ctL8wKS_tp-pNn95UaeXh_lRKy7b2Mcg4-S1_-Ss2N0b2nM5ld42UzHIa8rqXMpIaj50ioAx$`

King, V. M., Block, L. V., & Wood, C. K. (2016). Pressure/flow modeling and induced seismicity resulting from two decades of high-pressure deep-well brine injection, paradox valley, colorado. *Geophysics*, *81*(5), B119–B134.

Langenbruch, C., Weingarten, M., & Zoback, M. D. (2018). Physics-based forecasting of man-made earthquake hazards in oklahoma and kansas. *Nature communications*, *9*(1), 1–10.

Levandowski, W., Weingarten, M., & Walsh III, R. (2018). Geomechanical sensitivities of injection-induced earthquakes. *Geophysical Research Letters*, *45*(17), 8958–8965.

Lin, J., & Stein, R. S. (2004). Stress triggering in thrust and subduction earthquakes and stress interaction between the southern san andreas and nearby thrust and strike-slip faults. *Journal of Geophysical Research: Solid Earth*, *109*(B2).

Lundberg, S. M., & Lee, S.-I. (2017). A unified approach to interpreting model predictions. *Advances in neural information processing systems*, *30*.

Nikkhoo, M., & Walter, T. R. (2015). Triangular dislocation: an analytical, artefact-free solution. *Geophysical Journal International*, *201*(2), 1119–1141.

Papazafeiropoulos, G., Muñiz-Calvente, M., & Martínez-Pañeda, E. (2017). Abaqus2matlab: A suitable tool for finite element post-processing. *Adv. Eng. Softw.*, *105*, 9–16.

Qin, Y., Chen, T., Ma, X., & Chen, X. (2022). Forecasting induced seismicity in oklahoma using machine learning methods. *Scientific Reports*, *12*(1), 9319.

Reasenberg, P. A., & Simpson, R. W. (1992). Response of regional seismicity to the static stress change produced by the loma prieta earthquake. *Science*, *255*(5052), 1687–1690.

Rice, J. R., & Cleary, M. P. (1976). Some basic stress diffusion solutions for fluid-saturated elastic porous media with compressible constituents. *Rev. Geophys.*, *14*(2), 227. Retrieved 2021-04-13, from `https://urldefense.com/v3/__http://doi.wiley.com/10.1029/RG014i002p00227__;!!Mih3wA!E0xCUAx3ctL8wKS_tp-pNn95UaeXh_lRKy7b2Mcg4-S1_-Ss2N0b2nM5ld42UzHIa8rqXMpIai1FHNoQ$` doi: 10.1029/RG014i002p00227

Roeloffs, E., & Denlinger, R. (2009). An axisymmetric coupled flow and deformation model for pore pressure caused by brine injection in paradox valley, colorado: Implications for the mechanisms of induced seismicity. *Preliminary Report to the Bureau of Reclamation*.

Rudnicki, J. W. (1986). Fluid mass sources and point forces in linear elastic diffusive solids. *Mechanics of Materials*, *5*(4), 383-393. Retrieved from `https://urldefense.com/v3/__https://www.sciencedirect.com/science/article/pii/0167663686900426__;!!Mih3wA!E0xCUAx3ctL8wKS_tp-pNn95UaeXh_lRKy7b2Mcg4-S1_-Ss2N0b2nM5ld42UzHIa8rqXMpIahGXh2Vz$` doi: https://urldefense.com/v3/__https://doi.org/10.1016/0167-6636(86)90042-6__;!!Mih3wA!E0xCUAx3ctL8wKS_tp-pNn95UaeXh_lRKy7b2Mcg4-S1_-Ss2N0b2nM5ld42UzHIa8rqXMpIarQvXa1P$

Schoenball, M., Davatzes, N. C., & Glen, J. M. (2015). Differentiating induced and natural seismicity using space-time-magnitude statistics applied to the coso geothermal field. *Geophysical Research Letters*, *42*(15), 6221–6228.

Segall, P., & Lu, S. (2015). Injection-induced seismicity: Poroelastic and earthquake nucleation effects. *Journal of Geophysical Research: Solid Earth*, *120*(7), 5082–5103.

Shapley, L. S., et al. (1953). A value for n-person games.

Sharma, S., Hainzl, S., Zöeller, G., & Holschneider, M. (2020). Is coulomb stress the best choice for aftershock forecasting? *Journal of Geophysical Research: Solid Earth*, *125*(9), e2020JB019553.

Shirzaei, M., Ellsworth, W. L., Tiampo, K. F., González, P. J., & Manga, M. (2016). Surface uplift and time-dependent seismic hazard due to fluid injection in eastern texas. *Science*, *353*(6306), 1416–1419.

Stein, R. S. (1999). The role of stress transfer in earthquake occurrence. *Nature*, *402*(6762), 605–609.

Stokes, S. M., Ge, S., Brown, M. R., Menezes, E. A., Sheehan, A. F., & Tiampo, K. F. (2023). Pore pressure diffusion and onset of induced seismicity. *Journal of Geophysical Research: Solid Earth*, *128*(3), e2022JB026012.

Thompson, B. (2021). *cutde.* Retrieved from `https://github.com/tbenthompson/cutde`

Toda, S., Stein, R. S., Richards-Dinger, K., & Bozkurt, S. B. (2005). Forecasting the evolution of seismicity in southern california: Animations built on earthquake stress transfer. *Journal of Geophysical Research: Solid Earth*, *110*(B5).

Townend, J., & Zoback, M. D. (2000). How faulting keeps the crust strong. *Geology*, *28*(5), 399–402.

Trugman, D. T., & Ben-Zion, Y. (2023). Coherent spatial variations in the productivity of earthquake sequences in california and nevada. *The Seismic Record*, *3*(4), 322–331.

Van Der Elst, N. J., & Brodsky, E. E. (2010). Connecting near-field and far-field earthquake triggering to dynamic strain. *Journal of Geophysical Research: Solid Earth*, *115*(B7).

Wang, H. (2000). *Theory of linear poroelasticity: With applications to geomechanics and hydrogeology.* Princeton, New Jersey: 287 pp., Princeton Univ. Press.

Weingarten, M., Ge, S., Godt, J. W., Bekins, B. A., & Rubinstein, J. L. (2015).

High-rate injection is associated with the increase in us mid-continent seismicity. *Science*, *348*(6241), 1336–1340.

Zaliapin, I., & Ben-Zion, Y. (2013). Earthquake clusters in southern california i: Identification and stability. *Journal of Geophysical Research: Solid Earth*, *118*(6), 2847–2864.

Zaliapin, I., & Ben-Zion, Y. (2016). Discriminating characteristics of tectonic and human-induced seismicity. *Bulletin of the Seismological Society of America*, *106*(3), 846–859.

Zaliapin, I., Gabrielov, A., Keilis-Borok, V., & Wong, H. (2008). Clustering analysis of seismicity and aftershock identification. *Physical review letters*, *101*(1), 018501.

8 Supplementary

8.1 Model Pre-processing

A variety of issues and subsequent solutions arose in the model preprocessing that is important to elaborate on. As mentioned, previous work already compiled resources into a comprehensive, fully coupled poroelastic model of the PVU (Denlinger & RH O'Connell, 2020). However, this model was not easily portable to Abaqus and lacked sufficient discretization to capture large pressure gradients near the well. The methodology used to transfigure the initial model are presented here. We compare the model to a well known analytical solution and observed wellhead pressures to confirm its robustness.

8.1.1 Material Parameters and Meshing

The first difficulty with the Denlinger and O'Connel (D&O) model (Denlinger & RH O'Connell, 2020) is that the poroelastic material parameters are all defined at the nodes of the mesh. In Abaqus, there are a few material parameters defined at the nodes (pore pressure, void ratio, and saturation), but the elements (hexahedrons defined spatially by 8 nodes) are assigned other material parameters (ie. Young's modulus and bulk modulus of solid grains). After simple conversions of the given material parameters in the D&O model to the values used in Abaqus, we thought the best way to solve the issue of defining the *node only* values to elements would be to average the 8 nodal coordinates that make up a hexahedron element to the value at that element.

However, the averaging proved ineffective for a variety of reasons. First, the D&O model near the region of the well head experiences strong changes in material values. The Leadville formation, the high permeable injection formation, is embedded in low permeable material. The nodal change between these materials was actually only 1 node thick in some instances so by taking the average of 8 nodes resulted in significantly reducing the order of magnitude of material permeability for areas near fluid injection. Second, the strong changes in material values coupled with the large spatial discretization of the D&O model near the wellhead resulted in unrealistic gradients and convergence issues.

Therefore, in order to solve the issues present with the conversion of the D&O model to Abaqus, we decided to make several adjustments to our model that we believe make it a stronger model overall. First, we decided to reduce the spatial discretization near the well head. The well head is actually composed of 3 separate perforated injection zones and creates strong pressure gradients that require smaller spatial sampling in order to capture the large and rapid changes there. This is difficult to do based on the previous mesh since preserving spatial features such as dipping beds and down scaling material features is not straight forward. Thankfully, the vertical discretization was already well defined by the D&O model so the only change to the discretization was the horizontal directions. We solved this problem by preserving the number of elements whilst changing the horizontal spacing to grow exponentially from the location of the well head. Then, the vertical spacing and material parameters of the D&O model are preserved in the smaller spacing by using a nearest point search measured in Euclidean distance. The spatial meshing changes between the D&O model and ours are shown in Figure 1.

The second adjustment we made was in the determination of material parameters throughout the model. As previously mentioned the D&O model allows for entirely unique material parameters at every node, which caused difficulties in convergence for Abaqus. Using the newly discretized mesh of nodes/elements, and their associated material parameters, we applied a k-medoids clustering algorithm to cluster the nodes/elements based on similar material metrics across the combined set of materials. K-medoids is similar to k-means clustering, but instead of choosing the average from the kth cluster it chooses an actual data point as the center of the cluster. We worked with several different material cluster values, but ultimately decided on 1000. At this number, the model preserves many of the naturally occurring geological features such as the layered beds and salt domes whilst also maintaining a high level of material contrast near the wellhead without generating drastic gradients.

8.1.2 FEM Results Compared to Analytical Solution/Observation

A well known analytical solution exists to describe the spatial and temporal evolution of pore pressure due to continuous fluid injection into a poroelastic full space (Rudnicki, 1986). In order to gauge the success of the model, we first compare this solution to the 3D model using homogeneous material parameters. Additionally, we reduce the 3 injection nodes to a single node to better reflect the analytical solution. The radial analytical solution of pore pressure is compared with the closest radial axis given by the nodes shown in Figure 22. The solution for pore pressure matches well to the analytical solution after 10 days of constant injection using a typical bulk value of the crust as shown in Figure 23.

One thing to note is that the solution of pore pressure increases rapidly closer to the point of injection. The strong pressure gradients at this location require smaller elements then the horizontal discretization in the D&O model (200 m).

With the model now confirmed in the simplest case it was time to test a variety of k-medoid models, as previously described, and compare them to the observed wellhead pressures to confirm that the model was capable of capturing the observations. It is important to note that any complex model will result in overfitting of the wellhead data, and thus poor predictive ability for future data.

There has been a plethora of previous work from observational drilling to pressure-flow modeling designed to capture the reservoir permeability structure (V. King & Block, 2019). These different observations and modeling have provided a sizeable range of permeability values. For example, the permeability of intact limestone and dolomite varies from 0.01 to 0.1 mD (Bear, 1988). Fracturing is expected to increase permeability outside of this laboratory setting. Drill stem tests gave an original permeability of 7.97 mD, yet at the same time additional analysis indicated permeability between 1.3 and 1.5 mD. Samples from a well 4.6 km to the northeast yielded permeability ranges of 0.03 to 1.3 mD (Harr, 1988). An earlier model by Denlinger and Roeloffs (Roeloffs & Denlinger, 2009) arrived at a permeability in the injection zone of 28 mD, with significantly lower values for the other formations. Additional pressure-flow models also arrive at ranges of 9.06 to 29.2 mD for certain injection phases (V. King & Block, 2019). The current *best* model (the D&O model) throughout the entire model domain, only has a maximum permeability of 1.97 mD. The final 1000 k-medoids model, modeled at constant injection rate (typical daily average from PVU injection data), is compared with several hypothetical analytical solutions for constant injection rate for a range of bulk permeabilities in Figure 24.

The final 3D heterogeneous model compares well with a range of typical observational values and observed wellhead pressures. In the near-field, the permeability matches the higher permeability analytical solutions as expected since there is likely fractured media in this location (V. King & Block, 2019). In the far-field, where the permeability structure is expected to decrease, the model approaches the lower permeability analytical solution. For the future, it will likely be important to test a variety of physics based models to understand the sensitivity introduced in the machine learning. However, we are confident in the evidence presented that our current model, adopted from the D&O model, is robust enough to continue with the primary goal of this work.

671 ## 8.2 Supplementary Figures

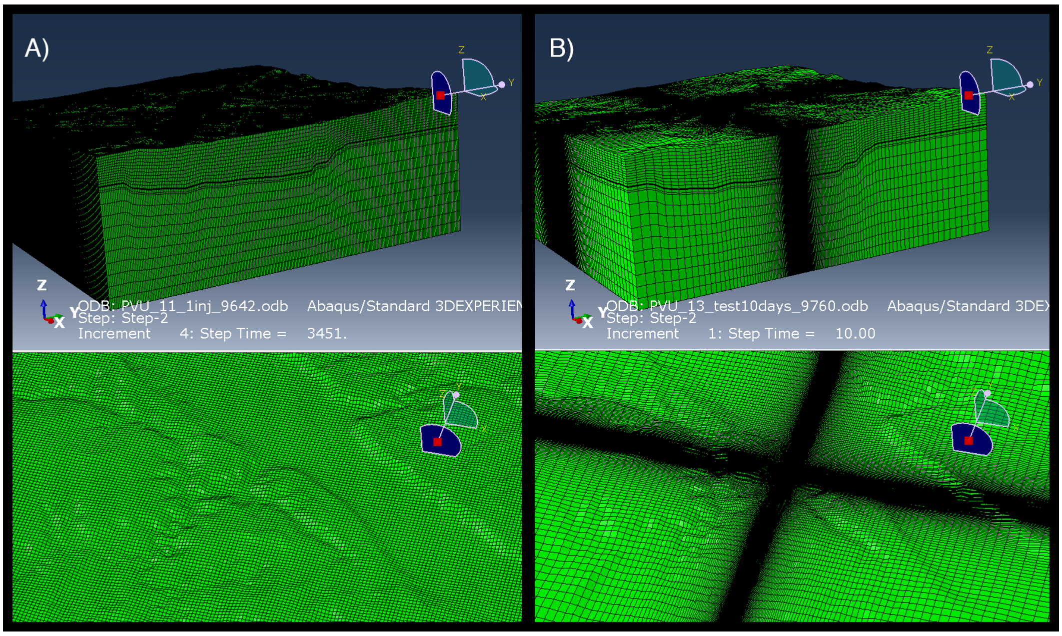

Figure 1. Previous model mesh from D&O model (Panel A) with surface view of well location compared to (Panel B) our smaller discretized model with similar surface view.

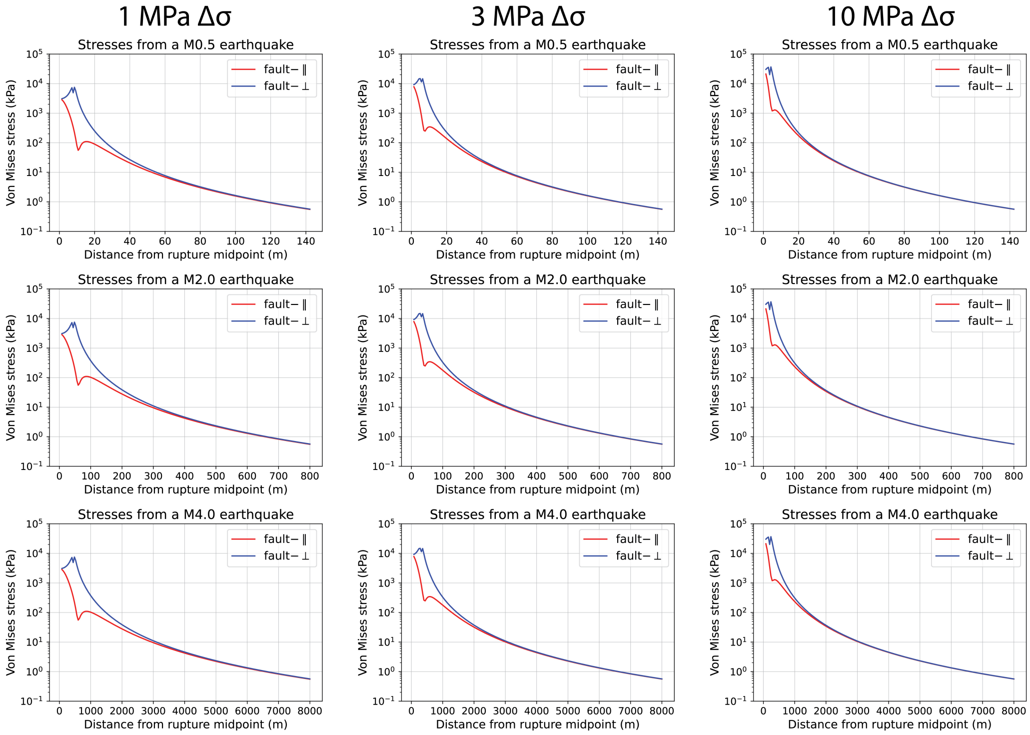

Figure 2. The von Mises stress in kPa for the three varying earthquake magnitudes (0.5, 2.0, and 4.0) for three varying stress drops (1, 3, and 10 MPa). We use cutde (Thompson, 2021) to resolve stress transfer produced from fullspace triangle dislocation elements assuming a uniform stress drop, a shear modulus of 30 GPa, and a Poisson ratio of 0.25. We show that the von Mises stress is self similar for opposite receiver planes at certain distances, dependent on the magnitude, produced by the dislocation. We use thetriggering threshold of 10 kPa (Reasenberg & Simpson, 1992; Stein, 1999) which increases depending on the magnitude size. This distance is our perturbable radius used for the earthquake feature.

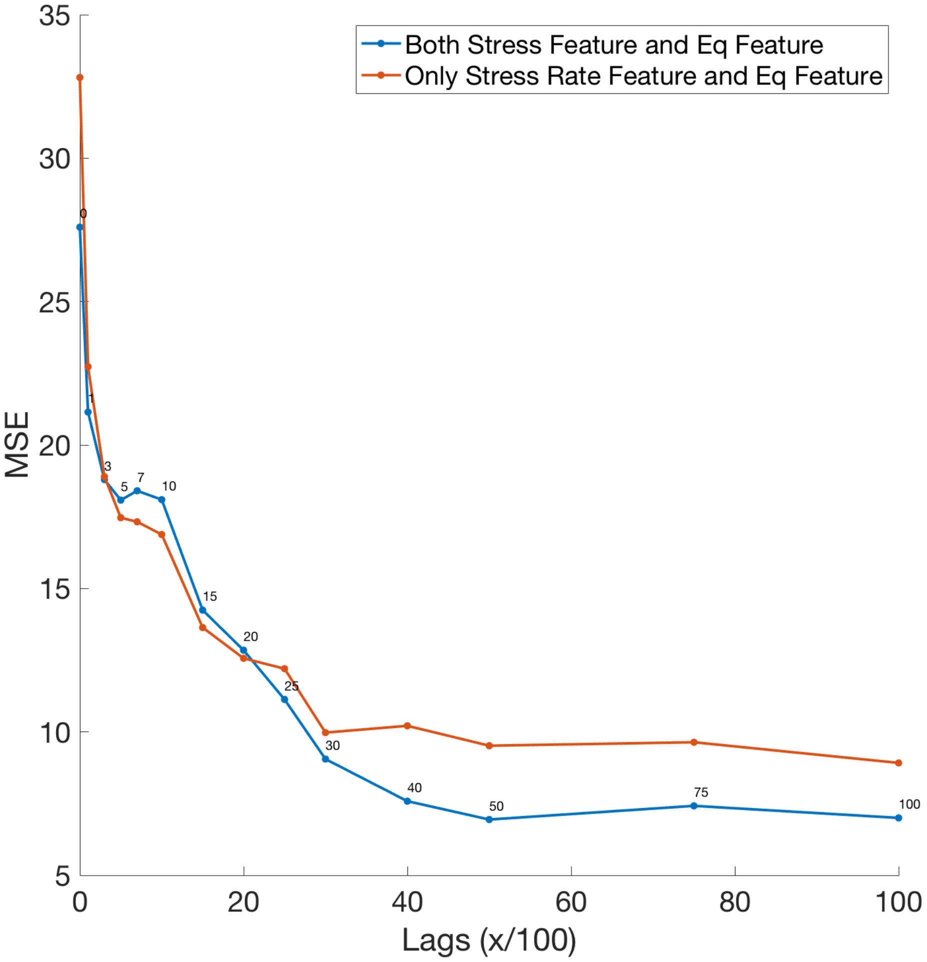

Figure 3. A sensitivity test to increasing and the overall MSE fit to the seismicity rate. We find that there is a local minimum near 5 lags. The fit does not improve after approximately 50 lags.

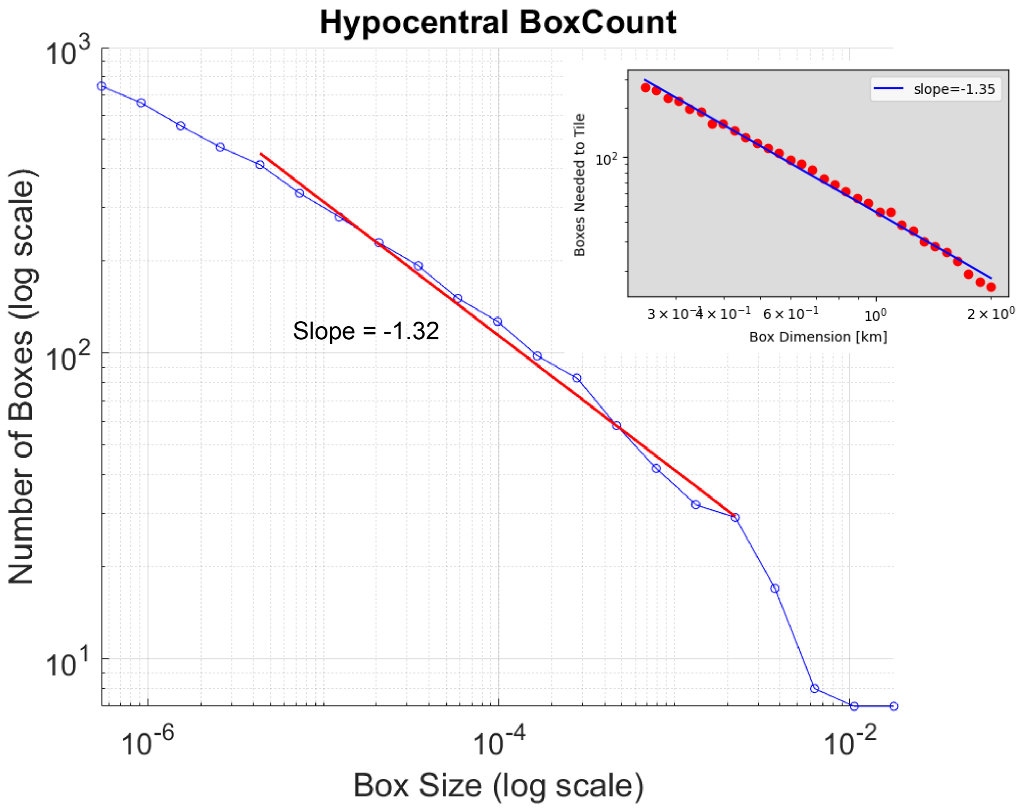

Figure 4. Hypocentral and epicentral (inlet) box-counting procedures with good agreement on the fractal dimension d_f=1.32 of the earthquakes at Paradox Valley.

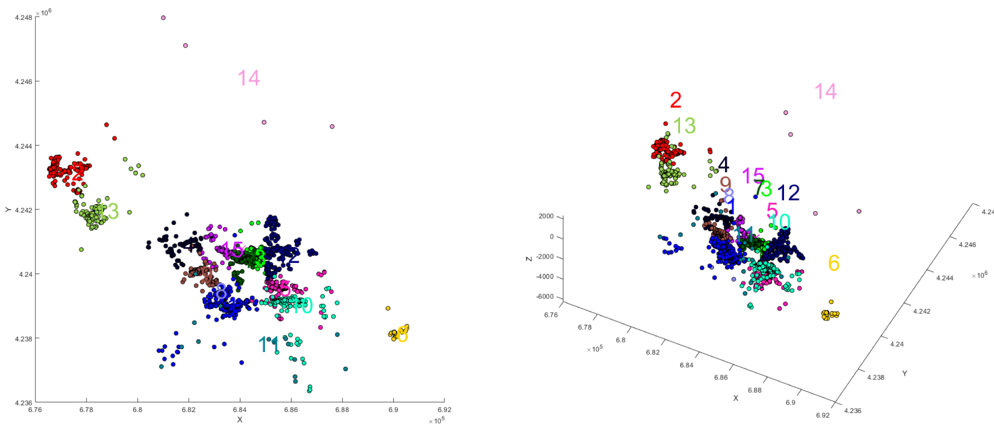

Figure 5. Different k-means cluster locations (1-15) of seismicity for the PVU. We extract the pore pressure at the center of each seismicity cluster from the numerical model in the subsequent figures. We include results for the near well cluster (7), two further regions with more diffuse responses (4) and (10) as well as farther distance (2) and (6).

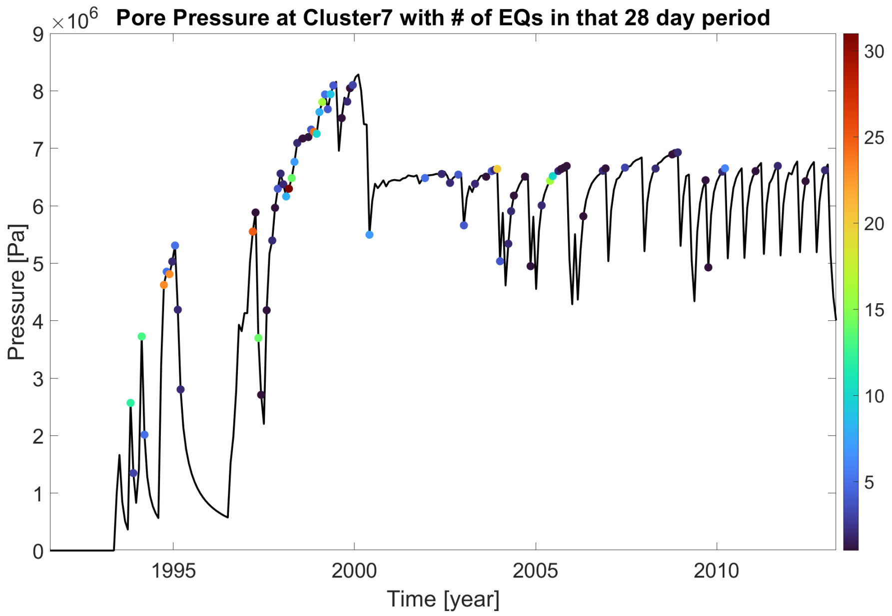

Figure 6. Cluster 7 near the well and pore pressure profile at the center of cluster. The pore pressure mimics the injection well rates due its close vicinity to the well.

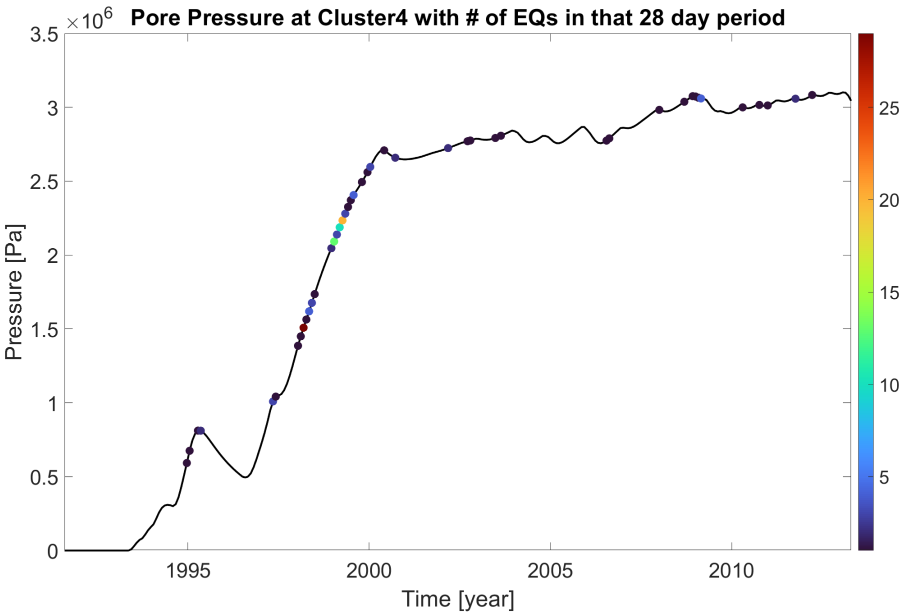

Figure 7. Cluster 4.

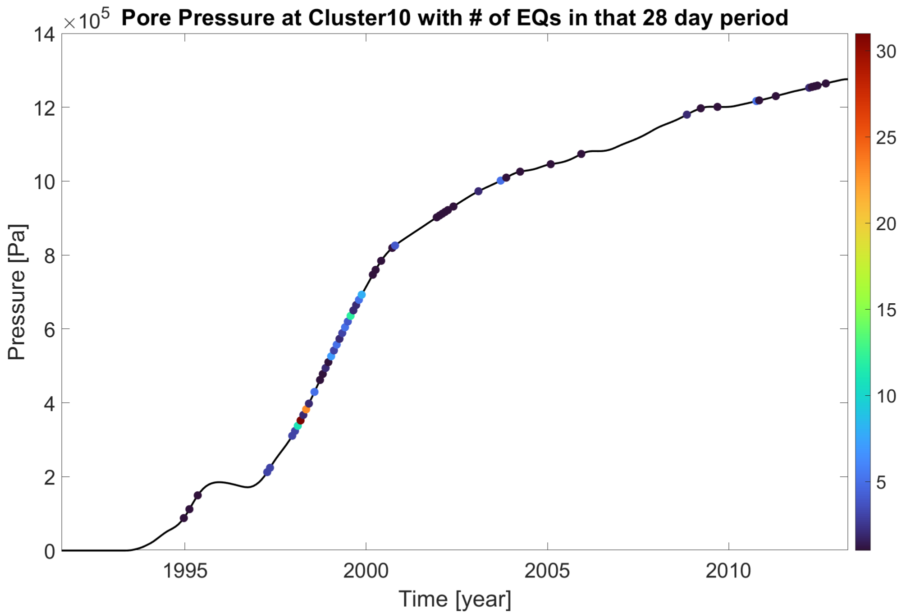

Figure 8. Cluster 10.

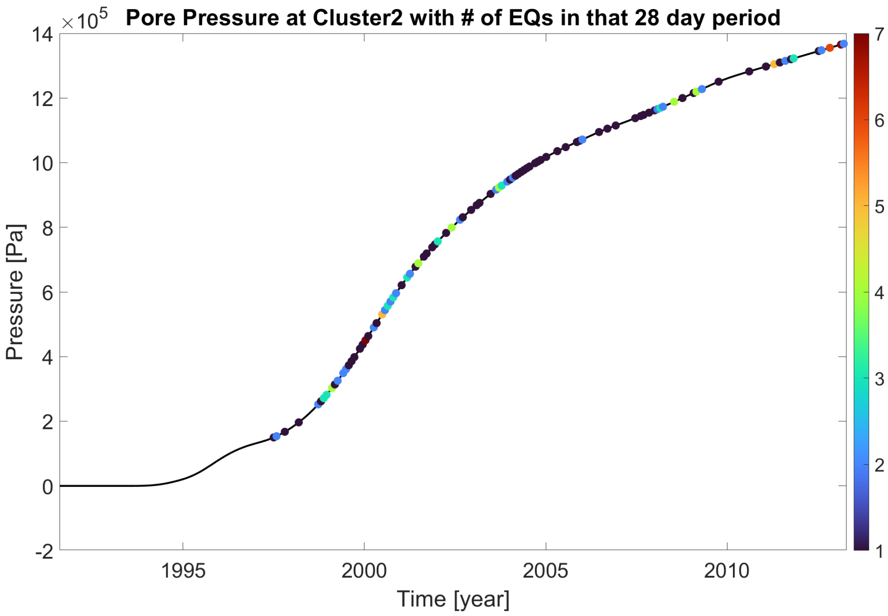

Figure 9. Cluster 2.

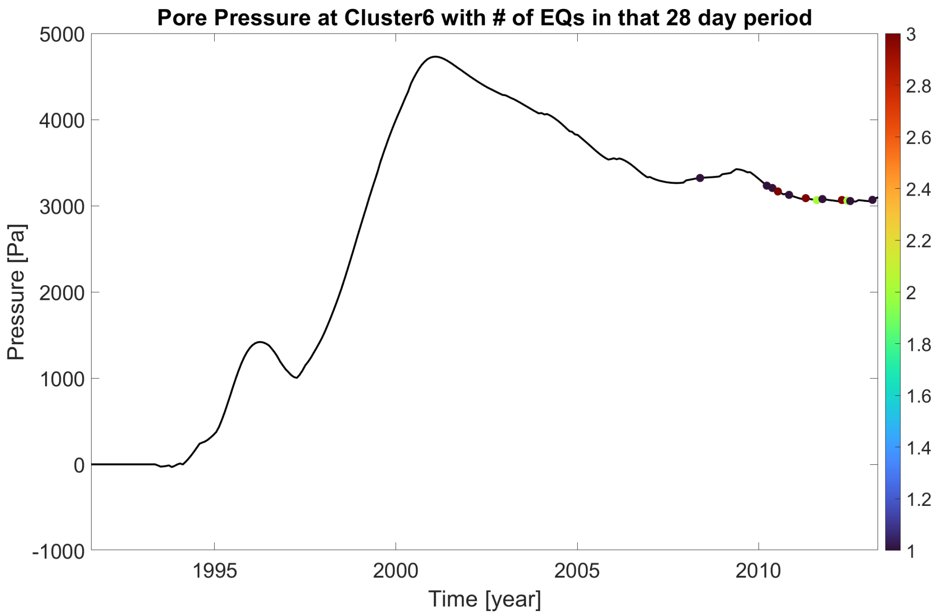

Figure 10. Cluster 6.

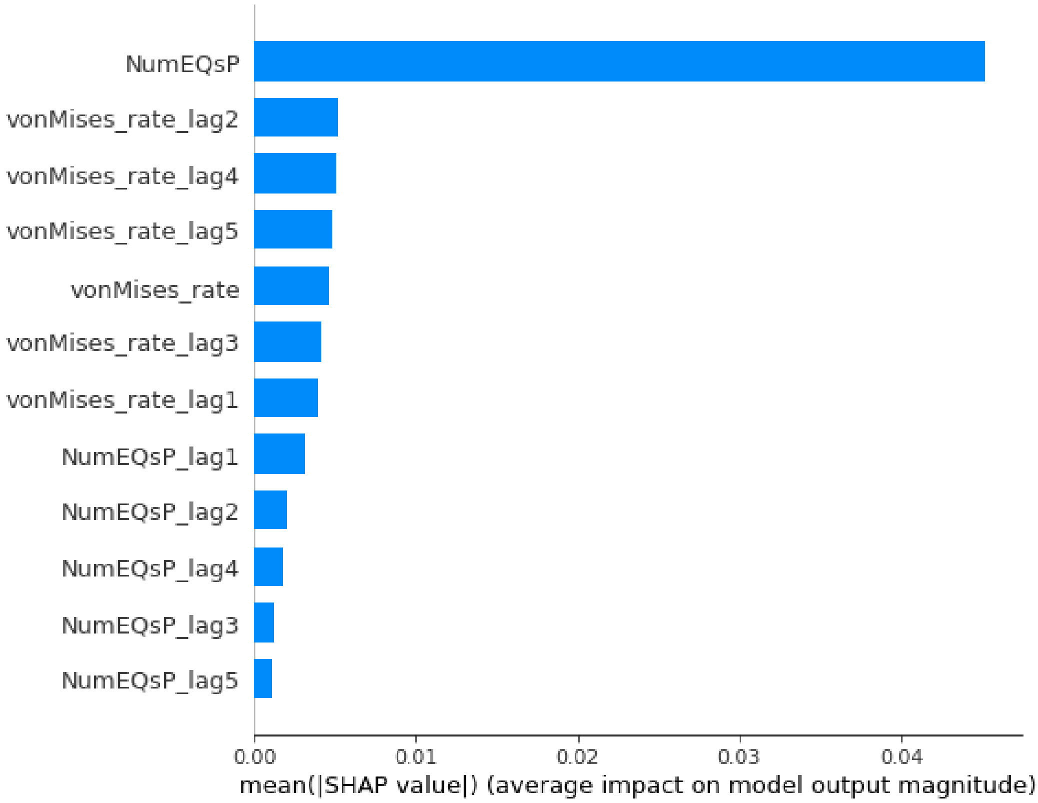

Figure 11. Similar to SM Figure 15 but for the model that includes both the von Mises stress and the von Mises stress rate. This represents 2927 total events. The most important feature is the number of perturbable earthquakes (NumEQsP) that occurred during that same time step as the earthquake in question. The next 65 variables are a mix of the von Mises and von Mises rate.

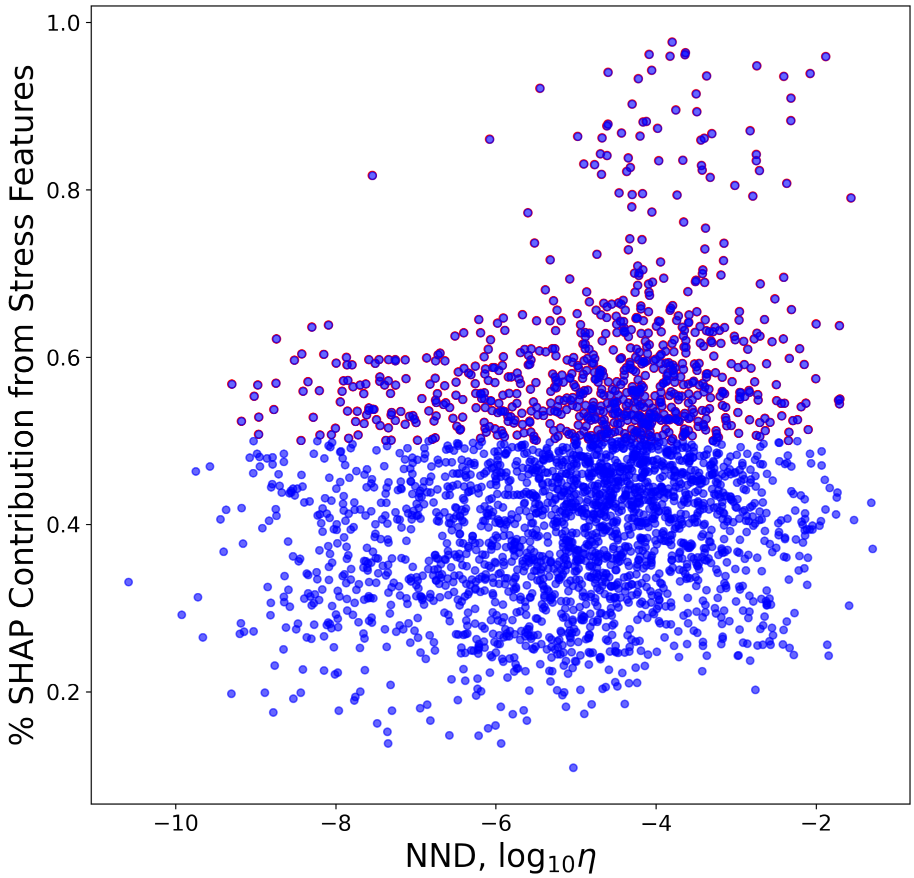

Figure 12. Similar to Figure 3c but for the model that includes both the von Mises stress and the von Mises stress rate. There is more earthquakes associated with the clustered mode, but still a large amount of background mode earthquakes.

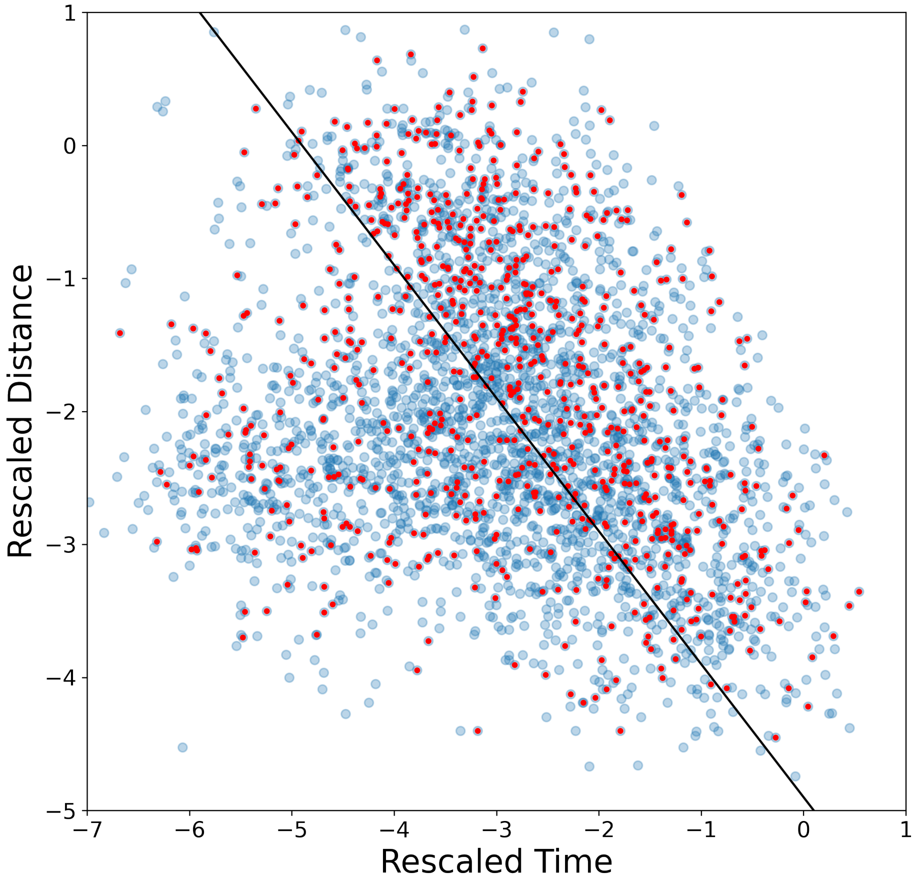

Figure 13. Similar to Figure 3b but for the model that includes both the von Mises stress and the von Mises stress rate. There is more earthquakes associated with the clustered mode, but still a large amount of background mode earthquakes.

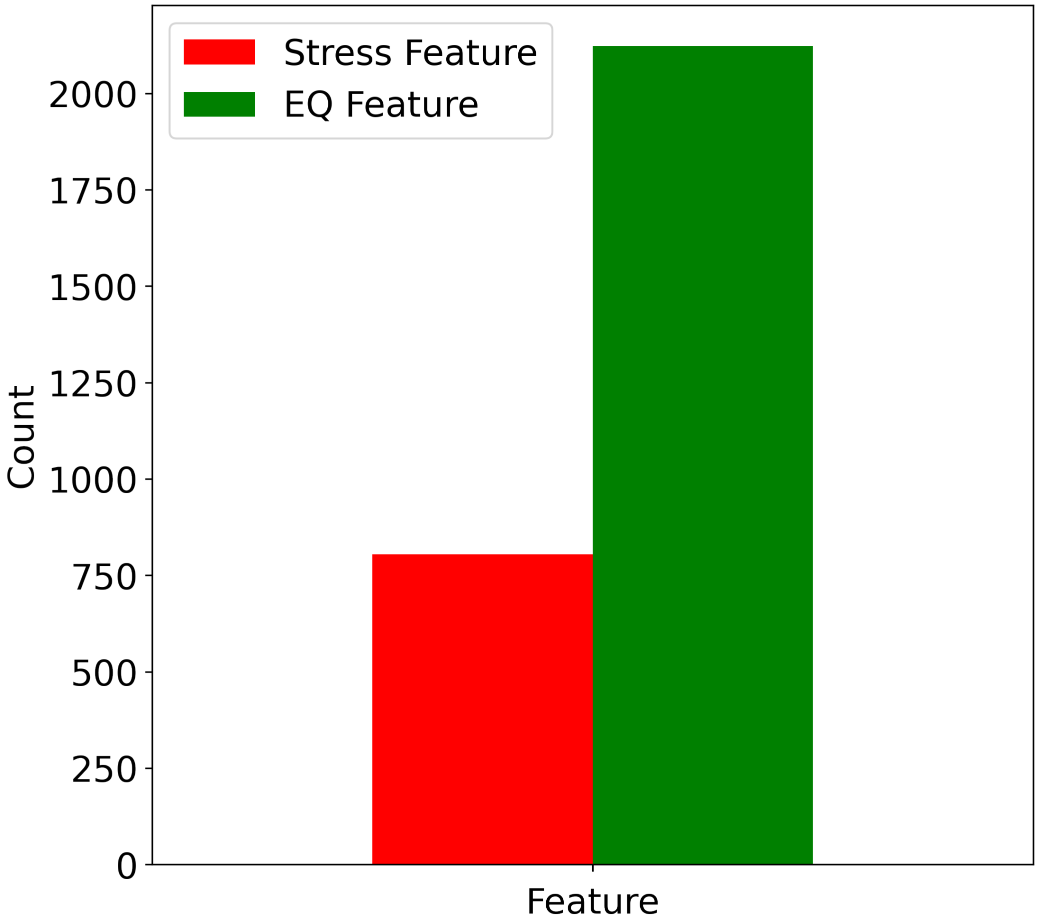

Figure 14. Similar to Figure 4e but for the model that includes both the von Mises stress and the von Mises stress rate. Ratio of the earthquake stress contribution totals for both the stress features and the earthquake features. For our model of including +5lags the stress feature to earthquake feature ratio approximately 1:3 which is must higher than the (1:5) ratio seen in the model that only has one stress feature.

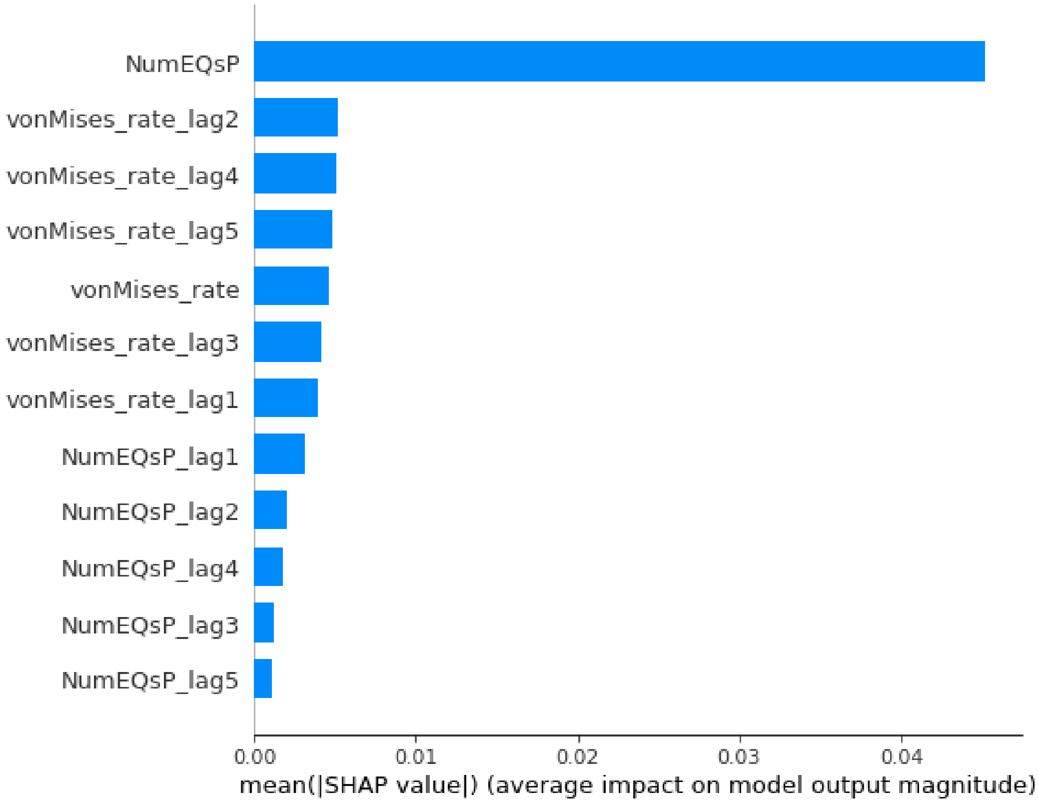

Figure 15. Mean absolute SHAP value for times in the model that an earthquake actually occured. This represents 2927 total events. The most important feature is the number of perturbable earthquakes (NumEQsP) that occurred during that same time step as the earthquake in question. The next 6 variables are all the stress rate from the stress change from the injection.

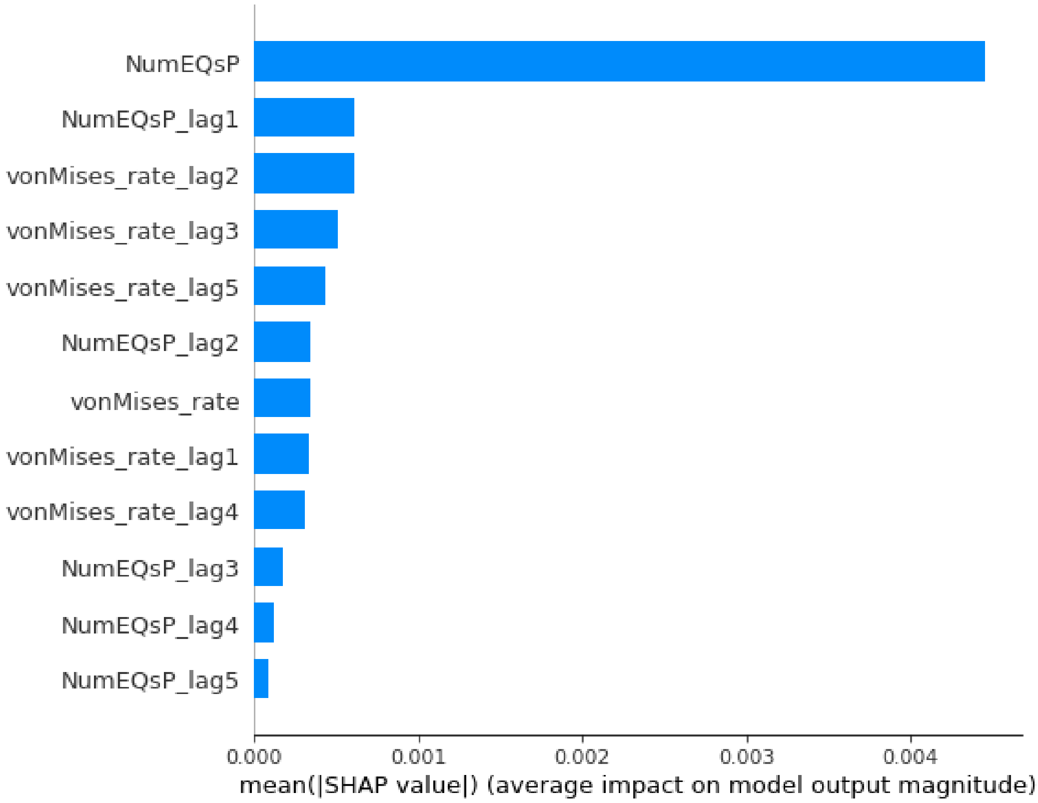

Figure 16. Simlar to SM Figure 15 except for all time steps in the model which includes the time steps when an earthquake is not occurring ($2927 * 284 = 831,268$ total samples).

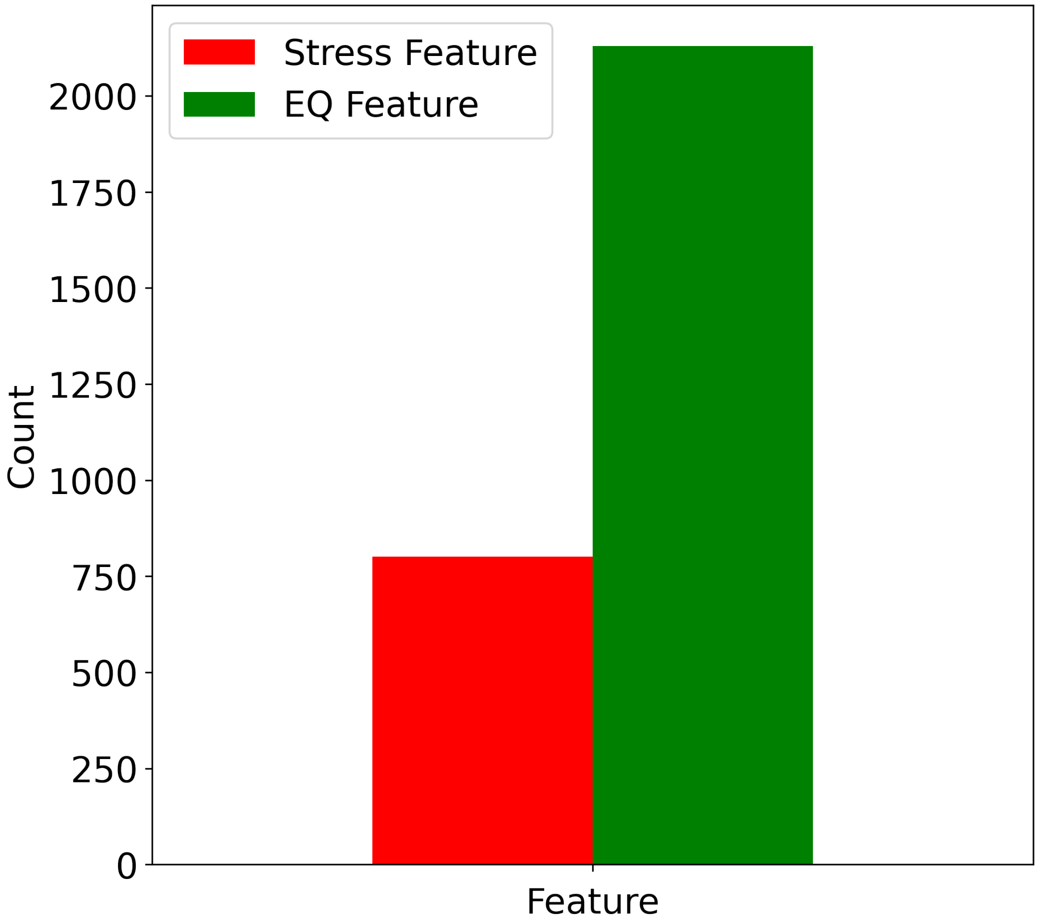

Figure 17. Similar to SM Figure 14 but for the model that includes both the von Mises stress and the von Mises stress rate and only +3 lags. The ratio is (0.3762) compared with the ratio at +5 lags (0.3789). Implying, that the ratio is not sensitive to increasing lags after +3.

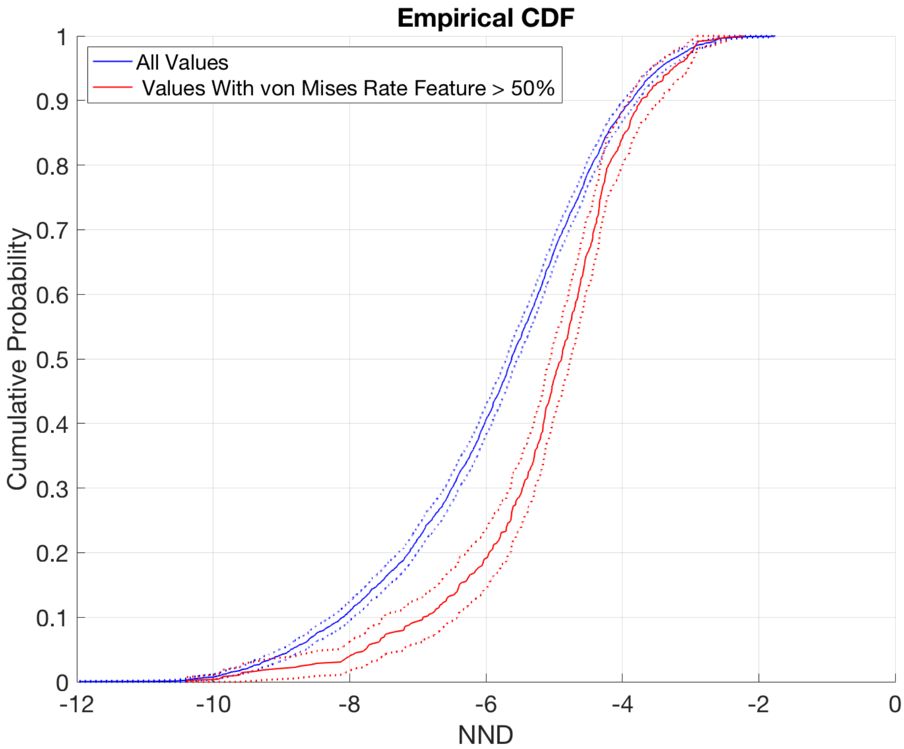

Figure 18. Empirical cumulative density functions of the two sample Kolmogorov–Smirnov test. We show that the distribution for the earthquakes with stress contribution >50% are not drawn from the same distribution as the total earthquakes with 99% confidence. Dashed line represents lower and upper confidence bounds for each distribution.

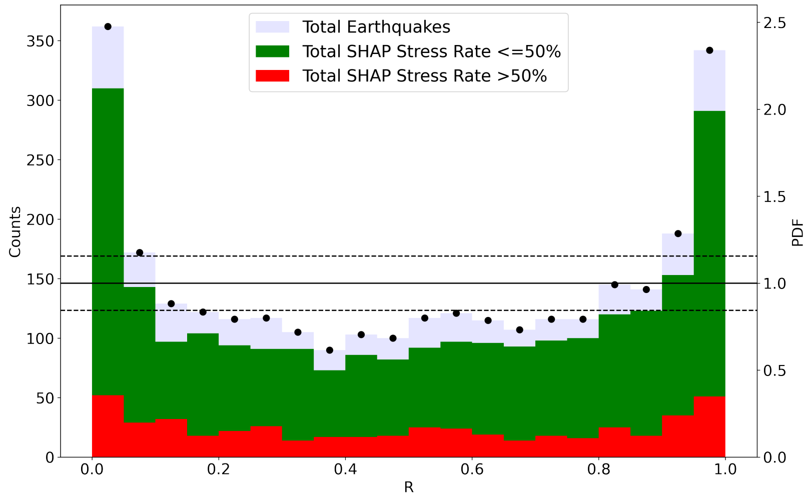

Figure 19. Results of interevent time measure R-test (Van Der Elst & Brodsky, 2010; Davidsen et al., 2017). The histograms represent count of earthquakes for the total earthquakes (blue) and the portion of this set for the the earthquake-driven earthquakes (green) and injection-driven earthquakes (red). The overall events reject the null-hypothesis due to the PDF of the interevent time ratio R exisiting outside the the dotted lines corresponding to the 95% confidence intervals of a Poisson process. Notice that the bimodal tails near $R = 0$ and $R = 1$ are indicative of clustering. The majority of the these tails are composed of earthquake-driven events. The injection-driven earthquakes are considerably flatter and represent a lower portion of the clustered seismicty in the overall catalog.

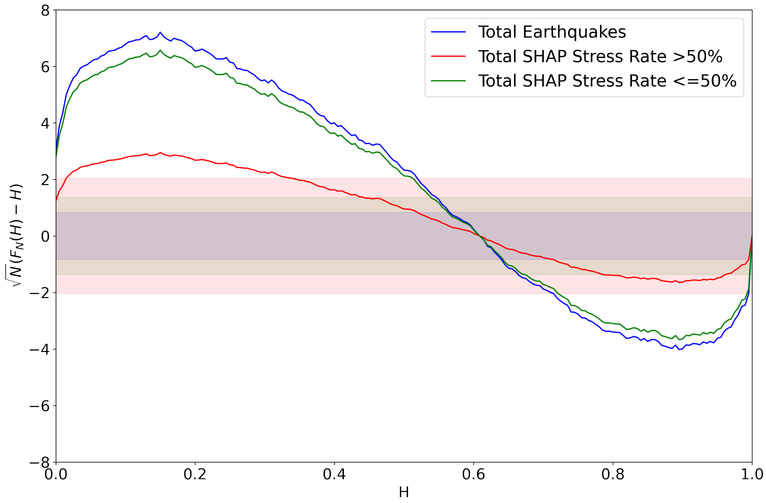

Figure 20. Results of the two sample Kolmogorov-Smirnov test for the distribution of the H statistics obtained by the Bi-test (Bi et al., 1989; Baró et al., 2014; Davidsen et al., 2021). The overall sesimicity (blue) and the portion of cumulative components of the earthquake-driven earthquakes (green) and injection-driven earthquakes (red). The three color bars represent the 50%, 95%, and 99.95% confidence bounds for the null hypothesis of a Poisson process ($F_n(H) = H$). Notice that the portion H attributed to injection-driven earthquakes are significantly flatter compared to the clustered earthquake-driven earthquakes which implies a smaller component of the clustered seismicity albeit we can not reject that it is clustered.

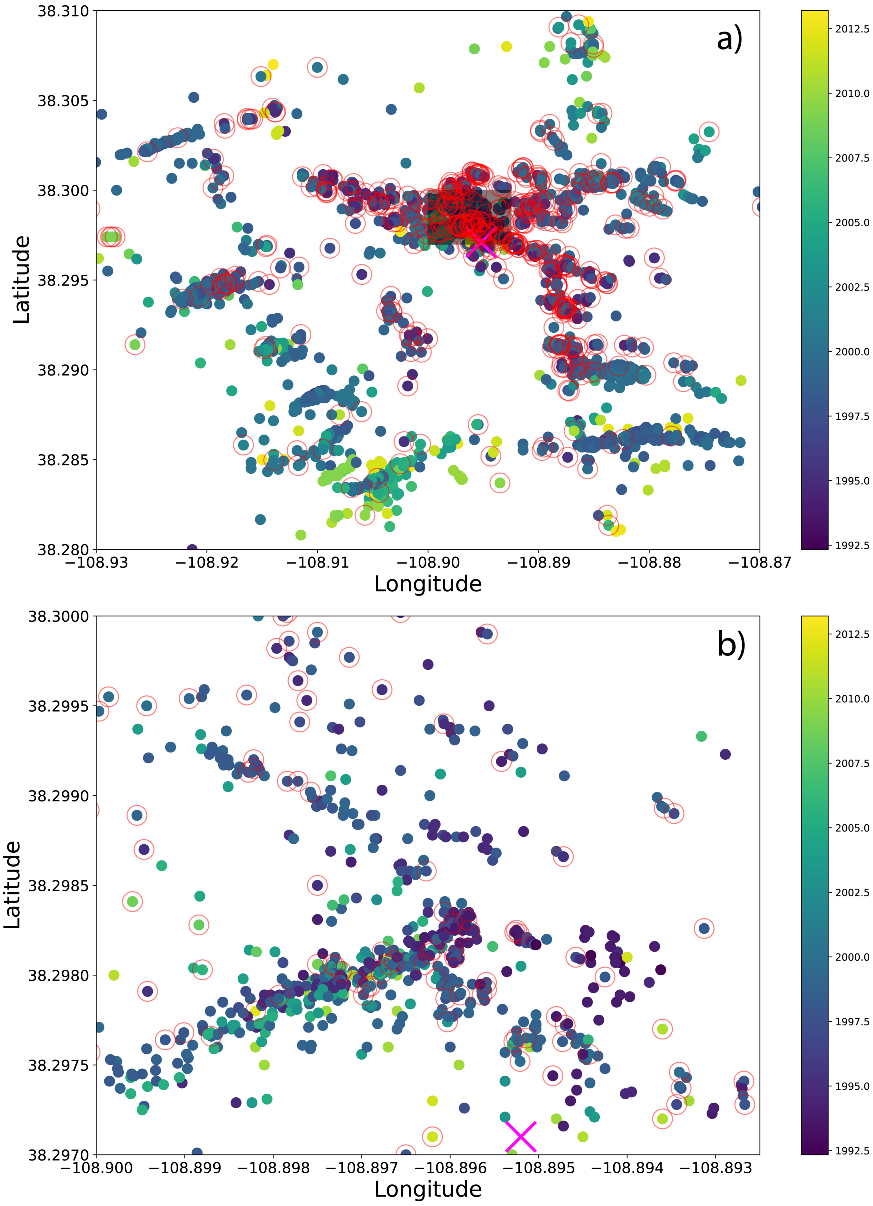

Figure 21. a) Map view of most earthquakes used in our study and denoted in color by the time they occurred. The red circled events represent those circled in red in Figure 3 (i.e. earthquakes that had >50% stress feature contribution). b) same as above panel, but zoomed in near well. The earthquakes strongly stress driven near the injection well, but also appear at different clusters throughout the domain. Often those away from the well have early times compared to the other earthquakes in their cluster suggesting they may be starting the seismicity in those areas. There are some examples of earthquakes that are close but nearly stress driven as opposed to earthquake driven as well.

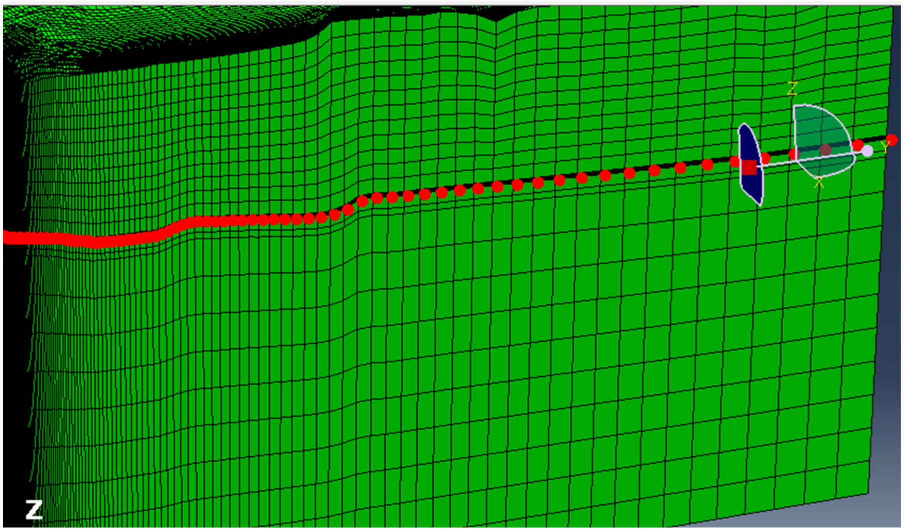

Figure 22. Nodes used in comparison with analytical solution. Well is located on the left and extends to the far field on the right.

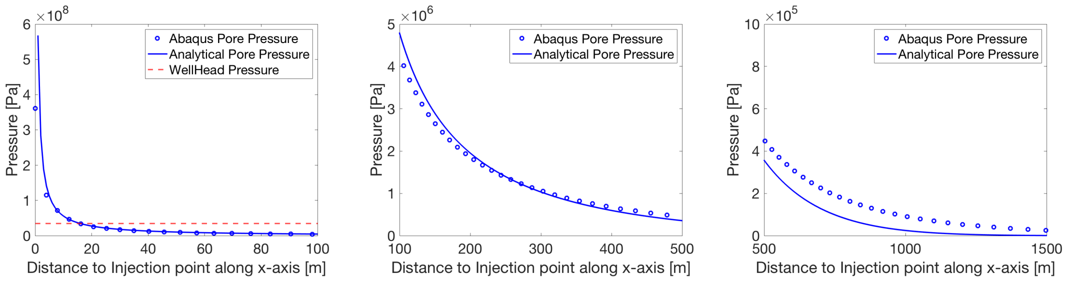

Figure 23. Analytical solution compared to the homogeneous 3D model. Dashed red line represents the average well head pressure of the observed PVU.

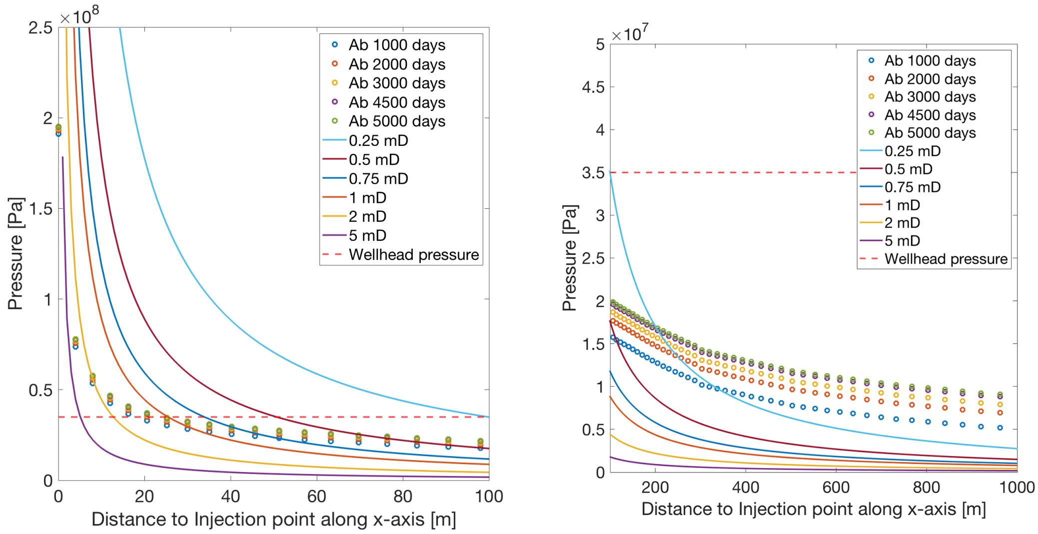

Figure 24. Final 1000 k-medoids model compared to several analytical solutions for a variety of constant rate injection times.